UNIVERSITÀ DEGLI STUDI DI GENOVA

ISTITUTO ITALIANO DI TECNOLOGIA

UNIVERSITY OF GENOVA

PHD PROGRAM IN BIOENGINEERING AND ROBOTICS

Single Layer Graphene Biointerface: Studying Neuronal Network Development and Monitoring Cell Behavior over Time

by

Amira El Merhie

Thesis submitted for the degree of *Doctor of Philosophy* (31^{o} cycle)

February 2019

Dr. Silvia Dante — Tutor
Prof. Alberto Diaspro — Supervisor

Thesis Jury:
Prof. Fabrizio Barberis, *Università degli Studi di Genova*
Prof. Michele Celebrano, *Politecnico di Milano*
Prof. Donato Vincenzi, *Università degli Studi di Ferrara*

Dibris

Department of Informatics, Bioengineering, Robotics and Systems Engineering

This thesis is dedicated to my family.

Declaration

I hereby declare that except where specific reference is made to the work of others, the contents of this dissertation are original and have not been submitted in whole or in part for consideration for any other degree or qualification in this, or any other university. This dissertation is my own work and contains nothing which is the outcome of work done in collaboration with others, except as specified in the text and Acknowledgements. This dissertation contains fewer than 65,000 words including appendices, bibliography, footnotes, tables and equations and has fewer than 150 figures.

Amira El Merhie

February 2019

Acknowledgements

This dissertation would not have been accomplished without the support of many people. Herein, I would like to thank those who have contributed in various ways to make this dissertation a reality.

First and foremost, I would like to express my sincere gratitude to my supervisor Dr. Silvia Dante for her constant support, enthusiasm, guidance and immense knowledge. I am thankful for her understanding and for always being there for me to advice and to support in the research-related issues but not only. I am grateful for the time that she spent with me; suggesting, discussing and correcting. If I had to choose a supervisor, I couldn't have imagined any better than her.

I would also like to express my gratefulness to Prof. Alberto Diaspro, the head of Nanoscopy & NIC@IIT (Istituto Italiano di Tecnologia) research group that I am a part of, for giving me the chance to become a member of his group and for giving me the freedom to choose my own research project. I would have not carried out the interesting and multidisciplinary PhD project of mine if it were not for him in the first place.

I am very thankful to my informal supervisors Dr. Marco Salerno and Dr. Claudio Canale for all the advice that they gave me and for a friendly lab atmosphere that I encountered since I joined IIT. I want to thank as well my dear friends and colleagues Barbara and Michela for the nice time that we spent together throughout those three years, for the moments of fun and seriousness and for always supporting one another. Special thanks to my friends from other departments Ahmed, Sedat, Fatima, Leyla, Reinier, Ilaria, Quinten and Emma for the nice and exciting moments in the institute and outside of it. I am glad for meeting you guys, and I hope that we always keep in touch. I would also like to thank one of my best friends Nicole for supporting me from a distance.

I would like to thank the staff of the human resources for helping to deal with the associated bureaucracy. I would also like to express my appreciation to my group members for the nice and friendly atmosphere in the group. Besides, I would like to warmly thank our administrative assistant Mrs. Manuela Salvatori for always being ready to answer all administrative related questions and for assisting in dealing with them. Furthermore, I would like to extend my sincere gratefulness to the lab technicians Marco Scotto, Lara Marini, Riccardo Carzino and especially Simone Nitti, Giammarino Pugliese, and Gabriele La Rosa for their help in different experimental techniques.

Finally, my deepest thanks go to my loving family, who were always there for me with their encouragement, motivation and belief in me – to my parents Liudmila and Fayez, my dearest sister Natalia, my beloved grandparents and all my dear relatives. I dedicate this thesis to you.

Table of Contents

LIST OF TABLES ..... **I**

TABLE OF FIGURES ..... **I**

LIST OF PUBLICATIONS ..... **IV**

LIST OF CONFERENCES ..... **IV**

AWARDS ..... **V**

LIST OF ABBREVIATIONS ..... **VI**

INTRODUCTION **1**

CHAPTER 1: GRAPHENE AS CELL INTERFACE **3**

1.1 Graphene **4**

1.2 Graphene as a Biocompatible Material **5**
1.2.1 Graphene as cell interface 6
1.2.2 Single Layer Graphene (SLG) 7

CHAPTER 2: SURFACE CHARACTERIZATION **10**

2.1 SLG Transfer **12**

2.2 Excimer Laser Micromachining of SLG **13**

2.3 Functionalization of SLG Substrates **15**

2.4 Physicochemical Characterization of SLG Substrates **17**
2.4.1 Raman Characterization 17
2.4.2 G-band and 2D-band Shift 18
2.4.3 Raman Mapping 19
2.4.4 Pump-probe Microscopy 20
2.4.5 Scanning Kelvin Probe Microscopy (SKPM) 23
2.4.6 Water Contact Angle (WCA) 26
2.4.7 ATR-FTIR 29
2.4.8 Quantitative imaging 31

2.5 Conclusions **34**

CHAPTER 3: SLG BIO-INTERFACE 35

3.1 Cell Culture 37

3.2 Assessment of Cell Viability 38

3.3 Proliferation Curves 39

3.4 N2a Differentiation 41

3.5 Immunofluorescence Staining and Image Analysis 41

3.6 Statistical Analysis 42

3.7. Confocal Imaging and Image Analysis 42

3.8 Visualizing samples using pump-probe microscopy 46

3.9 Conclusions 48

Supporting information 49

CHAPTER 4: SLG FUNCTIONALIZED MEAS FOR ENHANCED DETECTION OF NEURONAL NETWORK DEVELOPMENT 50

4.1 Micro-Electrode Arrays (MEAs) 51

4.2 SLG and MEAs 52

4.2.1 LG-SLG 53
4.2.2 LG-SLG transferring and characterization 53
4.2.3 Primary neuronal cultures 55
4.2.4 Immunolabeling, confocal microscopy and image analysis 56
4.2.5 MEA recordings 59
4.2.6 Experimental database 60
4.2.7 Spike detection and firing analysis 60
4.2.8 Burst detection 61
4.2.9 Cross correlation analysis 61
4.2.10 Statistics 62
4.2.11 Analysis of neuronal network activity 62
4.2.12 Discussion 67

4.3 Conclusions 70

4.4 Perspective 71

APPENDICES 73

APPENDIX A 74

APPENDIX B 102

REFERENCES 89

List of Tables

Table 1 Change of SLG Raman G and 2D peaks position and width before and after polymer coating, according to the best fitting curves in Fig. 2.7. 19

Table of Figures

Figure 1.1 Graphene and graphene-related materials (25) 5
Figure 1.2 SLG on glass substrates (44)..... 7
Figure 1.3 Schematic of a common setup for chemical vapor deposition of graphene (47)..... 8
Figure 2.1 Schematic representation of SLG transfer, micropatterning, functionalization and characterization. 11
Figure 2.2 Schematic representation of the transfer of SLG from Cu foil onto glass coverslip. 13
Figure 2.3 Laser micromachining - Schematic representation of micro-patterning by laser ablation on SLG. 15
Figure 2.4 Chemical structure of polylysine (59) 15
Figure 2.5 Surface interaction between positively charged polylysine and negatively-charged ions of the cell membrane. 16
Figure 2.6 Raman analysis of SLG - Raman spectrum indicating the D, G and 2D peaks of SLG transferred onto a glass coverslip. 18
Figure 2.7 G-band and 2D-band Raman peak of bare SLG (black, dotted) and of PDL coated SLG (red, dotted). A progressive shift towards higher wavenumber is observable. 19
Figure 2.8 Raman component color map of the region irradiated at 0.5 J/cm^2. The maps have been generated by taking the fitted Raman spectra of unmodified SLG as component. 20
Figure 2.9 Pump-probe microscopy image of SLG/ablated substrate 22
Figure 2.10 A schematic representation of Kelvin probe force microscopy (98)..... 24
Figure 2.11 AFM topography of the patterned substrate before (a) and after PDL coating (d). Center: SKPM maps of the same region, showing a higher potential in correspondence of the ablated squares (b, e). Right: Scan line profiles of topography and surface potential. 25
Figure 2.12 SP contrast at the surface of a SLG sample transferred on SiO2: the SP on the ablated squares is lower than on SLG background. 26
Figure 2.13 Schematic representation of contact angles formed by sessile liquid drops on a smooth homogeneous surface. 27
Figure 2.14 WCA on different surfaces (mean ± standard deviation). Pairs joined by lines show statistically significant difference (**: $p<0.01$, ***: $p<0.001$)..... 28
Figure 2.15 A schematic representation of the principle of ATR-FTIR (100)..... 29
Figure 2.16 A, B, infrared spectra of PDL and SLG/PDL samples in the 3600-3000 and 1900-1400cm^{-1} regions, respectively. Arrows in A are used as guides to highlight the observed changes. 31

Figure 2.17 Force-distance curve……..……32
Figure 2.18 F_{adh} and W_{adh} on SLG and ablated substrates, coated with PDL and not. 33
Figure 3.1 Confocal images of N2a cells incubated on bare SLG (A) and PDL/SLG (B) substrates for 48 h treated with live/dead assay kit. 38
Figure 3.2 Proliferation curves of N2a cells on bare and coated SLG substrates..... 40
Figure 3.3 Proliferation curves of CHO cells on bare and coated SLG substrates. 40
Figure 3.4 One representative sequence of large-scope confocal images of N2a cells after 48 h cultured on control bare glass (A), bare SLG (B) and PDL/SLG (C) (scale bar is 50 μm). 43
Figure 3.5 One representative sequence of large-scope confocal images of N2a cells after 48 h cultured on control bare glass (A), bare SLG (B) and PDL/SLG (C) with retinoic acid (scale bar is 50 μm). 44
Figure 3.6 Functional parameters of adhering cells: (A) neuritogenesis, (B) mean normalized length of the existing neuritic-like processes. Pairs joined by lines show statistically significant difference (*: $p<0.05$; **: $p<0.01$)..... 44
Figure 3.7 Confocal images of N2a cells after 48 h of incubation with RA on ablated SLG (A) and SLG substrates (B). Scale bar: 50 μm. 45
Figure 3.8 Optical image of CHO cells cultured on ablated/SLG substrate (48h after cell seeding). ... 46
Figure 3.9 Pump-probe microscopy images of the N2a cells cultured on the SLG substrate. 47
Figure 4.1 SEM micrograph of a partial growth of graphene on Cu foil. The average diagonal size of the single crystals is about 200 μm. 54
Figure 4.2 A schematic of the wet etching transfer of SLG onto a commercial MEAs device B: Optical image of the functionalized MEA; the coated electrode source of the spectrum is reported in the zoomed image on the left side, where the laser spot for Raman analysis is visible in the middle of the electrode. C: Raman characterization of the transferred SLG showing the two characteristic G and 2D band. 55
Figure 4.3 Morphological changes in hippocampal networks cultured on graphene-transferred substrate during development. A. Immunofluorescence micrographs of MAP2 of a representative culture on normal coverslips (top) and on LG-SLG coated coverslips (bottom), at three different developmental phases: 7 DIV, 13 DIV and 25 DIV, respectively from left to right at 2 different magnification factors (i.e. 10× and 20×, scale bars 100 μm and 50 μm, respectively). B. Bar graph of the total cell density on the two groups. No significant difference was found. C. Bar graph of the neuronal density at different DIVs on LG-SLG MEAs (red) and on control (black). Significant difference was found only at 13 DIV. 58
Figure 4.4 Optical micrograph of neuronal networks grown on a control MEA (top) and on a SLG-MEA (bottom) at different developmental ages. No morphological differences emerge from the comparison. 59
Figure 4.5 Developmental changes of hippocampal network activity of one representative graphene-transferred MEA and one control MEA. A. 10-s raster plots of spontaneous activity of a representative network cultured on conventional MEA, recorded by 60 electrodes at four different developmental phases: 7 DIV, 13 DIV, 19 DIV and 25 DIV, respectively from top to bottom. Each black dot represents a detected spike. B. 10-s raster plots of spontaneous activity recorded by 60 electrodes

covered by single-layer graphene at four different developmental phases: 7 DIV, 13 DIV, 19 DIV, 25 DIV, respectively from top to bottom. 64
Figure 4.6 Developmental profiles of hippocampal network cultured on graphene-transferred MEA (red) and conventional MEA (black). A. Mean firing rate (spikes/s) of 5 cultures on graphene-transferred MEA and 5 cultures on conventional MEA. The parameter was significantly different between two groups at 13 and 16 DIVs. B. Mean bursting rate (burst/min): the parameter was significantly different between two groups at 13, 19, 22 and 25 DIVs. C. Burst duration (ms): no statistical difference was found between the two groups. D. Percentage of spikes outside burst (IBR): the parameter was significantly different between two groups from 16 to 25 DIVs. All data are presented as mean±SEM. Statistical analysis has been performed by using the two sample t-test (*$p < 0.05$). 65
Figure 4.7 Cross Correlation Analysis. A) Box plots of the 100 strongest C peak values at each developmental time steps: 13, 16, 19, 22, 25 DIV for the control group (black box) and for the graphene (red box). We excluded the early developmental stage 7, 10 DIV since the level of activity was low. B) Box plots of the corresponding peak latency values (L peak) of the pre-selected 100 strongest C peak values. We considered only the peak latency values smaller than 50 ms. For each box plot (A–B), the small square indicates the mean, the central line illustrates the median and the box limits indicate the 25th and 75th percentiles. Whiskers represent the 5th and the 95th percentiles. Statistical Analysis was carried out using Mann-Whitney comparison test, *$p < 0.05$. 66
Figure 4.8 Evoked activity analysis of SLG-MEA versus conventional MEA (control). Response of the neuronal network activity to the stimulus (A). 72

List of Publications

Neuronal-like response of N2a living cells to nanoporous patterns of thin supported anodic alumina
A. El Merhie, M. Salerno *et al. (submitted to* Colloids and Surfaces B: Biointerfaces*)*

Single Layer Graphene functionalized MEA for enhanced detection of neuronal network development
A. El Merhie, D. Ito *et al. Sensors and Actuators B: Chemical*, 277, 224-233, August 2018

Step-by-step Surface Potential Tuning of Patterned Graphene by Polyelectrolyte Coating
M. Salerno, **A. El Merhie**, A. Diaspro, S. Dante. *Thin Solid Films.* 660, 253-257, June 2018

List of Conferences

Conference proceedings

CHO Cells on Uniform and Patterned SLG: Adhesion and Proliferation.
Amira El Merhie et al. European Biophysics Journal (2017) 46 (Suppl 1), S185

Oral contributions

ANNIC2018 (Berlin, Germany), October 2018
Amira El Merhie *et al.* – oral presentation
SLG Bio-interface: Enhanced CHO Proliferation and Boosted N2a Differentiation

ICONAN2018 (Rome, Italy), September 2018
Amira El Merhie *et al.* – oral presentation
SLG Bio-interface: Boosted N2a Differentiation and Enhanced Detection of Neuronal Network Development

Graphene2018 (Dresden, Germany), June 2018
Amira El Merhie *et al.* - oral presentation
SLG Functionalized MEA for Enhanced Detection of Neural Network Development

Poster presentations

19th IUPAB Congress & 11th EBSA Congress (Edinburgh, UK), July 2017
Amira El Merhie *et al.* – poster presentation
CHO Cells on Uniform and Patterned SLG: Adhesion and Proliferation

Graphene2017 (Barcelona, Spain), March 2017
Amira El Merhie *et al.* - poster presentation
Adhesion and Proliferation of CHO Cells on SLG

Awards

Best PhD Student Oral Presentation – Graphene2018 (Dresden, Germany) June 2018

Student Travel Grant – Graphene2018 (Dresden, Germany) June 2018

Student Poster Award – EBSA 2017 & the Biophysical Society (Edinburgh, UK) July 2017

Young Scientist Travel Award – 19th IUPAB Congress (Edinburgh, UK) July 2017

List of Abbreviations

APA, Anodic porous alumina
ATR-FTIR, Attenuated total reflectance – Fourier transform infrared spectroscopy
BD, Burst duration
CaF_2, Calcium fluoride
CHO, Chinese Hamster Ovary
Cu, Copper
CVD, Chemical vapor deposition
DAPI, 4′,6-diamidino-2-phenylindole
DIV, Days *in vitro*
DMEM, Dulbecco's Modified Eagle medium
DT, Differentiated threshold
FBS, Fetal bovine serum
FD, Force distance
G, Graphene
GRM, Graphene-related materials
QI, Quantitative imaging
hMSCs, human mesenchymal stem cells
IBR, Inverse burst ratio
KrF, Krypton fluoride
LG-SLG, Large grain single layer graphene
MAP2, Anti-microtubule associated protein 2
MBR, Mean bursting rate
MCS, Controlled thermostat
MEA, Multi-electrode array
MFR, Mean firing rate
MLG, Multi-layer graphene
NIR, Near infra-red
N2a, Neuroblastoma 2a
NSC, Neural stem cells
PBS, Phosphate buffered saline
PDL, Poly-D-lysine
PLP, Peak lifetime period
PMMA, Polymethyl methacrylate

PS, Penicillin Streptomycin
PSS, poly(sodium-4styrene sulfonate)
QI-AFM Quantitative Imaging AFM
RA, Retinoic acid
SEM, Scanning electron microscopy
Si, Silicon
SiO_2, Silicon Oxide
SKPM, Scanning Kelvin Probe Microscopy
SLG, Single layer graphene
SNR. Signal-to-noise ratio
SP, Surface potential
STORM, Stochastic optical reconstruction microscopy
TEM, Transmission electron microscopy
WCA, Water contact angle

Introduction

The objective of my Ph.D. thesis is the investigation of the role of Single Layer Graphene (SLG) as a biointerface for its possible future exploitation in various biomedical applications; in particular for the development of biosensors, substrates for regenerative medicine, interfacing platforms for better recording of electrophysiological activity of neuronal networks, among others. This Ph.D. project is multidisciplinary involving both the material transfer and characterization part from one side and the biological part from another side. The material part offers an in-depth explanation of SLG synthesis, transfer, characterization and functionalization while the biological section sheds light on the studies performed for investigation of the behavior of different types of cell lines on SLG substrates. For better understanding of the sequence of the performed work, I have divided this thesis into separate chapters. In the beginning and end of every chapter, I added an introduction and conclusions related to it.

Chapter 1 acts as a general introduction to graphene and graphene-related materials where a detailed explanation on the evolution of those materials as a cell interface is provided leading to the introduction of SLG in the end of this chapter along with its production process. Chapter 2 is oriented on the surface characterization of SLG substrates; in this chapter, I described the SLG transfer method, creation of the micrometric ablated geometric patterns on the transferred substrates using excimer laser micromachining, a technique developed in our lab, then further functionalization of the substrates and finally all the techniques employed for their physicochemical characterization. Chapter 3 is dedicated to the biological part of the project; i.e. studying the behavior of different cell lines on the SLG substrates. In this chapter, I have described and explained the interest of using the selected cell lines and the experiments that were performed on them. Chapter 4 has been devoted to a complete and separate project that I performed in collaboration with the Neuroscience and Brain Technologies

department. The main focus of the project was the functionalization of the commercial multi-electrode arrays (MEAs) with SLG and studying the neuronal network activity on them throughout the complete network development.

Although the main focus of my Ph.D. project was studying SLG biointerface, I have also been involved in side projects, among which, studying the neuronal-like response of mouse neuroblastoma (N2a) living cells to nanoporous patterns of thin supported anodic alumina which I have described in Appendix A, and studying the surface potential of graphene by polyelectrolyte coating which I have presented in Appendix B.

To summarize, this thesis reports an original investigation, since, to the best of our knowledge, there is no report yet about the study of the effect of SLG functionalized MEA on the neuronal network activity throughout the complete network maturation. Furthermore, proliferation curves of different cell lines on SLG versus control substrates have been presented; in addition to physicochemical characterization of ablated and functionalized SLG substrates as means of possible explanation of a certain cellular behavior on graphene.

CHAPTER 1:

Graphene as Cell Interface

1.1 Graphene

Variations in covalent bonding between carbon atoms leads to naturally occurring different materials called carbon allotropes. Each of them has distinctive physical and chemical properties owing to the unique spatial arrangement that carbon atoms adopt. Allotropes of carbon include graphite, diamond and carbon nanotubes (CNTs), among others. The atomic structure of graphite is characterized by the multiple stacking of one-atom thick sheets formed by carbon atoms arranged in a hexagonal lattice. The isolated two-dimensional crystal structures made of single atomic layers of graphite are called "graphene" (1). The existence of single graphene sheets had been discussed in theory more than 50 years ago. Yet, the existence of two-dimensional (2D), atomically thin crystal materials were considered physically impossible. In 2004, a single sheet of graphene was isolated and characterized by Novoselov and Geim (2). Since then, research on graphene has been increasing almost exponentially, attracting the interest of various scientific fields (1).

Graphene (G) is defined as a single- or few-layered sheet of sp^2-bonded carbon atoms tightly packed to a 2D honeycomb lattice (3). Each carbon atom has three μ-bonds and an out-of-plane π-bond that can bind with neighboring atoms, conferring graphene unique chemical and physical properties (3). The family members of graphene related materials (GRMs) include: single- and few-layered graphene (1–10 layers; G), graphene oxide (single layer, 1:1 C/O ratio; GO), reduced graphene oxide (rGO), graphite nano- and micro-platelets (more than 10 layers, but < 100 nm thickness and average lateral size in the order of the nm and μm, respectively), graphene and graphene oxide quantum dots, and a variety of hybridized graphene nanocomposites (4–6). The diversity among the GRMs is mainly dependent on the graphene production method; chemical vapor deposition (CVD) (7,8), mechanical cleavage (2), and electrochemical exfoliation of graphite (9), can in fact give the material a wide range

of specific properties based on the number of layers, lateral dimension, purity and defect density, conductivity, surface chemistry and shape (3,5,6,10,11).

G and GRMs (Fig. 1.1) also possess tunable and extreme mechanical strength, exceptionally high electronic and thermal conductivities, flexibility and transparency (2). Therefore, G has all the characteristics to play a key role in many applications, opening new advantageous opportunities in supercapacitors (12–14), flexible electronics (15,16), printable inks (17), batteries (18,19), optical and electrochemical sensors (20,21), and energy storage (22–24).

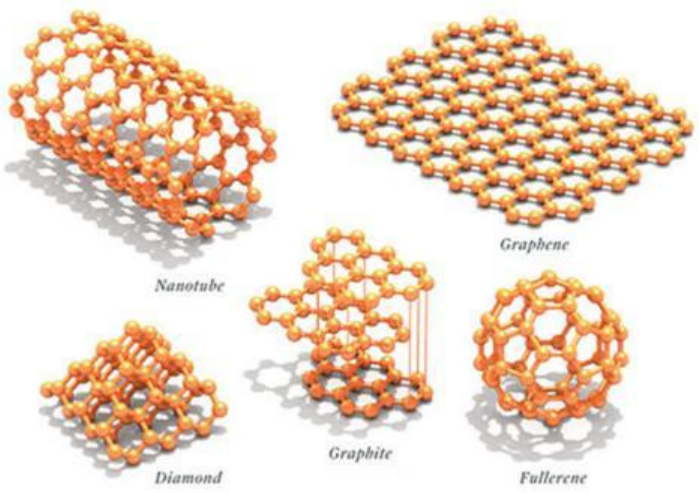

Figure 1.1 Graphene and graphene-related materials (25)

1.2 Graphene as a Biocompatible Material

In the last few years, biomedical applications of G have attracted an increasing interest, including the use of G and GRMs for bioelectrodes, bioimaging, drug/gene/peptide delivery, nanopore-based DNA-sequencing devices, stem cell differentiation and tissue engineering (26,27). Moreover, GRMs have generated great interests for the design of nanocarriers and nanoimaging tools, tissue scaffolds (both two- and three-dimensional), anti-bacterial coatings and biosensors (1,28,29).

1.2.1 Graphene as cell interface

Interfacing carbon-based materials with cells is considered to be important for regenerative medicine, implants, and neural prostheses, among other. Hence, it is important to find biocompatible and mechanically stable materials to be used as platforms driving cellular adhesion, proliferation and differentiation. Among carbon-based materials that have gained popularity for being used as biological interfaces have been CNTs (30). However, recently, among other carbon-based materials, G has attracted considerable interest as it possesses some exemplary properties, such as higher electrical conductivity and better mechanical and optical properties in comparison to CNTs (31–33). Possessing these properties, G has gained an increased popularity in various scientific and technological fields, as mentioned earlier. The exploitation of those properties could be useful for biomedical applications. Therefore, the use of G as a substrate for cell seeding has been tried. For example, an increase in the adhesion of osteoblasts and human mesenchymal stem cells (hMSCs) on G substrates has been previously demonstrated (34). Very recently, biomedical applications of G in nervous systems have attracted much attention (35,36). Concerning this, Convertino *et al* (37), demonstrated peripheral neural survival and growth on graphene substrates. In another study by Park *et al* (34), the influence of G on neural stem cells (NSCs) showing an enhanced differentiation of these cells into neurons rather than glial cells, which is required for neural regeneration and brain repair, has been shown. Last but not least, Li *et al* demonstrated a promoted neurite sprouting and the outgrowth of mouse hippocampal cells on graphene substrates (38). Despite the increasing number of studies in this field, the number of publications of the topic is still limited, and there is no universal consensus about what happens at graphene-cell interface, and, especially the reason that stands behind this is not completely clear.

Based on the literature review, most of graphene substrates, used for studying the differentiation of neuron-like cells and NSCs in addition to studying graphene-neuron interface, were produced by CVD (31,39,40). However, the gap in those studies lies in the unspecified number of G layers composing the

substrates (29); noting that the exact number of layers is important as it causes a great influence on the physico-chemical properties of a graphene-based platform (41,42). In a recent study (43), the effect of SLG (Fig. 1.2) and multi-layer graphene (MLG) on neuronal communication has been studied, and it has been demonstrated that SLG modifies neuronal excitability and up-regulates K+ currents of neurons that switch to functionally tonic phenotypes indicating that SLG enhances the functionality of neuronal network. This phenomenon has been observed when neurons were cultured on SLG only and not on MLG. Therefore, choosing SLG over other GRMs as a substrate to study SLG/biointerface has been a focus of my PhD project in order to study the behavior of cells over time on this substrate and to understand its physicochemical properties, with long term goal of employing it in regenerative medicine and for development of biosensors.

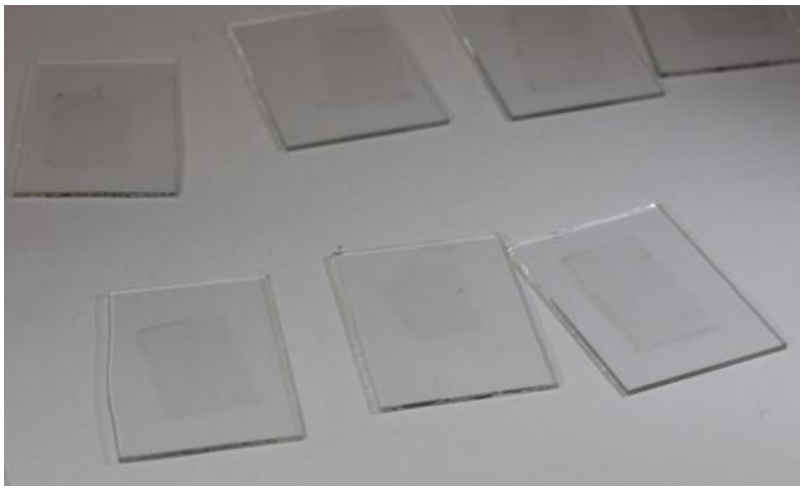

Figure 1.2 SLG on glass substrates (44)

1.2.2 Single Layer Graphene (SLG)

Among the several methods that have been devised for the production of high quality SLG (Fig. 1.2), the CVD method is the most promising, mostly used, and readily accessible approach for the deposition of reasonably high quality SLG onto transition-metal substrates such as Nickel (Ni), Palladium (Pd),

and Copper (Cu) (45). Also, this method has advantages such as being the most straightforward method to transfer graphene to any arbitrary substrates, in addition to being a good control over its number of layers. This fact led to shifting the attention towards the production of top quality SLG on crystalline Cu films. In this process, SLG is grown on 25μm thick Cu foils in a hot wall furnace (Fig 1.3). Initially, Cu foil is first annealed in hydrogen atmosphere at 1000°C, and then a mixture of H_2/CH_4 is introduced into the system to initiate the graphene growth. After a continuous graphene layer is formed on Cu foil, the system is cooled down to room temperature (Fig. 1.3) (46).

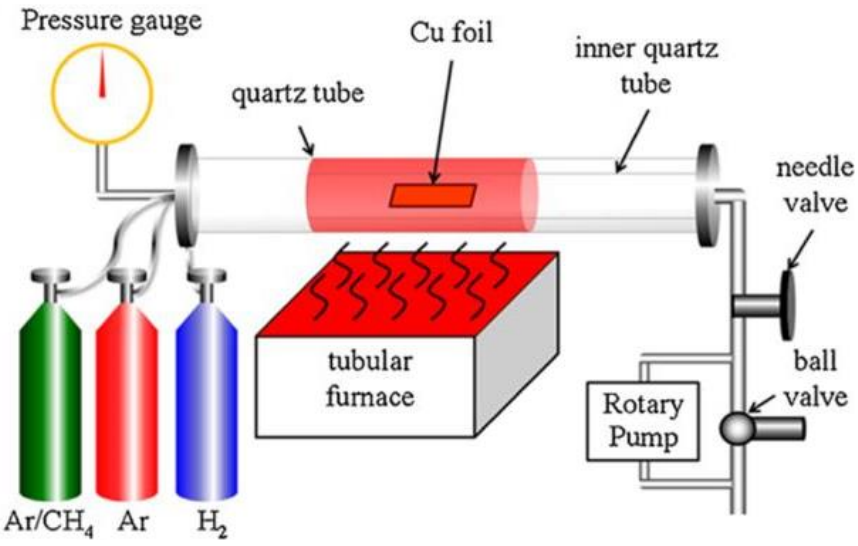

Figure 1.3 Schematic of a common setup for chemical vapor deposition of graphene (47)

Characterization of formed or fabricated SLG is an important part of research which involves measurements based on various microscopic and spectroscopic techniques. The outcome of such measurements involves the determination of the number of layers and the purity of samples in terms of presence or absence of defects. Optical contrast of graphene layers on different substrates is the most simple and effective method for the identification of the number of layers. Contrast in scanning electron microscopic (SEM) images is another way to determine the number of layers (48). Transmission electron microscopy (TEM) can be directly used to observe the number of layers on

viewing the edges of the sample (49). However, Raman spectroscopy has been extensively used as a non-destructive tool to probe the structural and electronic characteristics of graphene, being very powerful in distinguishing between single, double and multi-layer graphene (50).

The band structure of SLG is determined to have 2D characteristics and a linear dispersion relation of electronic wave functions with perfect electron-hole symmetry, in which the Fermi surface consists of two cones touching at one singular, so-called Dirac point, where the density of states is zero (33). These extraordinary electrical properties make SLG a good candidate for a wide range of high frequency applications, such as chemical sensors and biosensors. Additionally, SLG has inherently low electrical noise due to the quality of its crystal lattice and its 2D nature which can screen the charge fluctuations (51). The combination of the unique properties and potential characterization of graphene makes it as an ideal material for the fabrication of biosensors and for neuroengineering, for example in invasive implant technologies for brain biosensors and electrodes.

CHAPTER 2:

Surface Fabrication and Characterization

In my Ph.D. project, I used SLG substrates to perform experiments with living cells and to study their behavior over time. Moreover, I have performed the physico-chemical characterization of these substrates to gain information about the interplay between the interface and cell behavior.

It should be noted that in order for the SLG to be useful for biological applications, it has to be removed from the catalytic metal substrate and transferred onto an arbitrary substrate with a minimal amount of defects introduced into the target surface after the transfer procedure.

For this purpose, I used SLG transferred on glass (SLG/glass) to perform experiments with living cells and for Raman characterization, SLG on Silicon (Si) and Silicon Oxide (SiO_2) for Scanning Kelvin Probe Microscopy (SKPM) experiments and SLG on Calcium Fluoride (CaF_2) for attenuated total reflectance – Fourier transform infrared (ATR-FTIR) spectroscopy.

In this chapter, I described the SLG transfer procedure, patterning and functionalization (Fig. 2.1); in addition to the physico-chemical characterization techniques employed to characterize the substrates.

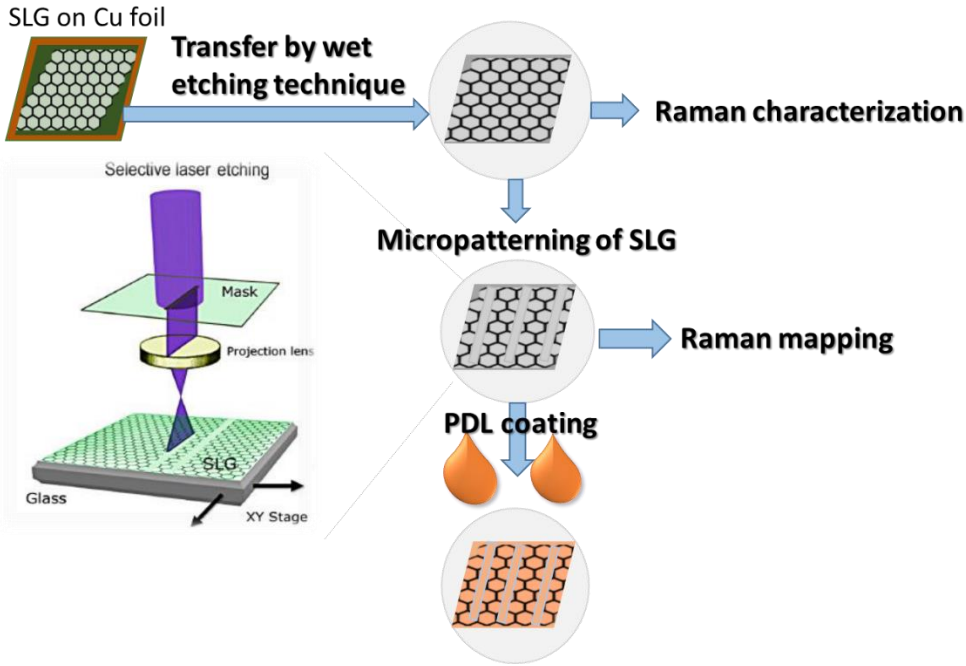

Figure 2.1 Schematic representation of SLG transfer, micropatterning, functionalization and characterization.

2.1 SLG Transfer

It should be clear that a successful and high quality SLG transfer process is the key point to the use of this material in many applications, since only clean SLG without wrinkles and ripples can provide high quality electronic and mechanical properties. For this purpose, I have optimized the transfer procedure to prepare clean and mechanically robust SLG on substrates of interest. In this section, I describe the transfer procedures used, sketched in Fig. 2.2.

SLG on Si and SiO_2 was a commercial product purchased from Graphene Supermarket. According to the manufacturer, SLG was transferred on the mentioned substrates by wet etching procedure and substrates were 285 nm thick.

As for the rest of the experiments mentioned beforehand, SLG produced by CVD on Cu foil was received from NEST group, IIT, Pisa, and the transfer by wet etching technique was performed following the procedure described herein.

A polymethyl metacrylate (PMMA) solution (MicroChem, 950,000 MW, 9–6 wt% in anisole) was spin-coated (Sawatec SM-180-BT spinner) on SLG/Cu foils at 3000 rpm for 45 s, and then the SLG on the opposite side of the Cu foil was removed by 100W oxygen plasma (180 s), followed by drying at room temperature for 12 h. The Cu was wet-etched using 0.2M Ammonium persulphate solution in a Petri dish and the PMMA/SLG stack was floated on the surface of the solution. The stack of PMMA/SLG was carefully rinsed in ultrapure water (Millipore, 18 MΩcm) to remove the traces of the Cu etchant, and was scooped on the target substrate (glass and CaF_2). The transferred SLG substrate was annealed in air at 150 °C for 3 h to obtain a firm adhesion to the target substrate and washed with acetone to remove any trace of organic contaminants. All the solvents were purchased from Sigma Aldrich. The quality of the SLG transfer was monitored by Raman spectroscopy.

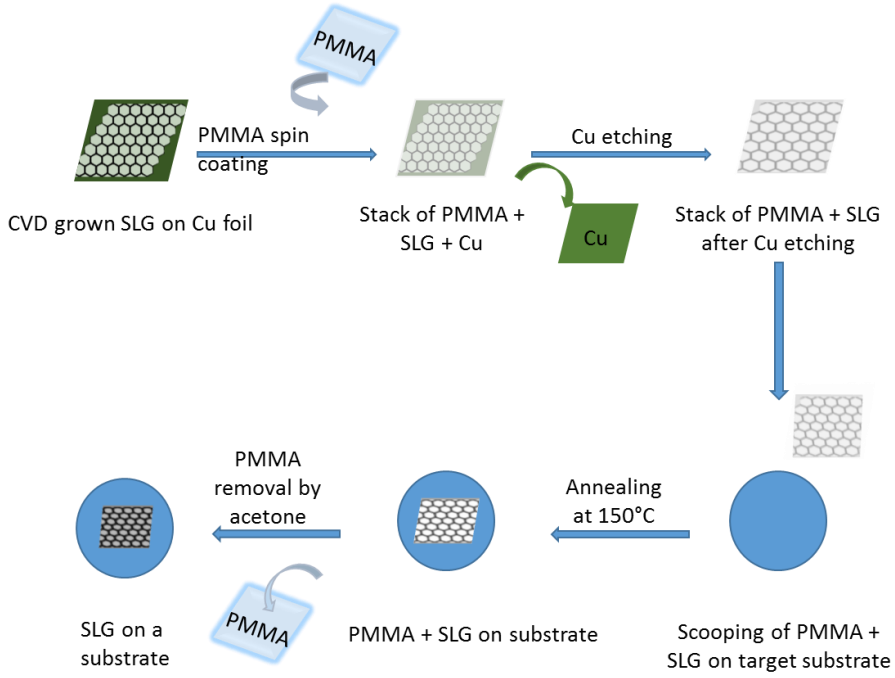

Figure 2.2 Schematic representation of the transfer of SLG from Cu foil onto glass coverslip.

2.2 Excimer Laser Micromachining of SLG

The beneficial effect of graphene in biomedical applications has been previously studied, such as, promoting effects on cellular behaviors, including cell adhesion, proliferation, development, spreading and differentiation. The precisely controlled cell migration or orientation plays a crucial role in determining cell responses and fates. In tissue engineering, patterning techniques play a vital role to understand the material interface of the anchored cells on the surface (52). For the fabrication of biosensors, the accurate positioning of biological ligands on substrates of interest is necessary for monitoring their behavior (53). Hence, the studies concerning the regulation of cellular behaviors by graphene substrates have been recently investigated.

The graphene patterned arrays have been especially under spotlight as a novel strategy for guiding and stimulating cellular behaviors as graphene can provide desirable topographical guidance cues as well as biochemical cues. For example, in one of the previous studies by Bajaj *et al* (54), the myogenic

differentiation of C2C12 skeletal muscle myoblasts on rectangular island-shaped graphene patterns on SiO_2/Si substrates fabricated using photolithography techniques. It has been observed that most myotubes were formed on graphene patterns while a few cells were differentiated into myotubes on the control substrates (SiO_2/Si).

Photolithography is the most widely used patterning technique for the cells on Si or on glass surface (55). Although photolithography is a technique that is highly developed for patterning features smaller than ~1 μm resolution, it is unnecessary for many applications of patterning in cell biology. Moreover, the high costs associated with equipment and the need for access to clean rooms, make this technique inconvenient for biologists.

Recently, there has been increased attention on pulsed laser ablation for surface micro-patterning and structuring of materials. The laser ablation with its single step process has numerous advantages for micromachining; high flexibility, direct patterning without the need for a resist process and also without the need for an etchant. In order to achieve high-quality ablation, it is necessary for the laser beam to be strongly absorbed by the materials (56).

Patterning SLG with micrometric or sub-micrometric resolution using laser micromachining showed immense potential for future development (56). The fact that SLG has an absorption peak in the deep UV at 4.6 eV was exploited to perform ablation patterning by a Krypton fluoride (KrF) Excimer laser of 248 nm wavelength (57). Recently the direct laser patterning on SLG was further optimized for hippocampal neuron patterning (56).

The SLG sheets transferred onto glass and Si substrates were subjected to micromachining by laser ablation (Fig. 2.3), with an aim to create patterns or local surface modification with micrometric or sub-micrometric resolution. The samples were exposed to laser pulses in ambient air. Patterned regions consisted of stripes or squares exposed to a single laser pulse with fluence of 0.5 $J.cm^{-2}$.

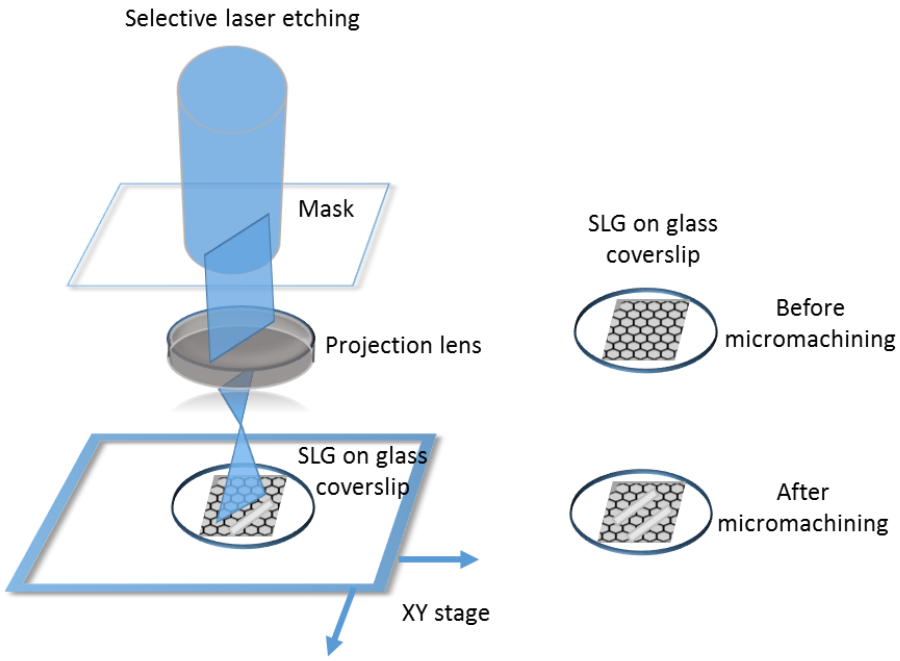

Figure 2.3 Laser micromachining - Schematic representation of micro-patterning by laser ablation on SLG.

2.3 Functionalization of SLG Substrates

Positively charged polyamino acids facilitate the attachment of cells and proteins onto solid surfaces in biological applications (58). Polylysine (Fig. 2.4), a homo-poly-amino acid characterized by the peptide bond between the carboxyl and ε-amino groups of lysine, shows a wide range of antimicrobial activity and is stable at high temperatures under both acidic and alkaline conditions. It represents the synthetic molecule mostly used as an unspecific adhesion factor to enhance cell adhesion in different applications.

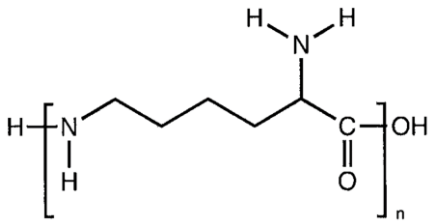

Figure 2.4 Chemical structure of polylysine (59)

In cell cultures, normal attachment, growth, and development of many cell types depend on attachment factors and extracellular matrix components. While some cells can synthesize these components, others require an exogenous source, particularly when grown in serum-free culture. Neurons are, however, distinctive cells with highly polarized morphology, much smaller somata, and thus few anchoring points for adhesion in comparison to most types of adherent mammalian cells. These features make the culturing of neurons a delicate process. To promote cell attachment, spreading, growth, morphology and differentiation, polyamino acids have been used as coating molecules (60). Polylysine enhances electrostatic interaction between negatively-charged ions of the cell membrane and positively charged surface ions of attachment factors on the culture surface (Fig. 2.5). When adsorbed to the culture surface, it increases the number of positively charged sites available for cell binding.

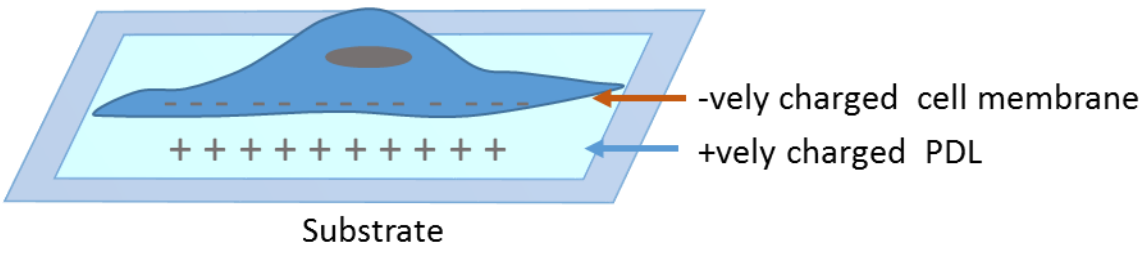

Figure 2.5 Surface interaction between positively charged polylysine and negatively-charged ions of the cell membrane.

In fact, its positively charged side groups (i.e., $-NH_2$ groups) interact electrostatically with the negatively charged cellular membrane. Besides increasing neural adhesion, polylysine enhances cell and neural, proliferation, and neurite extension (61).

For coating of SLG substrates used in my experiments, I used poly-D-lysine (PDL) (Sigma-Aldrich, MW 30.000–70.000). The substrates were coated with PDL (concentration of 0.1 $mg.ml^{-1}$ in sterile

water) for 3h in an incubator (37ºC, humid atmosphere with 5% CO_2), and thoroughly rinsed with sterile deionized water.

2.4 Physicochemical Characterization of SLG Substrates

2.4.1 Raman Characterization

To ensure the successful transfer of SLG, the substrates are characterized by Raman spectroscopy. This is a non-destructive technique widely used to quantify the defect density and crystallographic quality of carbonaceous products.

Analysis of the observed Raman spectra provides precise information on the electronic states, the phonon energy dispersion, and the electron-phonon interaction in sp^2 carbon systems. For SLG, the sp^2 hybridized electrons do not have an energy gap at the Fermi level, and thus one always gets a resonance condition for Raman spectra for any laser excitation energy. The Raman spectrum of graphene has three major bands: the D-band located around 1350 cm^{-1} that is a defect-induced band; the G-band located around 1580 cm^{-1} that is due to in-plane vibrations of the sp^2 carbon atoms; the 2D-band around 2700 cm^{-1} results from a two-phonon lattice vibration. Unlike the D-band, the 2D-band is not activated by the vicinity to a defect. A sharp and symmetric 2D-band is found in the case of SLG, as shown in Fig. 2.6. Therefore, to evaluate the success of the transfer procedure and the quality of the obtained SLG, Raman measurements on the samples have been carried out routinely at ambient conditions using a LabRAM HR800 spectrometer (Horiba Jobin Yvon, USA) equipped with a microscope, namely a μRaman system. A 633 nm wavelength excitation line was used, in backscattering geometry through a 50× objective lens. Fig. 2.5 displays a Raman spectrum obtained from SLG transferred onto a glass coverslip. The ratio of the intensities of the 2D and G-band, I_{2D}/I_G, and the sharp symmetric 2D band peak are indications of a good quality SLG, in spite of the presence of few defects (D-band).

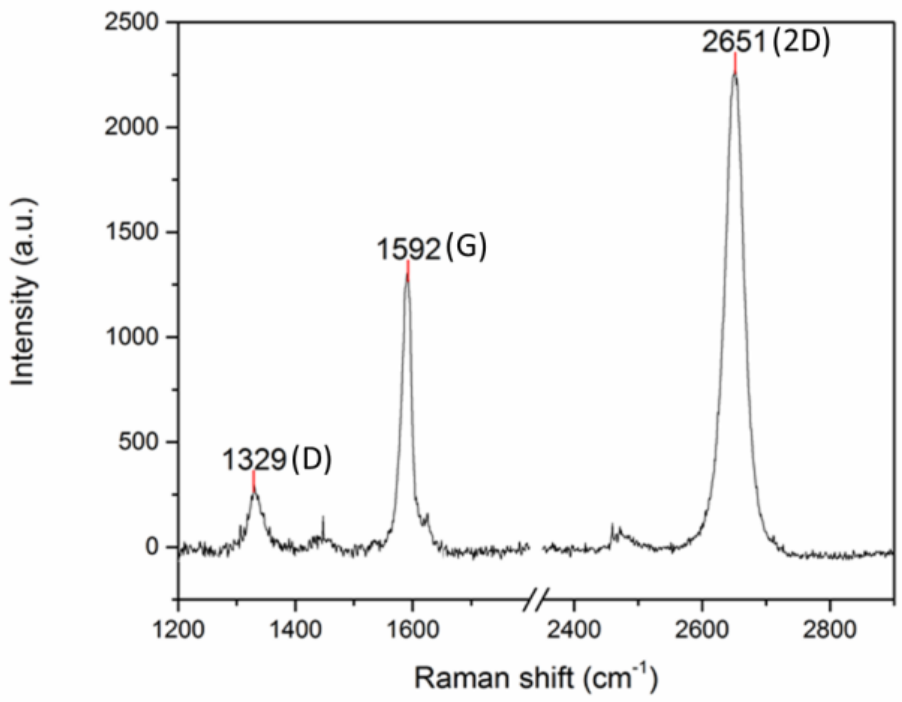

Figure 2.6 Raman analysis of SLG - Raman spectrum indicating the D, G and 2D peaks of SLG transferred onto a glass coverslip.

2.4.2 G-band and 2D-band Shift

In order to ensure the presence of the PDL layer on SLG substrates, I performed Raman characterization of those substrates after the PDL coating to see whether there were any changes in the Raman spectra. A shift in the G and 2D bands of SLG was observed (Fig. 2.7). The G band is shifted to the right by about 3 cm^{-1} and the 2D band is shifted to the right too by about 7 cm^{-1}. This shift known as the blue shift, accompanied by a slightly reduced width of the peak (Table 1), is an indication of the stiffening of the graphene vibrations as has been reported (62).

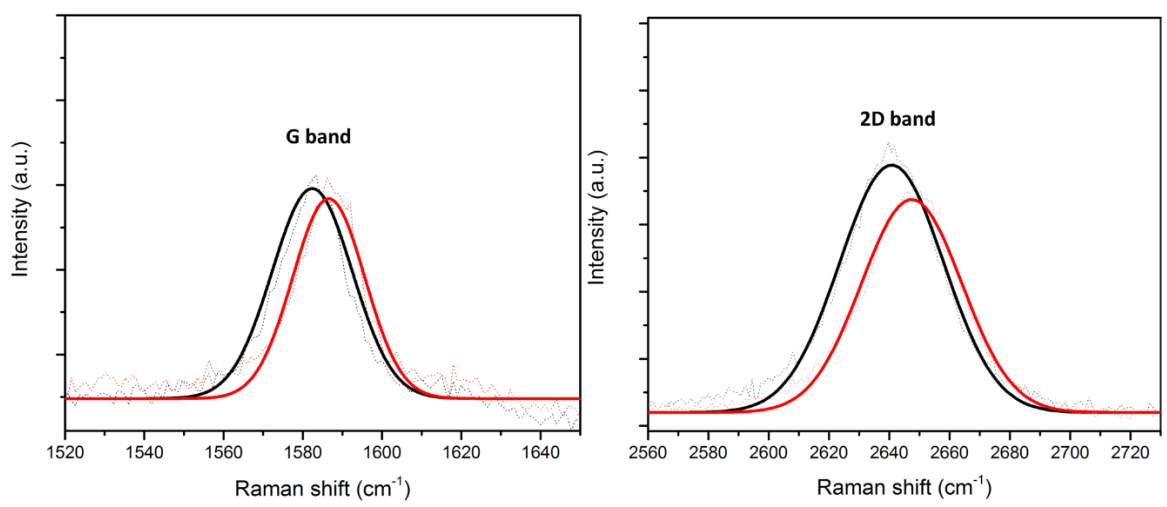

Figure 2.7 G-band and 2D-band Raman peak of bare SLG (black, dotted) and of PDL coated SLG (red, dotted). A progressive shift towards higher wavenumber is observable.

	G - peak position	G - peak width	2D – peak position	2D – peak width
Bare SLG	1583,3 ± 0,4	11,2 ± 0,4	2640,8 ± 1	34,4 ± 2,3
PDL/SLG	1586,5 ± 0,3	9,1 ± 0,3	2647,4 ± 1,1	33,2 ± 2,1

Table 1 Change of SLG Raman G and 2D peaks position and width before and after polymer coating, according to the best fitting curves in Fig. 2.7.

2.4.3 Raman Mapping

Raman intensity mapping was performed on SLG/ablated substrates in order to ensure the complete removal of SLG from the ablated regions.

Raman intensity maps averaged over a wide wavenumber region instead of single peak intensity allows a mapping that is more sensitive to SLG alteration due to photo exposure. Raman mapping has been performed over SLG and ablated regions as shown in Fig. 2.8(A), and the acquired Raman spectra are displayed in Fig. 2.8(B). In SLG region, pristine SLG Raman signal has been collected, in the SLG/ablated border, the spectra indicates a modification in SLG (i.e. a folded residual) while in the

ablated region, there is no significant Raman signal. This map clearly resolves the transition region between pristine and irradiated areas.

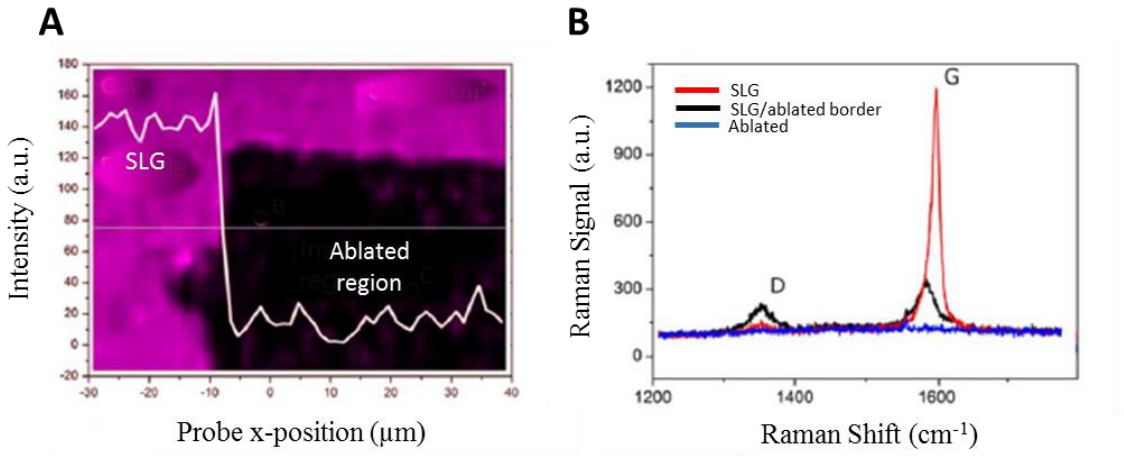

Figure 2.8 Raman component color map of the SLG, SLG/ablated border and the ablated region irradiated at 0.5 J/cm^2.

2.4.4 Pump-probe Microscopy

Pump-probe microscopy is another technique that I used to discriminate between the SLG and the ablated regions of the substrate.

It is defined as a non-linear optical microscopy technique which relies on *absorption-based* non-linear interactions of two input fields, called pump and probe, with the sample under study. Absorption-based measurements are advantageous because they permit to investigate non-emissive and dark states, broadening the range of available targets towards *weakly or non-fluorescent samples*.

Pump-probe methods were first introduced in time-resolved spectroscopy to resolve and monitor chemical and atomic ultrafast processes using two illumination pulses. A first high-intensity pump pulse is absorbed, perturbing the system from equilibrium, while a second weak probe pulse is used to measure the pump-induced population changes by monitoring its *transmission variations*. Kinetic

measurements can be performed varying the time delay between pump and probe pulses, while spectral measurements can be obtained varying the probe wavelength.

The implementation of these absorption-based methods in a *non-linear microscopy platform* with a proper detection scheme (63–66) permits to reconstruct spatial maps at the microscopic scale of the ultrafast phenomena under study, offering label-free non-fluorescence-based contrast capabilities.

Because of its non-fluorescent-based contrast, its high single-particle sensitivity and its high temporal resolution, pump-probe microscopy is extensively used in imaging and characterizing the carrier dynamics of metallic and semiconducting nanostructures for studying their optoelectronic properties (67–79).

Among nanomaterials, graphene recently started to be intensively studied for the development of novel electronic and optoelectronic devices (80). Due to its particular linear electronic band structure, it shows a wavelength-independent, broadband optical absorption (~ 2.3% per layer (81)) in the near infrared (NIR) part of the spectrum (82). This makes absorption-based pump-probe microscopy as an ideal technique for studying its carrier dynamics and for performing imaging, mainly using NIR wavelengths (83–96). What is expected is that the absorption of the pump beam will decrease the absorption coefficient of the graphene for a subsequent probe beam, thus the probe beam will be transmitted more due to the presence of the pump. This change in transmission is the pump-probe signal that will give the desired contrast for pump-probe imaging.

Measurements have been performed using the custom NIR pump-probe setup present at the Nikon Imaging Center of IIT, which is realized by coupling a tunable mode-locked femtosecond pulsed Ti:sapphire laser (680-1080 nm, 80 MHz, 140 fs, Chameleon Ultra II, Coherent) with a laser scanning Nikon C2 scan head and a Nikon Eclipse FN1 upright microscope body (Nikon Instruments). Measurements have been carried out by my colleague, a Ph.D. student of my cycle, Giulia Zanini (Details about the setup and measurements are explained in her dissertation).

To perform the measurements, the graphene/ablated substrate was placed on a 3-axis piezo-electric stage (P-611.3S NanoCube®, Physik Instrumente, travel range 100 µm × 100 µm × 100 µm, resolution 1 nm) which enables 3D image acquisition. Image analysis was performed with ImageJ/Fiji (NIH) (97). For the measurements of my substrates, pump beam was tuned to 800 nm while probe beam was tuned to 1030 nm. Both wavelengths fall in the wide absorption band of graphene. Powers of both beams were kept below 5 mW at the sample. No sample damages were seen at those powers.

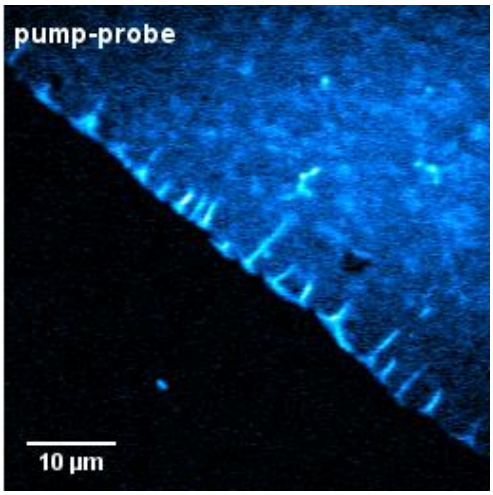

Figure 2.9 Pump-probe microscopy image of SLG/ablated substrate

Fig. 2.9 displays the SLG/ablated substrate where the border between SLG and the ablated stripes can be easily observed.

The advantages of using this technique are the following:

- It permits to image non-fluorescence graphene with high contrast, single layer sensitivity, and in short time
- It allows to perform the measurements in relative short time, opposite to the Raman mapping measurements that last longer
- It offers large field of view 127x127 um^2 (large area)
- 256x256 pixel, 20us/px, 1.3 s/frame (short time)

- It gives the possibility to measure the dimensions of the ablated stripes, the width of the stripes, and compare with the parameters initially set on the ablation laser micromachining device
- It allows to see the defects on the graphene layer (brightest spots are multilayer regions, while dark areas correspond to holes in the graphene)

2.4.5 Scanning Kelvin Probe Microscopy (SKPM)

With the aim of gaining more insight on the physico-chemical properties of the patterned (and PDL coated) SLG substrates, I focused my attention on studying the surface potential (SP). For this, I have used SKPM to measure the SP of the patterned SLG substrates.

The measurements were carried out on an atomic force microscope MFP-3D (Asylum Research, CA, USA), acquiring images at maximum scan size of 90 μm, with 2562 pixels, at a (single) line scan frequency of 0.2 Hz. A MESP probe (Bruker, MA, USA) was used, with nominal properties as follows: cantilever resonance frequency of ~75 kHz and Co-Cr coating on the tip of ~30 nm, resulting in a final tip diameter of ~70 nm. The tip work function Φtip, after calibration on highly oriented pyrolytic graphite (HOPG), assumed to have ΦHOPG=4.65 eV (56), appeared to be ~4.61 eV. The samples were back contacted at their bottom on a metal puck support.

The SKPM technique relies on double-pass method (Fig. 2.10), where each line is scanned first in tapping-mode to track the surface topography and then is scanned again at a set elevation height (50 nm in my case) to avoid topographical artifacts. During the elevated scan, the cantilever is dithered electrically, by applying a tip voltage (with sample substrate set to ground) consisting of a DC and an AC component (the latter at the resonance frequency). A feedback circuit cancels out the force on the probe by tuning the DC voltage component, which thus equals the local SP value.

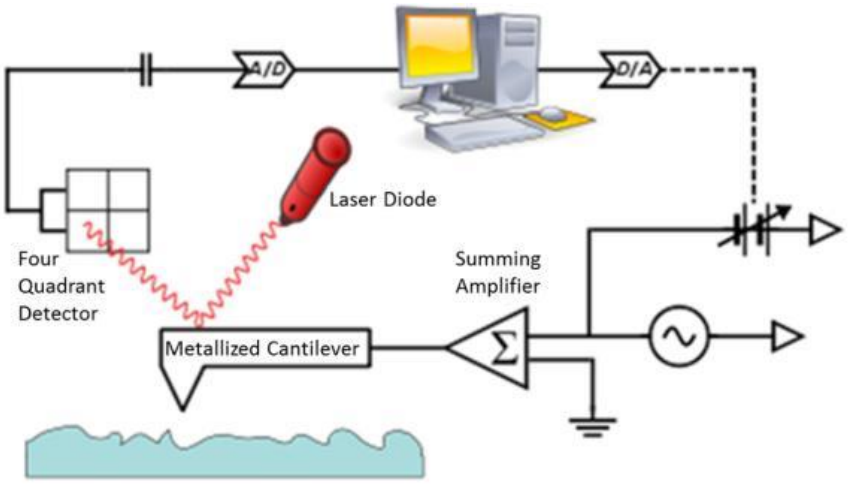

Figure 2.10 A schematic representation of Kelvin probe force microscopy (98)

As visible in the topographic image of Fig. 2.11, the patterning was carried out successfully with micrometric resolution, and the ablated graphene squares showed a clear, flat bottom of non-modified substrate, as well as intact surrounding graphene regions. As the only side-effect of ablation, several debris particles appear in the image, especially at the square edges. The SP map obtained in the same scanned area is displayed in the same figure (Fig. 2.11) A striking contrast in SP is observed. When averaging among several different regions, the values of the contrast at the squares and of the graphene background (mean ± standard deviation) were 143 ± 22 mV and−440 ± 60 mV, respectively.

The following step of the experiment was the coating of the surface with the positively charged PDL to modify the local SP. The interest in studying this specific coating comes, as mentioned earlier, from the use of PDL as cell adhesive layer (60) (for more information on this study and the measurements performed with negatively charged polyelectrolyte, poly(sodium-4styrene sulfonate) (PSS), refer to Appendix B). After immersing the sample in the PDL solution, I repeated the characterization previously performed on the graphene coated Si. In this case, I was certain that PDL was coating both the SLG and the ablated region due to the previous study performed in our lab by using fluorescently labelled PDL (56); this study allowed the direct visualization of fluorescence in correspondence of the

ablated region. On SLG, as expected (99) the fluorescence was quenched, but the presence of PDL was confirmed by Raman spectroscopy.

AFM topography and surface potential maps after PDL coating are reported in the second row of Fig. 2.11 (D) (namely panels 2D-F). No major differences are detected in the topography after PDL coating as compared to the pristine surface.

Indeed, it is assumed that both regions (ablated squares and surrounding graphene) are equally coated with PDL, being both negative, and this conformal coating does not give rise to a different depth of the topographic step at the squares. However, the effective PDL coating is observed in the SP image (Fig. 2.11 (E)), as a shift of the SP towards less negative values (−155 ± 55 mV). Incidentally, the contrast between the two regions was not varied. Moreover, preliminary indications exist that by changing the substrate (from Si to SiO_2), the contrast itself at the ablated regions can be chosen either positive or negative.

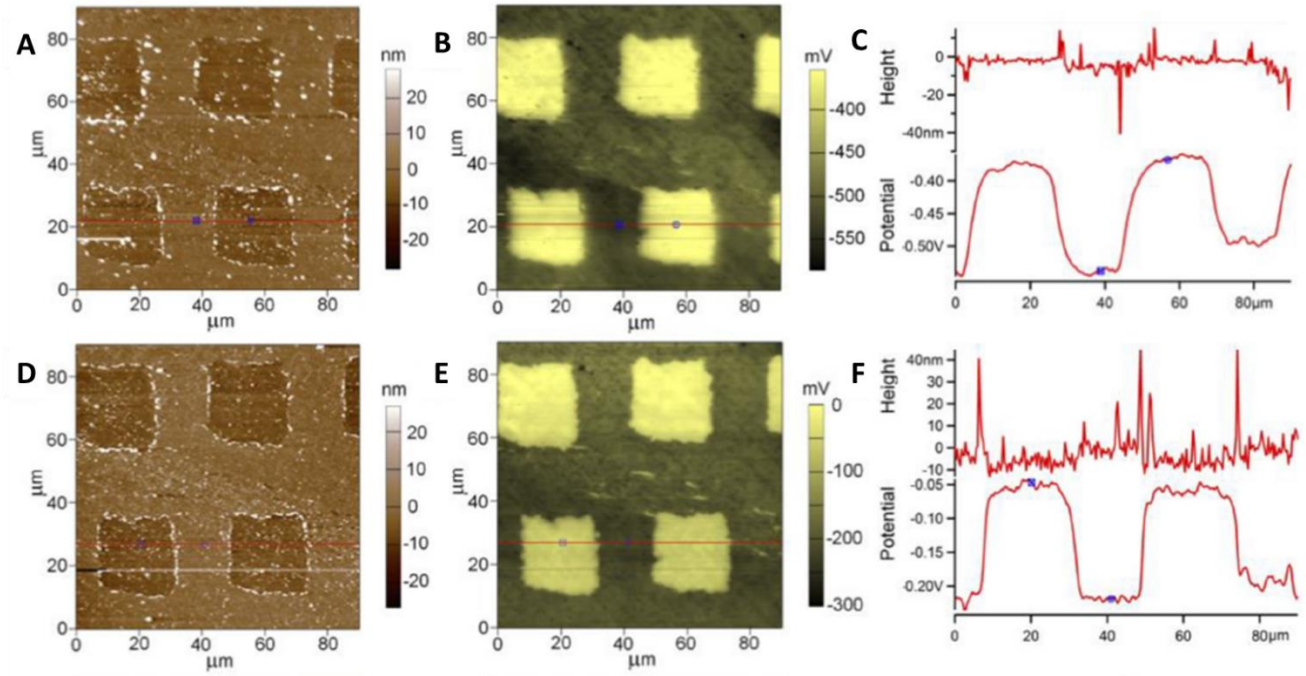

Figure 2.11 AFM topography of the patterned substrate before (A) and after PDL coating (D). Center: SKPM maps of the same region, showing a higher potential in correspondence of the ablated squares (B, E). Scan line profiles of topography and surface potential (C, F).

In another set of experiments, commercial SLG on SiO_2 was used for laser patterning and for the subsequent characterization by SKPM. The results (Fig. 2.12) showed a reverse contrast between graphene and the ablated squares of SiO_2, indicating that the contrast sign of the patterned region can be appropriately chosen by changing the substrate for graphene transfer.

The tuning of this surface property can find useful application, since many interfacial phenomena are regulated by electrostatics.

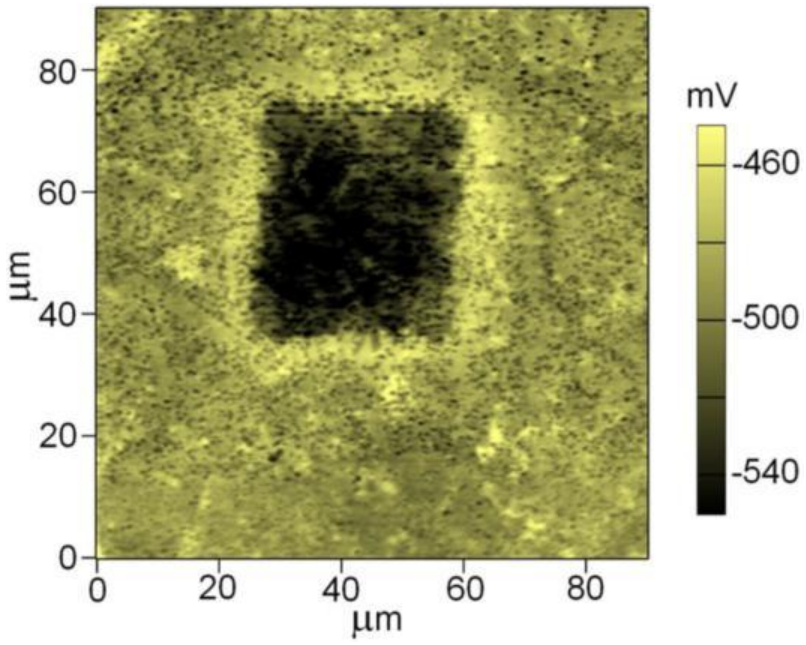

Figure 2.12 SP contrast at the surface of a SLG sample transferred on SiO2: the SP on the ablated squares is lower than on SLG background.

2.4.6 Water Contact Angle (WCA)

Water contact angle (WCA) measurements of surfaces have been widely used because they give a rapid idea about the presence of hydrophilic/hydrophobic domains on them (Fig 2.13). WCA represents an easy, fast and non-destructive technique. It relies on the affinity between a water drop and a surface: when the drop is placed onto the surface, if the surface is hydrophilic, the drop ill spread while if the

surface is hydrophobic, the drop will bead up. This behavior is determined by a force balance between adhesive forces between the liquid and the solid that tend to make the drop spread across the surface, and cohesive forces within the liquid that tend to make the drop ball up and avoid contact with the surface. In the general case, the angle between the tangent to the drop at its edge contact with the surface and the surface plane, the WCA, is measured, and it provides an estimation of the surface wettability by water.

As illustrated in Fig. 2.13, WCA<90° means that wetting of the surface is favorable, and the water will spread over a large area (hydrophilic surface), while WCA>90° means that wetting of the surface is unfavorable (hydrophobic surface). Superhydrophobic surfaces have WCA>150°, showing very little contact area between the drop and the surface. In my study, I measured the WCA to investigate the surface properties of the glass coverslip, SLG and ablated regions, with and without the PDL coating. The modified substrate was tested after incubation with PDL for 3 h reproducing the PDL coating procedure of substrates used in the experiments with living cells.

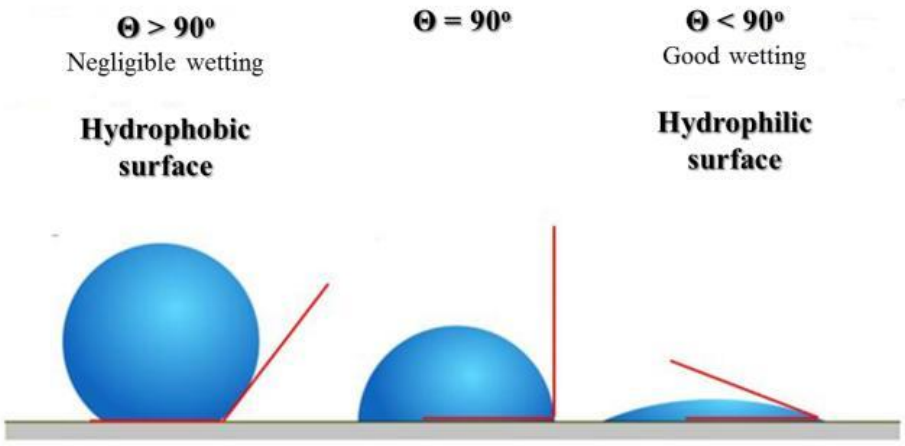

Figure 2.13 Schematic representation of contact angles formed by sessile liquid drops on a smooth homogeneous surface.

To study the relationship between the bare and modified substrate, ten different spots at random locations on each substrate were analyzed and three substrates for each sample were tested.

In Fig. 2.14, the values of WCA measured with sessile drop method on the surfaces of interest are shown. On the bare substrates without PDL, namely ablated SLG, SLG and glass coverslips, the WCA values observed (mean ± standard deviation) were 77°±2°, 79°±1°, and 29°±2.5°, respectively. After the surface modification with PDL, the WCAs changed into 76°±1°, 66°±1.4°, and 19°±1.4°, respectively. I can infer that after the PDL coating, the glass coverslips and SLG become clearly hydrophilic, but the ablated SLG still remains comparatively hydrophobic. In particular, the differences are statistically significant for the comparisons of bare glass to PDL glass ($p<0.001$), bare SLG to PDL SLG ($p<0.001$) and PDL ablated to PDL SLG ($p<0.05$). The change in behavior between SLG and ablated SLG substrates may be due to the functional groups of the polylysine that are exposed over the surface, but this does not seem to alter the wetting of the ablated SLG regions.

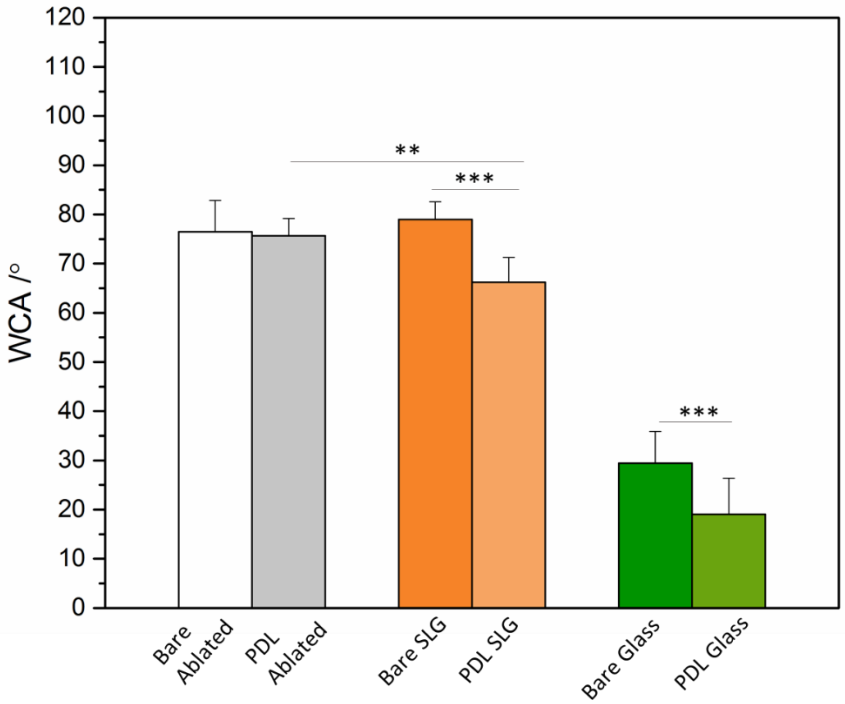

Figure 2.14 WCA on different surfaces (mean ± standard deviation). Pairs joined by lines show statistically significant difference (**: $p<0.01$, ***: $p<0.001$).

2.4.7 ATR-FTIR

Attenuated Total Reflection (ATR) spectroscopy is a technique where a beam of infrared light is passed through a crystal which allows total internal reflection. The infrared beam penetrates the surface of a liquid or solid sample, and the eventual signal profile received at the detector can be used to characterize the sample. The effectiveness of ATR spectroscopy has been further enhanced by use in conjunction with Fourier Transform Infrared Spectroscopy (FTIR) (Fig. 2.15), knowing that the Infrared spectroscopy is a useful technique for the determination of conformation and orientation of membrane-associated proteins and lipids. The technique is especially powerful for detecting conformational changes by recording spectral differences before and after perturbations in physiological solution (100,101).

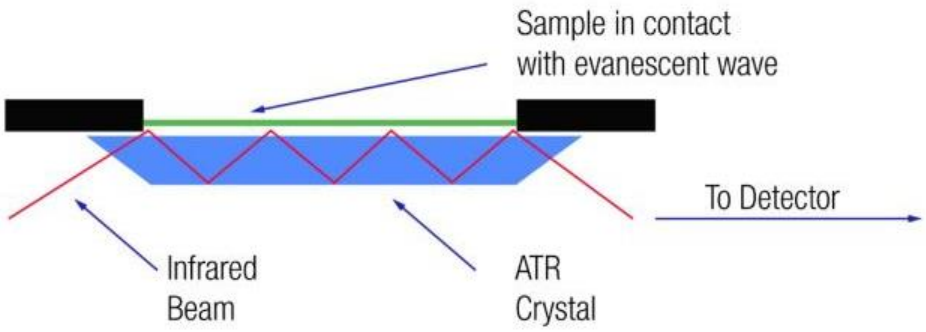

Figure 2.15 A schematic representation of the principle of ATR-FTIR (100)

For my experiments, I used CaF_2 as a substrate, and I performed ATR-FTIR measurements on PDL coated SLG/CaF_2 and PDL (10 $mg.ml^{-1}$) coated CaF_2 as a control, initially I tried with the concentration of 0.1 $mg.ml^{-1}$ that I used for coating of the substrates for the experiments with living cells, but since that concentration was not enough for obtaining high intensity of the measurements, I increased it until I obtained a signal. The samples were coated with PDL using drop casting method following the same method used for functionalization of the substrates for experiments with living cells

(section 2.3). Infrared spectra were obtained with a single-reflection ATR accessory (MIRacle ATR, PIKE Technologies) equipped with a diamond crystal and coupled to a Fourier Transform Infrared (FTIR) spectrometer (Equinox 70 FT-IR, Bruker). All spectra were recorded in the range from 3800 to 600 cm^{-1} with a resolution of 4 cm^{-1}, accumulating 128 scans.

Hence, PDL and PDL-SLG samples were chemically characterized by ATR-FTIR spectroscopy (Fig. 2.16). Main spectral differences were observed in the spectral regions between 3600 and 3000 cm^{-1} associated with the N-H stretching mode in different molecular environments, Fig. 2.16(A), and between 1900 and 1400 cm^{-1} ascribed to the C=O stretching mode and to Amide I and II bands as well as the bending mode of CH_2 groups, Fig. 2.16(B) (101–103). As displayed in Fig. 2.16(A), there was a redshift from 3299 to 3282 cm^{-1} (*i.e.*, a decrease of 17 cm^{-1}) of the proton mode of NH-CO in β-sheet structures when graphene was present. This could be related to changes in this secondary structure. In addition, the relative intensity of the N-H stretching mode attributed to random coils was increased for PDL-SLG, indicating that those had a higher contribution in PDL structure. Furthermore, a small decrease of the N-H stretching mode assigned to $–NH_3^+$ groups was also observed for PDL-SLG in comparison to PDL, most probably because of a lack of interaction between non-polar graphene layers and charged ammonia groups. On the other hand, some important changes were detected at lower wavenumbers, Fig. 2.16(B). While Amide II and $\delta(CH_2)$ were practically unaltered, the sample with graphene showed a considerable reduction of the relative intensity of the Amide I band and the occurrence of a new peak at ~1736 cm^{-1}. This last vibration has been previously attributed to free –COOH groups (*viz.*,disassociated or non-interacting by H-bonds carboxyl groups) of lysine and detected in some poly(lysine) (102,104). However, considering also the above mentioned decrease of the Amide I, a significant change of the secondary structure of the protein can be not excluded.

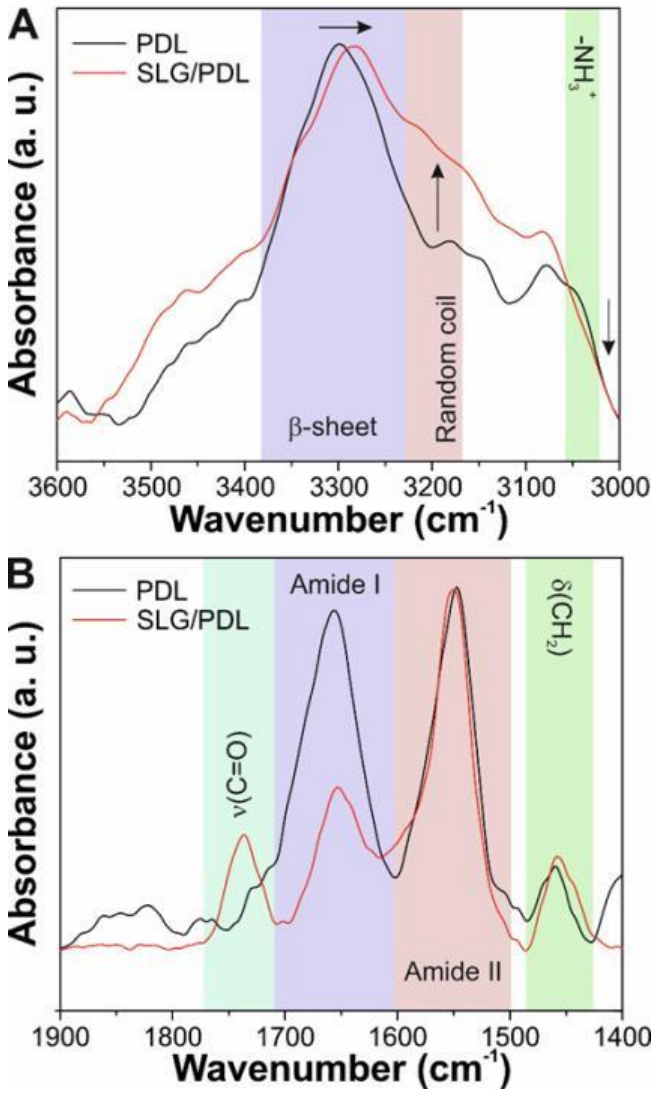

Figure 2.16 A, B, infrared spectra of PDL and SLG/PDL samples in the 3600-3000 and 1900-1400cm^{-1} regions, respectively. Arrows in A are used as guides to highlight the observed changes.

2.4.8 AFM-Quantitative imaging

The adhesion of bare SLG, bare ablated, PDL-coated SLG and PDL-coated ablated substrates was investigated by using a Nanowizard III AFM system (JPK Instruments) in the quantitative imaging (QI) mode. An Axio Observer D1 inverted optical microscope (Carl Zeiss, Germany), coupled with the AFM system, and was used to choose the areas for the mechanical analysis. V-shaped DNP silicon

nitride cantilevers (Bruker, Billerica, MA, USA), with a nominal spring constant 0.24 $N.m^{-1}$, the resonance frequency in the air in the 40‑70 kHz range and tip typical curvature radius of 20‑60 nm were used. The actual spring constant of each cantilever was determined *in situ*, using the thermal noise method. The acquisition of a large set of force‑distance (FD) curves (128 × 128) was performed in PBS with maximum force load of 2 nN and curve length of 100 nm. QI images of 100 × 100 μm^2 were collected. The adhesive properties of the sample were extracted from the post-processing analysis of the acquired force-distance (FD) curves. Fig. 2.17 shows the typical retraction part of the FD curve. The total area delimited by the part of the retracted curve below the FD curve baseline provides the evaluation of the detachment work (W_{detach}), i.e. the physical quantity that we take into account to characterize the adhesion properties on the two parts of the patterned substrate (105).

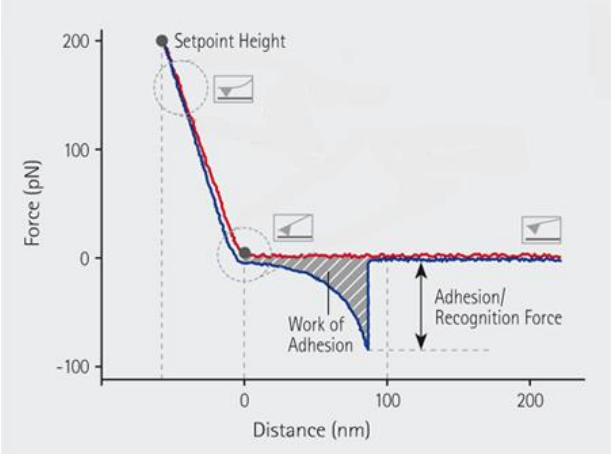

Figure 2.17 Force-distance curve (106).

Hence, we performed a quantification of adhesion properties of the interface by quantitative imaging. For this purpose, the adhesion Force and detachment work of the AFM tip from the surface were quantified. We performed experiments with the tip functionalized with PDL and without PDL. We performed experiments with bare tip on bare substrates, bare tip on PDL coated substrates, PDL coated tip on bare substrates, and PDL coated tip on PDL substrates. The curves were acquired on large

regions, containing both SLG and ablated squares. After the global post-processing of all acquired curves, histograms of F and W in the region of interest were extracted. The results demonstrated higher adhesion in correspondence of the SLG region (Fig. 2.18), especially in the experiments with bare tip and PDL coated substrates which interest us the most. In this case, the tip represents living cells and the way they react to the PDL coated substrates. The adhesion force (F_{adh}) was much higher on PDL-SLG (around 6 nN) as compared with the PDL-ablated (<2 nN). PDL coated tip on bare substrates represents how PDL reacts to this substrates when deposited on them, where again we observed higher F_{adh} on SLG versus ablated.

Clearly, the PDL polymer arranges differently on SLG with respect to the ablated part (confirmed by the ATR-FTIR measurements, section 2.16), possibly exposing a larger number of charged groups on its surfaces and providing a larger number of binding sites to the cell membrane.

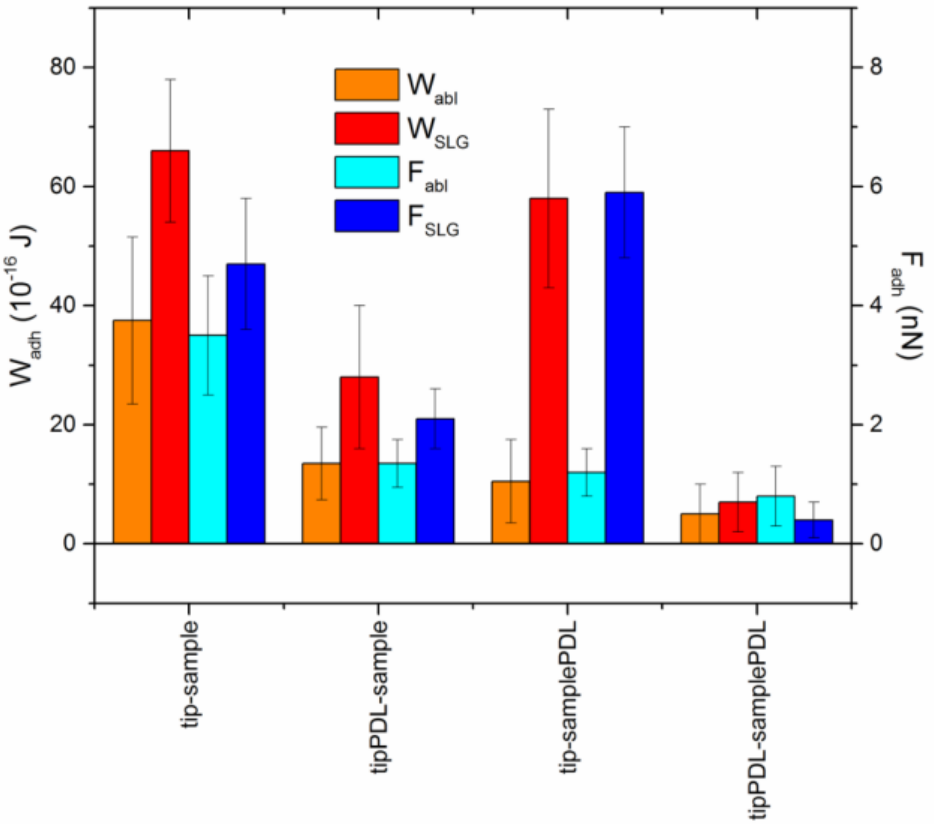

Figure 2.18 F_{adh} and W_{adh} on SLG and ablated substrates, coated with PDL and not.

2.5 Conclusions

In this chapter, I have presented different physico-chemical characterization techniques that I employed for characterizing my SLG and ablated/SLG substrates, bare and PDL coated, in order to understand how the substrates affect the PDL coating and to interpret their effect on cellular behavior. The characterization experiments have been performed in parallel with the experiments with living cells to understand how these substrates affect cell behavior since I have observed different cell behavior during my experiments (see details in the following chapter, Chapter 3).

From the results that I have presented in this chapter, I observed that several physico-chemical parameters were different on SLG with respect to glass and/or ablated regions; in particular I observed differences in WCA and SP. Due to these differences, the adhesion molecule PDL had a different structure, as detected by ATR-FTIR, and higher affinity to the substrate, as measured by QI-AFM. All these parameters have an influence on cell behavior.

CHAPTER 3:

SLG Bio-interface

Interfacing carbon-based materials with cells is considered to be important for regenerative medicine, implants, and neural prostheses, among other. It is important to search for biocompatible and mechanically stable materials to be used as platforms driving cellular adhesion, proliferation and differentiation depending on the application settings. As mentioned earlier, among carbon-based materials, graphene has attracted considerable interest as it possesses exemplary properties that led to its increased popularity in various scientific and technological fields, such as biophysics and biotechnology (40). These include drug delivery, disease diagnosis, ultra-sensitive biosensing and tissue engineering. Very recently, biomedical applications of graphene in nervous systems have attracted much attention (107). Concerning this, Park *et al* demonstrated the influence of graphene on neural stem cells (NSCs) showing an enhanced differentiation of these cells into neurons rather than glial cells which is required for neural regeneration and brain repair (34). Li *et al* demonstrated a promoted neurite sprouting and the outgrowth of mouse hippocampal cells on graphene substrates (38). In another study, by Convertino *et al*, peripheral neural survival and growth has been demonstrated on graphene substrates (37).

Based on my literature review, most of graphene substrates, used for studying the differentiation of neuron-like cells and neural stem cells (NSCs) in addition to studying graphene-neuron interface, were produced by CVD (31,107). In a recent study (43), the effect of SLG and MLG on neuronal communication has been studied, and it has been demonstrated that SLG modifies neuronal excitability and up-regulates K+ currents of neurons that switch to functionally tonic phenotypes when cultured on SLG while those effects are not mimicked by MLG, thus showing that SLG is a desired substrate for the enhancement of neuronal network activity.

Since the main focus of my PhD project was exploring and studying the effect of SLG substrates on different cell lines; including their behavior, migration, proliferation, and differentiation, I decided to explore the effect of those substrates on the differentiation of neuroblastoma cell lines. The idea of this

project was mainly based on the fact that the ability to differentiate neuron-like cells into neurons, and of desired type based on the application, is important for application in tissue engineering and regenerative medicine.

I used Neuro 2A (N2a) cell line, a mouse neuroblastoma cell line, that has been extensively used to study neuronal differentiation, axonal growth and signaling pathways. N2a cells possess the property of responding quickly to serum deprivation and other stimuli in their environment thus undergoing neuronal differentiation and neurite growth (109). Efficient differentiation of N2a cells on functionalized single walled carbon nanotubes has been demonstrated (108). Another study (109), showed the differentiation of N2a cells into dopamine neurons under specific conditions.

In this chapter, I have described the study that I performed in order to explore the effect of SLG substrates on N2a differentiation with the retinoic acid (RA) treatment and without.

I have also studied the effect of SLG versus ablated/SLG on the differentiation of this cell line. I have used ablated/SLG substrates in order to study whether the behavior of cells on this kind of substrates is cell line specific. Previous studies have been conducted on those substrates in our group that demonstrated ordered neuronal network growth on patterned SLG substrates (31,56). Hence, I wanted to study the behavior of other cell lines to determine how cell-dependent the behavior of cells is on this kind of substrates.

For my experiments, I used SLG on glass coverslips that was transferred, functionalized and characterized following the procedures described in Chapter 2.

3.1 Cell Culture

The N2a, mouse neuroblastoma, cell line (ATCC CCL-131) was maintained as a monolayer in Dulbecco's Modified Eagle medium (DMEM) (Gibco, UK), 10% Fetal Bovine Serum Inactivated (FBS), and 1% Penicillin Streptomycin (PS) at 37^0C with 5% CO_2 and used in the experiments between passages 20-24. The cells were split every 3 - 4 days, at a confluency <80%. The cells were seeded on

substrates of interest (255 cells/mm^2), in triplicates, and left in culture for 48 h when they reached the level of confluency allowing performing quantitative analysis for cell viability and neuritogenesis.

3.2 Assessment of Cell Viability

The calcein AM/ethidium homodimer live/dead assay (Invitrogen Co., Carlsbad, CA, US) was employed to quantify the N2a cell viability on SLG substrates, either coated or not with PDL. Calcein AM is a cell-permanent dye that is changed to green fluorescent calcein in live cells through the action of intracellular esterases. Ethidium homodimer is a DNA-binding dye that enters the damaged membrane of dead cells and gives red fluorescence. Cells were treated with live/dead assay after 48 h (same incubation time as used for the experiments of differentiation) of culture on substrates of interest, in duplicates, at 37^{0}C with 5% CO_2. Fluorescence images were captured using a Nikon Inverted Microscope TiE equipped with a confocal microscope (Nikon Optical Co., Ltd., Japan) at excitation wavelengths λ= 405 nm at a magnification of 10x. Survival of most of the seeded cells was observed (Fig. 3.1).

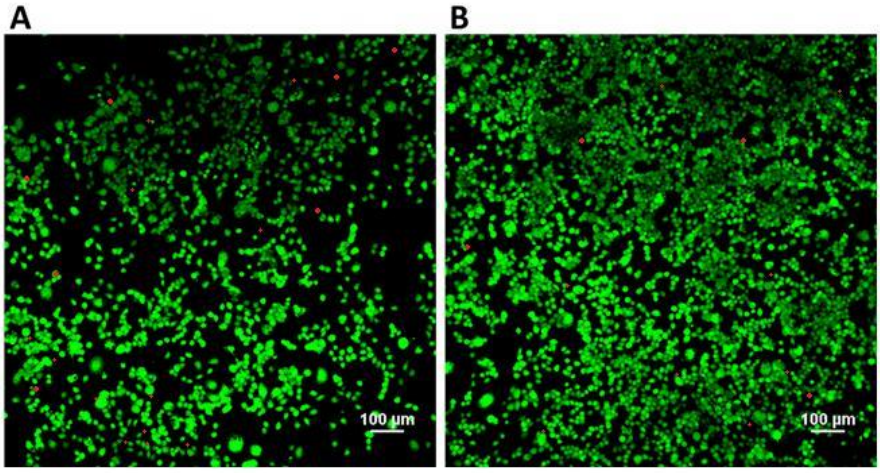

Figure 3.1 Confocal images of N2a cells incubated on bare SLG (A) and PDL/SLG (B) substrates for 48 h treated with live/dead assay kit.

3.3 Proliferation Curves

With the aim to study how SLG influences cell behavior with respect to standard substrates, I compared proliferation curves of two different cells lines on different substrates starting from 3 h after cell seeding up to seven days in culture; specifically on SLG and glass substrates, either coated or not with PDL. I used two cell lines in order to investigate whether the effect of SLG is cell line specific or not. I used N2a cells and CHO (Chinese Hamster Ovary) cells, an epithelial cell line. The reason behind choosing CHO as a second cell line is that several studies have been conducted on it in my group (105). Specifically, we have compared SLG and glass, either coated or not with PDL. Equal density of cells (255 cells/mm^2) was plated on substrates of interest (in triplicates) and cultured at 37^0C with 5% CO_2. Cells were fixed, with 4% paraformaldehyde (PFA) in phosphate-buffered saline (PBS) for 30 min at room temperature, at the following time points: 6h, day 1 (D1), D2, D3, D4, D5, D6, and D7, rinsed three times in PBS, and then mounted on glass slides with ProLong anti fade mounting media with with 4′,6-diamidino-2-phenylindole (DAPI) for nuclear staining (Thermo Fisher Scientific, Waltham, MA, USA). Fluorescence images were captured using a Nikon Inverted Microscope TiE equipped with a confocal microscope (Nikon Optical Co., Ltd., Japan) at excitation wavelengths λ= 405 nm at a magnification of 10x and 20x. Total number of cells was determined by counting cell nuclei following image analysis procedure described in the following section (3.5).

As expected, PDL always facilitated the adhesion properties of cells, and, more importantly, the proliferation rate was higher on PDL coated SLG substrates with respect to glass (Fig. 3.2 & Fig. 3.3).

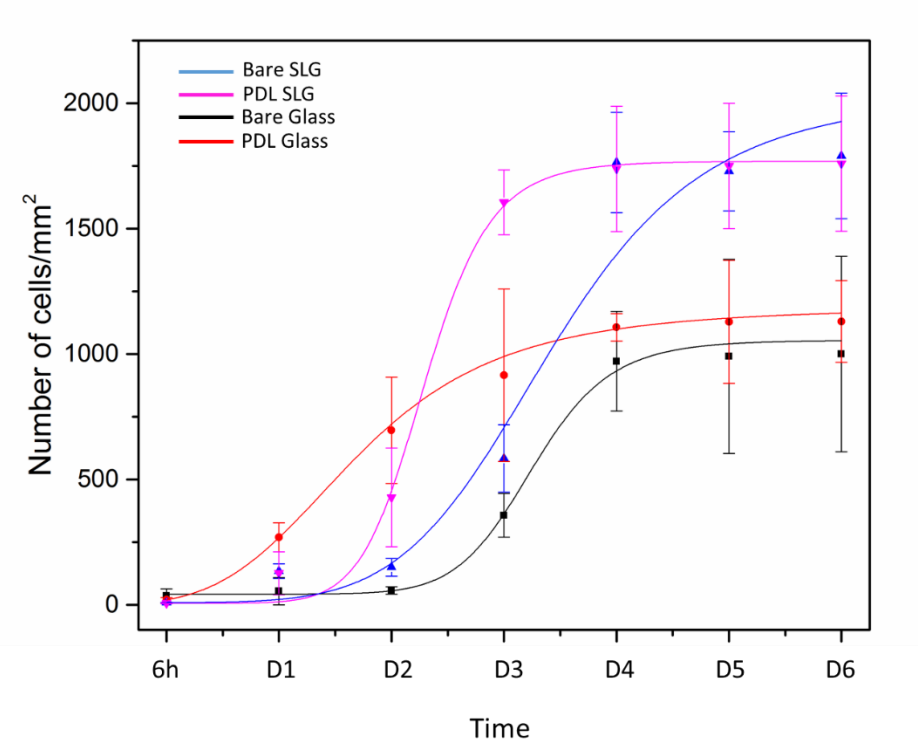

Figure 3.2 Proliferation curves of N2a cells on bare and coated SLG substrates.

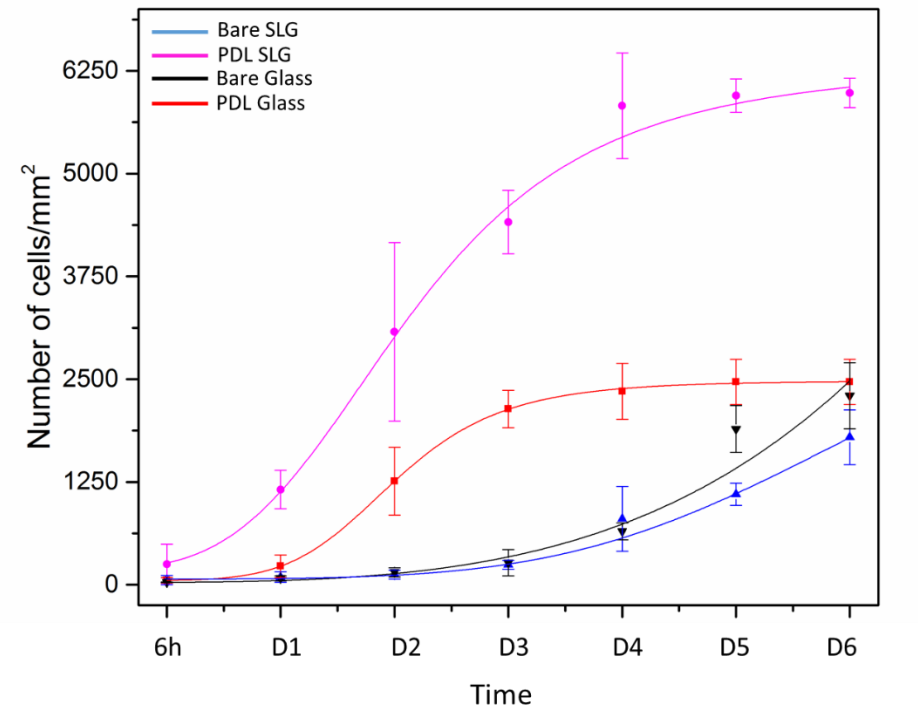

Figure 3.3 Proliferation curves of CHO cells on bare and coated SLG substrates.

3.4 N2a Differentiation

The effect of SLG on N2a differentiation has been studied by monitoring the shape, number and length of the processes (neurites) on SLG *versus* glass substrates, either coated or not with PDL, during 48 h incubation with and without 20 µM retinoic acid (RA) treatment.

Qualitative analysis was performed on the cells cultured in normal media (Fig. 3.4) and quantitative analysis on the cells with RA treatment (Fig. 3.5).

3.5 Immunofluorescence Staining and Image Analysis

Immunofluorescence staining was performed following the previously described procedure (110,111). In brief, the cultures on coverslips were fixed with 4% PFA in PBS for 30 min. After permeabilization with 0.1% Triton X-100 in PBS for 10 min four times, the cultures were incubated with PBS containing 5% goat serum and 0.1% Triton X-100 for 1 h. The permeabilized cultures were incubated with primary antibodies (1:100 anti-microtubule associated protein 2, MAP2, mouse IgG; 1:100; Sigma-Aldrich) in PBS containing 5% goat serum overnight at 4°C and were rinsed with PBS for 10 min four times. The cultures were then incubated with secondary antibody (1:200 Alexa Fluor 488-labeled anti-mouse IgG; Molecular Probes) in PBS containing 5% goat serum for 2 h at room temperature and rinsed four times. The coverslips were removed from 12-well plate and mounted on glass slides with ProLong anti fade mounting media with DAPI for nuclear staining (Thermo Fisher Scientific, Waltham, MA, USA). Fluorescence images were captured using a Nikon Inverted Microscope TiE equipped with a confocal microscope at excitation wavelengths λ= 405 nm and λ= 488 nm at a magnification of 10x and 20x.

Image analysis was performed using Nikon Imaging Software (NIS-Elements, Nikon Instruments, Japan) and ImageJ Software (NIH, Bethesda, Maryland, USA). Images were taken at least at three different cell locations, and the experiment was conducted in triplicate. To determine the total cell

density, we counted the number of cell nuclei using DAPI stained images which were transformed into black and white images and then converted into binary files based on which the total number of nuclei was determined. Objects in the binary images that were slightly overlapped were separated by Watershed separation using ImageJ software. To quantify the number of differentiated cells, we counted the number of somata of MAP2 positive neurons following the method previously described (111). Percentage of spreading cells, i.e. neuritogenesis, was defined as (spreading cells/total number of adherent) X 100 (Fig. 3.6).

3.6 Statistical Analysis

Data within the text are expressed as mean +/- standard error of the mean (SE). Statistical analyses were performed using OriginPro (OriginLab Corporation, Northampton, MA, USA) software assessing the statistical significance using student's t-test (Tukey test) and One-Way Repeated Measures ANOVA.

3.7. Confocal Imaging and Image Analysis

From sets of confocal images (Fig. 3.4) of immunolabeled N2a cells cultured in normal medium, the possible effects of the substrate properties on different cell behavior, for example associated with cell shape and neuronal like extensions, may be addressed. It is evident that the number of neuronal like extensions is higher on SLG and PDL-SLG as compared with glass. Taking a closer look at the cellular behavior on SLG and PDL-SLG and comparing the number of neuronal like extensions and their length qualitatively, it can be observed that this number is higher and the extensions are longer on PDL-SLG.

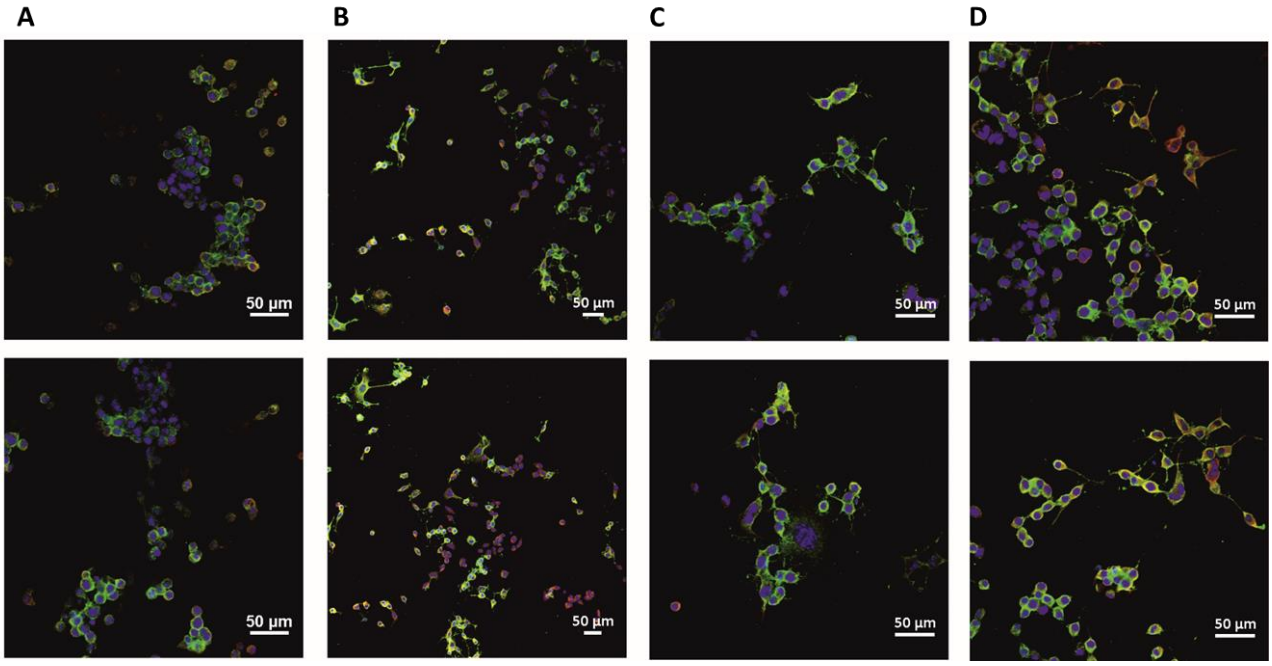

Figure 3.4 Two representative sequences of large-scope confocal images of N2a cells after 48 h cultured on control bare glass (A), PDL/glass (B), bare SLG (C) and PDL/SLG (D) (scale bar is 50 µm).

Similar sets of fluorescence images (Fig. 3.5) of N2a cells incubated with 20 µM retinoic acid (RA) treatment, allowed to determine the surface efficiency in cell adhesion by cell counting. In addition to cell counting, after proper staining, a parameter, called neuritogenesis, has thus been calculated, which is the ratio of number of cells with neuronal-like processes (neurites) to the total number of adhering cells (detailed explanation of the quantitative analysis is presented in the supporting information section at the end of this chapter). This result is presented in Fig. 3.6 (A).

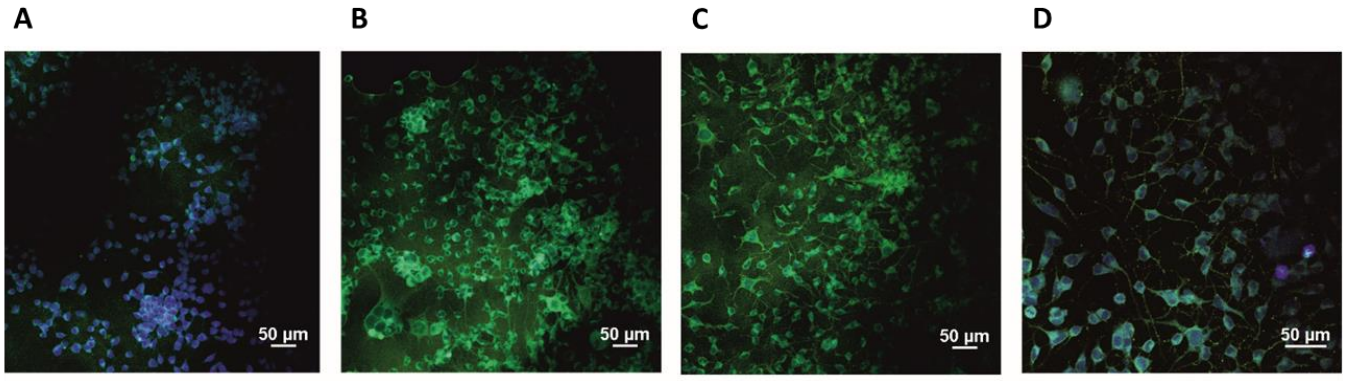

Figure 3.5 One representative sequence of large-scope confocal images of N2a cells after 48 h cultured on control bare glass (A), PDL/glass (B), bare SLG (C) and PDL/SLG (D) with retinoic acid (scale bar is 50 µm).

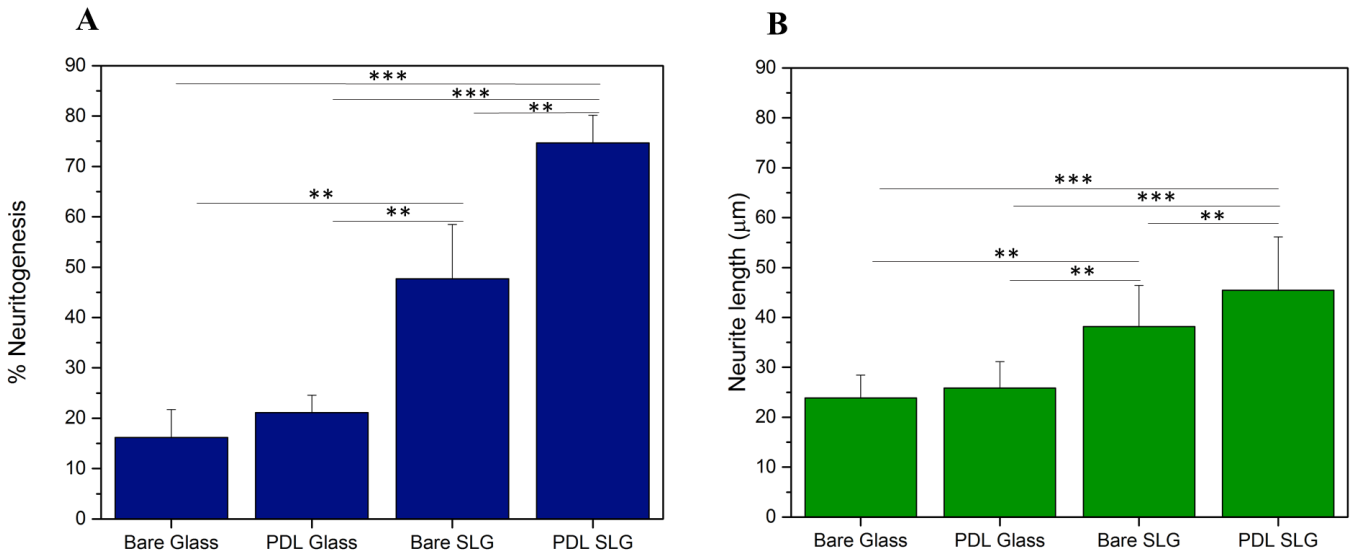

Figure 3.6 Functional parameters of adhering cells: (A) neuritogenesis, (B) mean normalized length of the existing neuritic-like processes. Pairs joined by lines show statistically significant difference (**: $p<0.01$; ***: $p<0.001$).

It appears from Fig. 3.6(A) that the cells seeded SLG substrates, whether bare or PDL coated, present the larger number of neurites; the highest neuritogenesis rate is obtained on PDL coated SLG, whereas this number is minimum on glass substrates. In particular, the differences are statistically significant for

the comparisons of bare glass to bare SLG ($p<0.01$), bare glass to PDL-SLG ($p<0.001$), PDL-glass to bare SLG ($p<0.01$), PDL-glass to PDL-SLG ($p<0.001$) and bare SLG to PDL-SLG ($p<0.01$).

In Fig. 3.6(B), the mean length of the identified neurites is plotted instead. In this case as well, a maximum appears for PDL-SLG substrates. Similarly, the differences are statistically significant for the comparisons of bare glass to bare SLG ($p<0.01$), bare glass to PDL SLG ($p<0.001$), PDL glass to bare SLG ($p<0.01$), PDL glass to PDL-SLG ($p<0.001$) and bare SLG to PDL SLG ($p<0.01$); thereby allowing us to confirm that SLG substrates and particularly the PDL coated ones drive the N2a cells towards a neuron-like behavior.

N2a cells were also cultured on the ablated SLG and SLG substrates in medium with RA treatment for 48 h. Confocal images of the immunolabeled substrates are displayed below (Fig. 3.7).

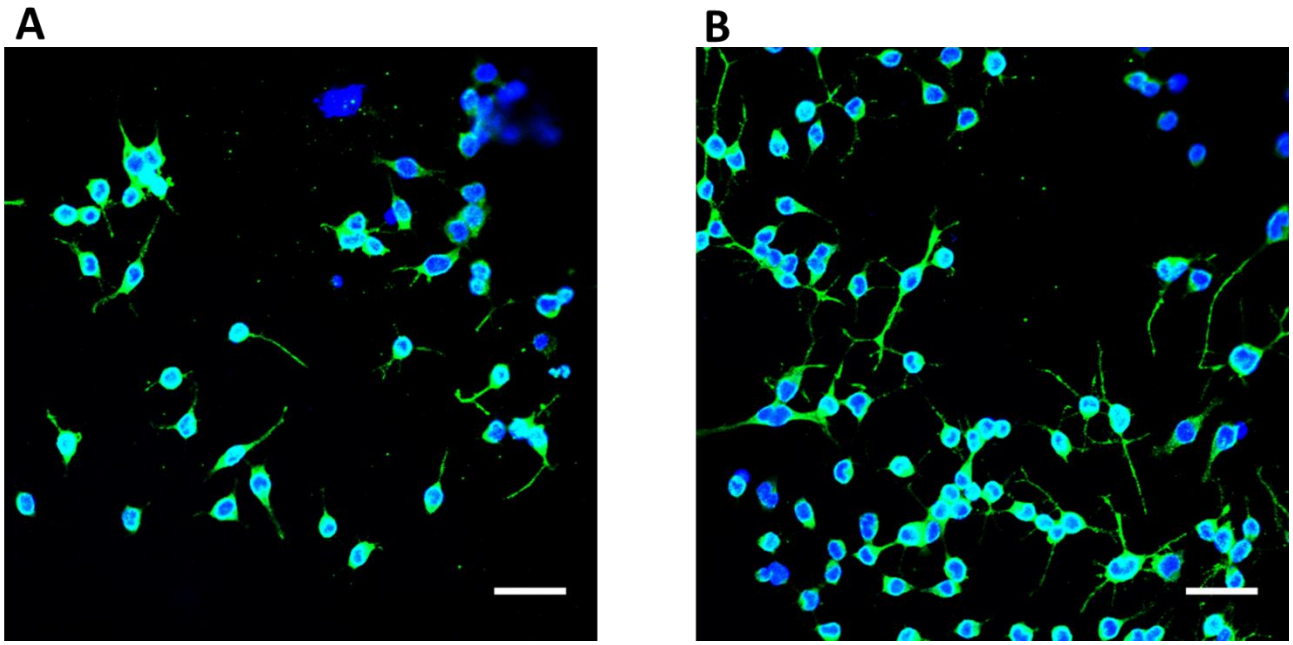

Figure 3.7 Confocal images of N2a cells after 48 h of incubation with RA on ablated SLG (A) and SLG substrates (B). Scale bar: 50 µm.

It appears that the number of N2a cells with neurites is higher on SLG substrates, where the length of neurites is longer than on the ablated SLG substrates; thereby confirming that SLG promotes N2a differentiation.

As mentioned in the beginning of this chapter, this experiment has been performed in order to determine whether the behavior of cells on ablated/SLG substrates is cell type dependent.

I have also studied the behavior of CHO on this kind of substrates, and I have observed a different behavior where the cells preferred the ablated region (rectangles of Fig. 3.8 represent the ablated regions of SLG substrates) instead of SLG region as was the case with neurons (31,112) and N2a cells; thus confirming that the behavior of cells on graphene is cell line specific.

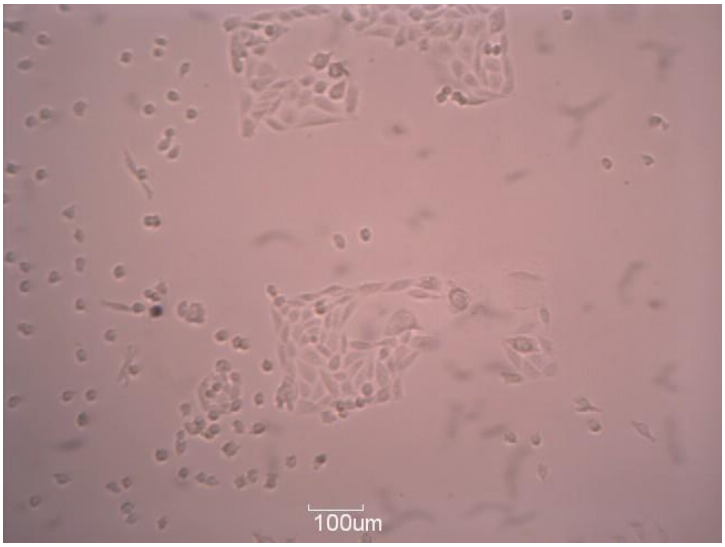

Figure 3.8 Optical image of CHO cells cultured on ablated/SLG substrate (48h after cell seeding).

3.8 Visualizing samples using pump-probe microscopy

Once again, I have employed the pump-probe microscopy technique for visualizing my substrates seeded with cells this time (Fig. 3.9). Imaging has been done on fixed samples (without immunolabeling) and immunolabeled samples.

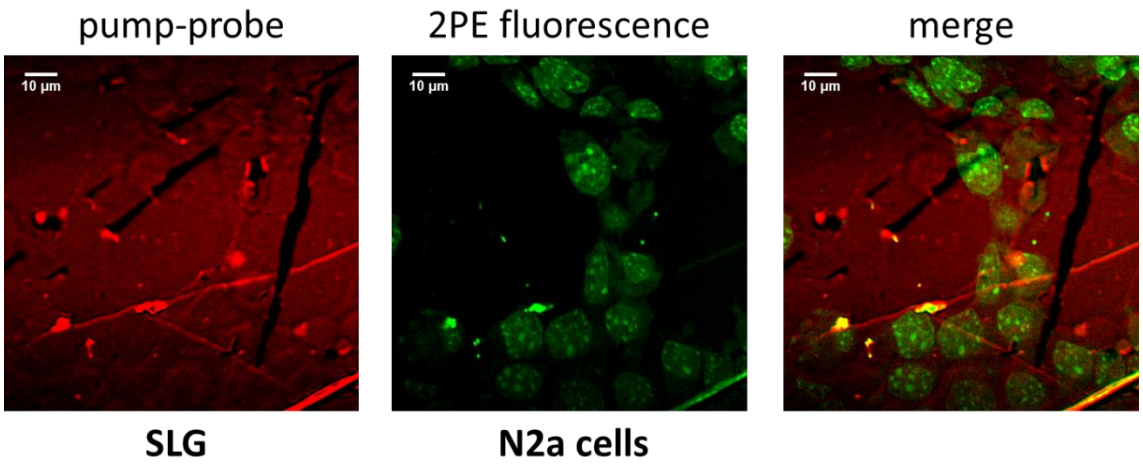

Figure 3.9 Pump-probe microscopy images of the N2a cells cultured on the SLG substrate.

For this kind of substrates, this technique is useful as:

- It allows to see both graphene and cells at the same time with a multimodal approach and two different types of signals: two photon fluorescence from cells collected in epifluorescence, pump-probe signal from graphene collected in transmission

- It is possible to see defects on the graphene layer (brightest spots are multilayer regions, while dark areas correspond to holes in the graphene) and see if the cells behave differently due to the graphene structure

- It gives the possibility of imaging cells without immunolabeling because they exhibit strong auto-fluorescence when exited in the near infrared. This can accelerate the experiments as it eliminates the need for staining. It is also less invasive as there are no external fluorescent dyes added. The disadvantage of auto-fluorescence is that it comes from all the cell body (except nucleus), so it is not possible to distinguish organelles inside the cytoplasm. If the selectivity inside the cell is required, then the staining should be done.

3.9 Conclusions

In this chapter, I have studied the effect of SLG substrates on the differentiation of N2a cells cultured in normal medium with RA treatment and without. N2a cells were cultured on bare glass, bare SLG and PDL/SLG substrates for 48 h. It has been observed that SLG (bare and PDL coated) induces neurite sprouting of N2a cells as compared with glass; this result has been more evident in the presence of RA in the medium. Moreover, the length of neurites was longer when the cells were cultured on SLG and PDL/SLG substrates in comparison with glass. Hence, in this work, I have demonstrated the stimulatory effect of SLG on neuronal differentiation of N2a cells; this result along with further studies to identify the type of neurons to which the cells differentiate, could confirm the potential of graphene for being used as active substrates for regenerative medicine allowing the enhancement of axon regeneration.

I have also studied the effect of ablated/SLG substrates on N2a and CHO cells, and I observed a different behavior where N2a cells preferred SLG region and underwent enhanced differentiation on it while CHO cells migrated towards the ablated regions. Thus, the obtained results confirmed that the behavior of cells on ablated/SLG substrates is cell type dependent. N2a cells, knowing that they differentiate into neurons and are a model for studying neurons, behaved like neurons (31,112) preferring SLG for proliferation and differentiation.

Supporting information

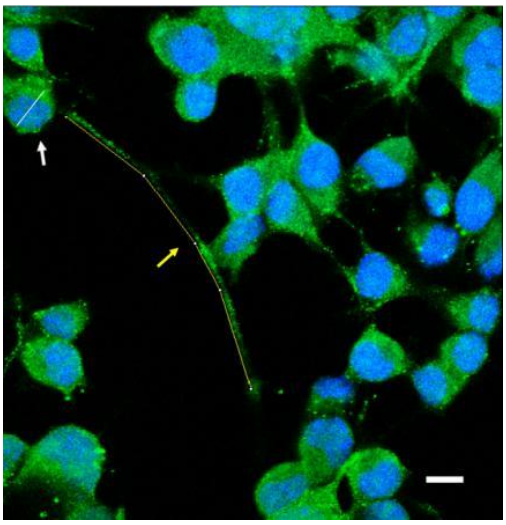

Figure S1 One representative high-resolution image of N2a cells (60X, 20 µm scale bar) used to identify and measure the neurites, for quantitative analysis of neuritogenesis and neurite length. Yellow arrow is pointing to one of the neurites; white arrow is pointing to soma.

The percentage of differentiated cells (neuritogenesis) was determined counting the number of cells with at least one neurite with a length equal to or longer than the cell body diameter. The neurite length was measured as illustrated in Fig. S1.

CHAPTER 4:

SLG Functionalized MEAs for Enhanced Detection of Neuronal Network Development

In this chapter, I have presented a study that I carried out in collaboration with Neuroscience and Brain Technologies department. Knowing that the exploitation of graphene for neuro-interfacing applications requires a complete, yet missing, understanding of neuron-graphene interaction, we have explored the interplay between the carbon based interface and neuronal networks during the complete developmental phase at whole network scale. To this purpose, we have, first, successfully transferred large grains single layer graphene (LG-SLG) via wet etching onto commercial planar 60 electrode devices; then, we have compared to control the neuronal growth on the functionalized devices, recording the spontaneous activity up to completion of network maturation, i.e., from 7 to 25 days-in-vitro. This chapter explains in detail the whole project starting from the introductory part, materials and methods employed, the results part and the discussion.

4.1 Micro-Electrode Arrays (MEAs)

Planar Micro-Electrode Arrays (MEAs) are a valuable tool for the long-term *in vitro* recording of cells or tissues electrical activity without causing any damage to the cells (113); since the first development, MEAs have been widely applied to monitor the behavior of electrogenic cells (e.g. cardiomyocytes (114) and neurons (115)) or tissues (hippocampal slices (116,117), retina (118,119)). The most common MEA application is, however, the recording of the spontaneous activity of primary neuronal networks. Neuronal networks are known to be spontaneously active and able to generate a rhythmic activity consisting of alternate almost synchronized patterns called ‘bursts’(115). MEAs recordings provide the possibility to monitor the electrophysiological activity of neurons from single spikes to whole network events, i.e. network bursts. Recordings of the spontaneous activity of the neuronal network have been used as an assay for network performance in applied settings (120,121).

Conventional MEAs consists of a discrete number of metal electrodes integrated on a substrate, usually glass or silica. Recently, in order to improve the MEA performances in terms of signal-to-noise ratio

(SNR), different strategies have been proposed, including the chemical functionalization of the electrodes (122) and their topographical modification increasing roughness or creating 3D features in order to improve the cell-to-electrode sealing. Examples of these approaches are the fabrication of electrodes with increased roughness (123), of porous electrodes (124), or of electrodes with 3D features to name only a few. Alternatively, the employment of new materials, especially carbon-based materials, has gained popularity (125,126).

4.2 SLG and MEAs

As mentioned earlier (chapter 1), graphene is one of the promising materials recognized for its high conductance, high mechanical strength and optical transparency as well as biocompatibility (3). Its intriguing properties have been exploited for several biomedical applications (14,40,105,127,128); it has been also involved in the fabrication of transistors to detect action potentials (14,129) and used as an electrode for the same purpose (130,131). Recently, graphene MEAs consisting of graphene electrodes have been fabricated and used in the successful recording of the neuronal activity of primary rat cortical neurons (20). Moreover, in other studies (37,51), it has been demonstrated that the viability of neuronal cells and average neurite length were significantly enhanced on graphene substrate compared to the conventional tissue culture substrate indicating that graphene could be a neuron favorable material.

SLG grown by CVD on Cu foil may be considered extremely favorable in the field of biosensor development due to its high crystallinity, scalability and convenient transfer onto any substrate, including flexible ones (132).

In a recent investigation by our group (105), we monitored the *in vitro* development of neuronal networks growing onto SLG and we compared the single neuron synaptogenesis on SLG and on control glass substrates during the first and second week after cell seeding by means of patch clamp

recording. Neurons grown on SLG resulted to be fully functional; the synaptogenesis was following, though, a slightly different trend. Intrigued by that result and aiming to explore better neuron-SLG interface, I have been involved in the investigation of the electrophysiological development of neuronal cultures on SLG at the whole network level, the study described in the current chapter. We have functionalized the surface of commercial 60 electrode MEAs by transferring SLG *via* wet etching, and we have recorded the network activity up to completion of network maturation, compared to that on standard not functionalized devices.

We have chosen to employ large grain SLG (LG-SLG) as it possesses a higher electrical conductivity (133) and therefore shall yield optimized performance when acting on MEAs.

4.2.1 LG-SLG

The graphene was synthesized using an Aixtron BM Pro cold-wall reactor on electropolished Cu foil (Alfa-Aesar 13182). To increase the average grain size of the continuous films, the nucleation of graphene was reduced using argon annealing and a sample enclosure, as it has been described previously (134). The growth was performed for 20 minutes at a temperature of 1070 °C and a pressure of 25 mbar, flowing methane, hydrogen, and argon at 3 sccm, 20 sccm and 1000 sccm, respectively.

4.2.2 LG-SLG transferring and characterization

LG-SLG was produced on Cu foils with size 2 cm x 2 cm. The size of the grains was about 200 mm x 200 mm as estimated from partial growths. This size was chosen in order to be comparable with a single electrode area and to maximize the coverage of each electrode with large area grains. Fig. 4.1 displays the typical morphology of graphene large grains.

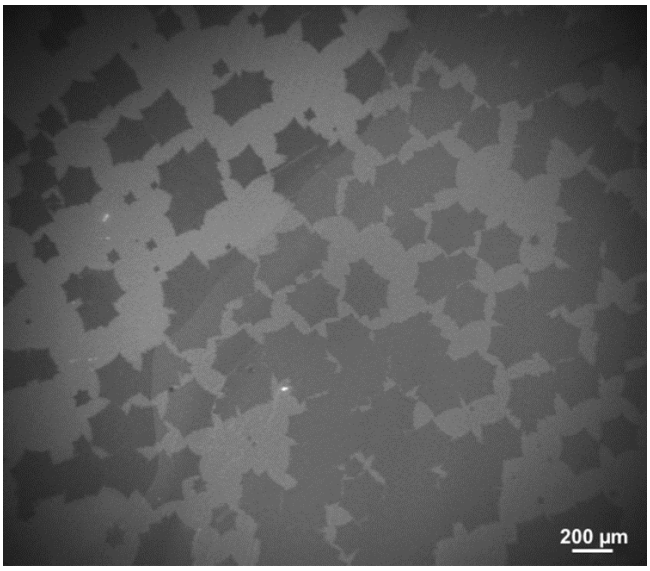

Figure 4.1 SEM micrograph of a partial growth of graphene on Cu foil. The average diagonal size of the single crystals is about 200 µm.

LG-SLG was transferred onto the surface of the 64-electrode MEA following a wet etching transfer procedure already used in a previous investigation (31) and reported in Chapter 2, section 2.1. The scheme of the wet etching procedure is shown in Fig. 4.2. Of note, the procedure was applied to the device already equipped with the external ring for culture medium confinement. For immunolabeling experiments, LG-SLG was transferred onto normal glass coverslips, following the same wet-etching protocol. All the chemicals were from Sigma Aldrich. To evaluate the quality of the large crystal SLG, Raman analysis was routinely carried out on the MEA at ambient conditions using an in ViaRenishaw (New Mills, UK) µRaman spectrometer equipped with a microscope. The Raman spectra had two prominent features at ~1582 cm^{-1} ("G" band) due to the sp^2 vibration and a stronger single Lorentzian sharp peak centered around ~2700 cm^{-1} ("2D" band) of the graphene on the MEA. No disorder-related D peak at 1350 cm^{-1} was observed, indicating an extremely low density of lattice defects.

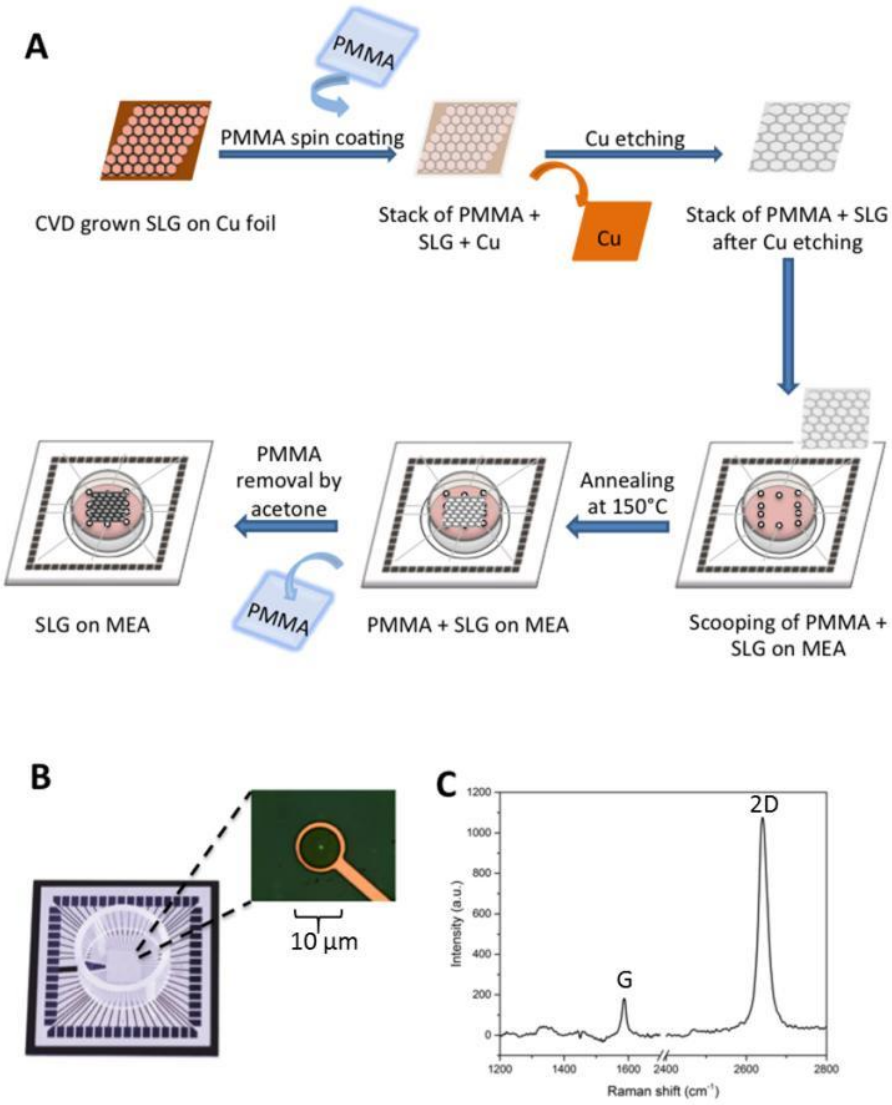

Figure 4.2 A schematic of the wet etching transfer of SLG onto a commercial MEAs device B: Optical image of the functionalized MEA; the coated electrode source of the spectrum is reported in the zoomed image on the left side, where the laser spot for Raman analysis is visible in the middle of the electrode. C: Raman characterization of the transferred SLG showing the two characteristic G and 2D band.

4.2.3 Primary neuronal cultures

Dissociated neuronal cultures were prepared from hippocampi of 18-day old embryonic rats (pregnant Sprague-Dawley female rats were obtained from Charles River Laboratories). Briefly, the hippocampi of 4–5 embryos were dissected out from the brain and dissociated first by enzymatic digestion in

trypsin solution 0.125% (25–30 min at 37 °C) and subsequently by mechanical dissociation with a fire-polished pipette. The resulting tissue was resuspended in Neurobasal medium supplemented with 2% B27, 1% Glutamax-1, 1% Pen-Strep solution and 10% Fetal Bovine Serum (Invitrogen, Garlsbad, CA), at the final concentration of 75,000 cells/µl. We placed a 50-µl drop onto the MEA recording area (i.e., 25mm^2 is the area covered by the plated drop) previously coated with PDL and laminin to promote cell adhesion (final density around 1900 cells/mm^2) and maintained with 1 ml of nutrient medium (i.e., serum-free Neurobasal medium supplemented with B27 and Glutamax-1). They were then placed in a humidified incubator having an atmosphere of 5% CO_2, 95% air at 37 °C. Half of the medium was changed weekly. Neuron cultures were inspected with an optical microscope before each recording and optical micrographs at 20x were taken.

4.2.4 Immunolabeling, confocal microscopy and image analysis

4.2.4.1 Immunofluorescence staining and image analysis

Immunofluorescence staining was performed as previously described (110,111). Briefly, the cultures on coverslips were fixed with 4% PFA in PBS for 30 min. After permeabilization with 0.1% Triton X-100 in PBS for 10 min four times, the cultures were incubated with PBS containing 5% goat serum and 0.1% Triton X-100 for 1 h. The permeabilized cultures were incubated with primary antibodies (anti-microtubule associated protein 2 [MAP2] mouse IgG; 1:100; Sigma-Aldrich) in PBS containing 5% goat serum overnight at 4°C and were rinsed with PBS for 10 min four times. The cultures were then incubated with secondary antibody (Alexa Fluor 488-labeled anti-mouse IgG; Molecular Probes) in PBS containing 5% goat serum for 2 h at room temperature and rinsed four times. The coverslips were removed from 12-well plate and mounted on glass slides with ProLong anti fade mounting media with DAPI for nuclear staining (Thermo Fisher Scientific, Waltham, MA, USA). Fluorescence images were

captured using a Nikon Inverted Microscope TiE equipped with a confocal microscope (Nikon Optical Co., Ltd., Japan) at excitation wavelengths λ=405 nm and λ=488 nm at a magnification of 10× and 20×.

Image analysis was performed using Nikon Imaging Software (NISElements, Nikon Instruments, Japan) and ImageJ Software (NIH, Bethesda, Maryland, USA). To determine the total cell density, we counted the number of cell nuclei using DAPI stained images which were transformed into black and white images and then converted into binary files based on which the total number of nuclei was determined. Objects in the binary images that were slightly overlapped were separated by Watershed separation using ImageJ software. To quantify the number of neurons, we counted the number of somata of MAP2 positive neurons following the method previously described (111).

4.2.4.2 Confocal microscopy on immunolabeled samples and image analysis

The behavior of hippocampal neurons cultured on the LG-SLG transferred coverslips versus bare coverslips was investigated by optical inspection confocal microscopy of immunolabeled samples at three different developmental phases: 7 DIV, 13 DIV, and 25 DIV. Fig. 4.3 summarizes the findings. Based on our previous knowledge, the presence of the protein adhesion layer was necessary for neuronal survival (31,56). The particular suitability of PDL/laminin coating for culturing neurons on graphene was recently reported (37). No significant changes in morphology were observed in the neuronal networks cultured on LG-SLG coverslips versus control coverslips. Neurons spread homogeneously to cover the whole surface of the MEA forming clumps mainly visible on SLG-MEA at DIV25 (Fig. 4.4) and coverslips (Fig. 4.3 (A)). In some cases, they form aggregates (clumps), but both types of cultures demonstrated morphology of healthy cells. By means of DAPI fluorescence, which indicates the presence of cell nuclei, we were able to observe that the total cell density increased during the development with no significant difference between both the LG-SLG and control cultures (Fig. 4.3 (B)). The density of neuronal cells was computed by the neural-specific marker MAP2. MAP2

quantification indicated that also the number of neurons was, in general, the same on LG-SLG with respect to control cultures, but a statistically significant difference was found at 13 DIV (Fig. 4.3 (C)).

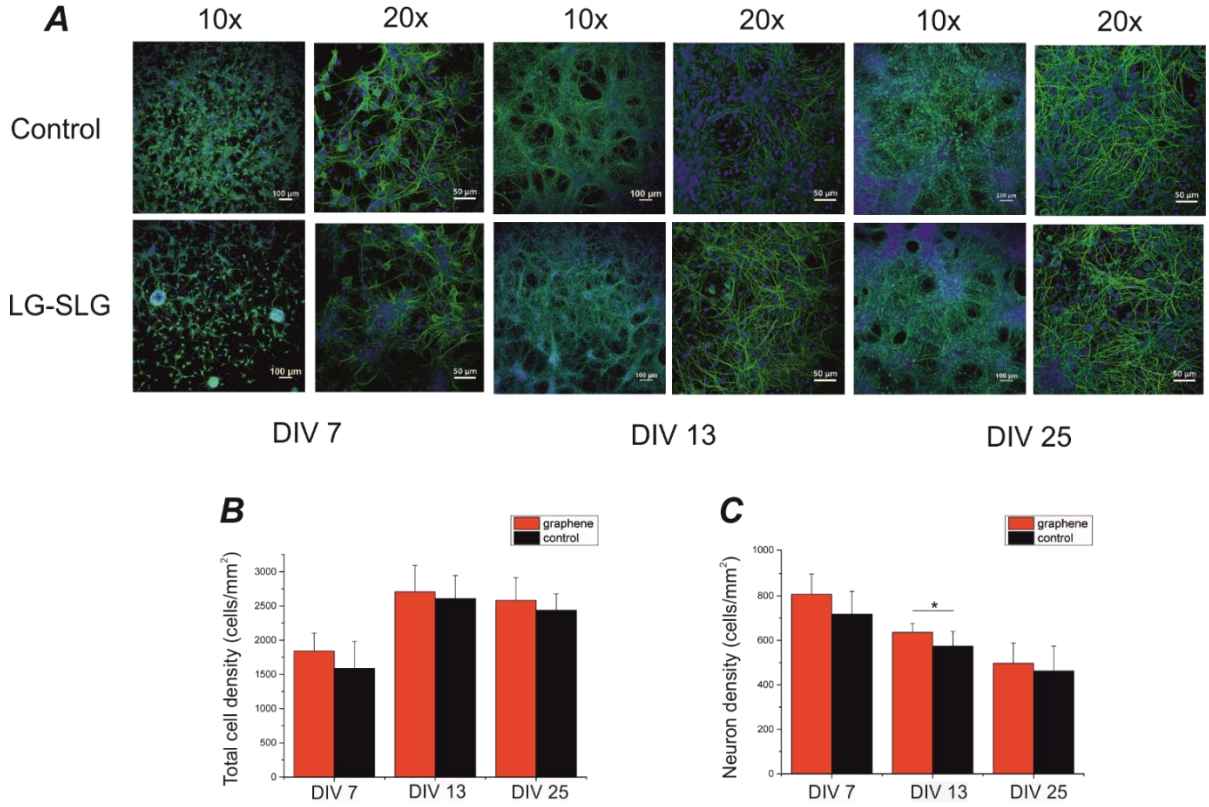

Figure 4.3 Morphological changes in hippocampal networks cultured on graphene-transferred substrate during development. A. Immunofluorescence micrographs of MAP2 of a representative culture on normal coverslips (top) and on LG-SLG coated coverslips (bottom), at three different developmental phases: 7 DIV, 13 DIV and 25 DIV, respectively from left to right at 2 different magnification factors (i.e. 10× and 20×, scale bars 100 μm and 50 μm, respectively). B. Bar graph of the total cell density on the two groups. No significant difference was found. C. Bar graph of the neuronal density at different DIVs on LG-SLG MEAs (red) and on control (black). Significant difference was found only at 13 DIV.

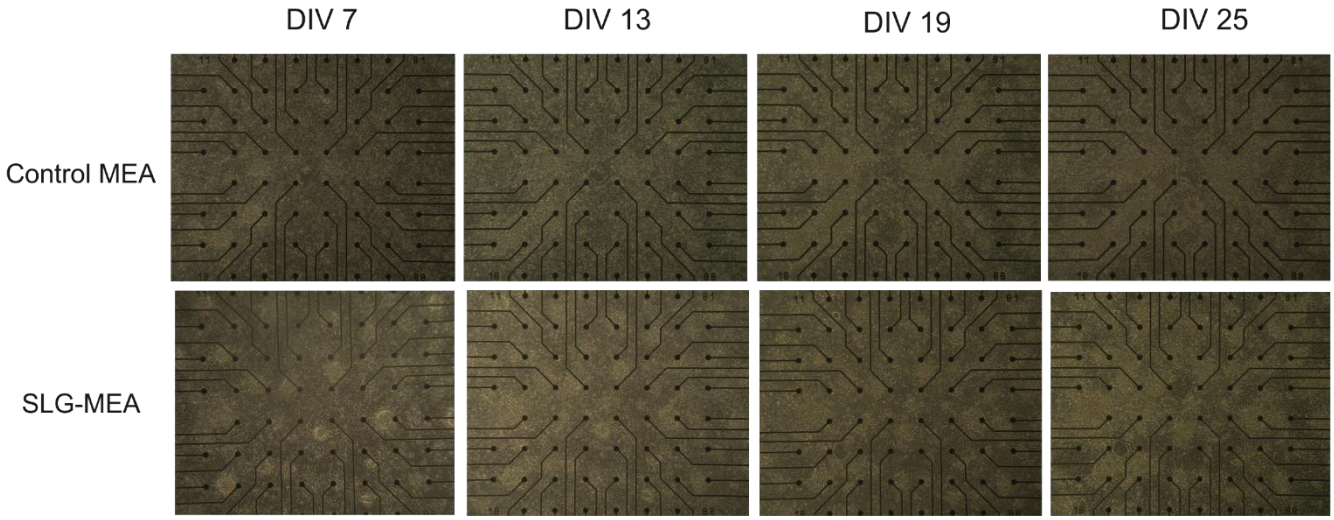

Figure 4.4 Optical micrograph of neuronal networks grown on a control MEA (top) and on a SLG-MEA (bottom) at different developmental ages. No morphological differences emerge from the comparison.

4.2.5 MEA recordings

The experimental set-up, based on the MEA 60 system, is composed of a microelectrode array, a mounting support with 60 integrated channels, a pre-and a filter amplifier (gain 1200x), a personal computer equipped with a PCI data acquisition board for real time signal monitoring and recording, and anti-vibration table and a Faraday cage. Network activity was recorded using commercial software (MCRack, Multichannel Systems, MCS, Reutlingen, Germany). To reduce thermal stress of the neurons during each experiment, MEAs were kept at 37°C by means of a controlled thermostat (MCS) and covered by a PDMS cap to avoid evaporation and to prevent changes in osmolarity (135). Additionally, we have settled a custom incubation chamber to maintain a controlled atmosphere (i.e., a gas flow of 5% CO_2 and 95% O_2+N_2) during the entire recording time, as reported in previous papers (136). The spontaneous activity was monitored and recorded for 90 min, after a period of rest outside the incubator into the experimental set-up of 30 min, to let the culture adapt to the new environment and reach a stable level of activity (137).

4.2.6 Experimental database

The purpose was to monitor and compare the *in vitro* development of graphene-coated MEAs and control MEAs at seven different developmental stages: 7, 10, 13, 16, 19, 22, 25 DIVs. A total of 11 graphene cultures from 4 different preparations and 21 control cultures from 6 different preparations were initially plated. We then discarded the cultures that died along the development (i.e., 6 for the graphene and 16 for the control). Overall, we were able to collect data for the entire developmental profile from 5 cultures on graphene-coated MEAs and 5 control cultures. Every experimental session lasted 2 h, for a total of 14 h of recording for each network and 140 h of recording for the entire database. Data analysis and statistics Data analysis was performed off-line by using a custom software package developed in MATLAB (The Mathworks, Natick, MA, USA) named SPYCODE (138), which collects a series of tools for processing multi-channel neural recordings. The different steps of the analysis are briefly reported in the following.

4.2.7 Spike detection and firing analysis

In order to discriminate spike events, we used a custom spike detection algorithm (139). Briefly, the method used three parameters: (1) a differential threshold (DT) set independently for each channel and computed as 8-fold the standard deviation (SD) of the noise of the signal; (2) a peak lifetime period (PLP) set to 2 ms; (3) a refractory period set to 1 ms. The algorithm scans the raw data to discriminate the relative minimum or maximum points. Once a relative minimum point is found, the nearest maximum point is searched within the following PLP window (or vice versa). If the difference between the two points is larger than DT, a spike is identified and its timestamp saved. Then, to characterize the activity level of the analyzed networks, we computed the mean firing rate (MFR), which is defined as the mean number of spikes per second, computed over the total recording time (i.e., 90 min). We considered active electrodes as those presenting a firing rate higher than 0.01 spikes per second. The

low threshold guarantees to exclude only those electrodes that are not covered by cells or with very few spikes, keeping all the others.

4.2.8 Burst detection

Neuronal networks plated on MEA show both random spiking activity and, in large majority, bursting behavior (140,141). Bursts consist of packages of spikes distributed over a range of a few milliseconds, which generally last from hundreds of milliseconds up to seconds, and are separated by long quiescent periods. Spontaneous bursting activity was detected using a custom burst detection method, whose input parameters were directly estimated from the inter-spike interval distribution of each channel. The method used the logarithmic Inter Spike Interval Histogram (logISI) to extract the parameters needed for the analysis of each recording channel (142). In particular, the threshold used for detecting bursts was found as the minimum of two principal peaks in the logISI. Details can be found in a paper from our group (143). Once spike and burst detection procedures were performed, we extracted several parameters describing the electrophysiological patterns, such as mean firing rate (MFR) [spikes/s], mean bursting rate (MBR) [bursts/min], burst duration (BD) [ms] and the Inverse Burst Ratio (IBR), which represents the percentage of random spikes, i.e., spikes outside the bursts.

4.2.9 Cross correlation analysis

We computed the cross correlation analysis between each pair of spike trains recorded from active channels (i.e. with MFR > 0.01 spike/s). The Cross Correlation function represents the probability of observing a spike in one channel i at time ($t+\tau$, τ=3 ms) given that there is a spike in a second channel i+1 at time t. In order to quantify the strength of correlation between each couple of electrodes, we evaluated the Correlation peak (C peak). We select only the first 100 C peak values to identify only the most significant correlations at each developmental time steps: 13, 16, 19, 22, 25 DIV. We decided to exclude the early developmental stages 7, 10 DIV given the low level of activity. Finally, we analyzed

the latency from the peak (L peak) and we considered the corresponding peak latency values of the pre-selected 100 strongest C peak values (144).

4.2.10 Statistics

Data within the text are expressed as mean±standard error of the mean (SE), if not differently specified. Statistical tests were employed to assess the significant difference among different experimental conditions. We assessed the normal distribution of data using Kolmogorov- Smirnov normality test. According to the distribution of data, we performed either parametric (e.g. two-sample t-test) or non-parametric test (e.g. Mann-Whitney) between the control group (i.e. networks cultured on conventional MEAs) and the graphene group (i.e. networks cultured over LG-SLG treated MEAs). Statistical analysis was carried out by using OriginPro (OriginLab Corporation, Northampton, MA, USA).

4.2.11 Analysis of neuronal network activity

The recording of the spontaneous activity of the network was monitored during development (section 4.2.5). Raster plots of two representative networks are displayed in Fig. 4.5, control MEAs and LG-SLG MEA side to side at different DIVs. Each 10-s trace contains the spike events recorded by 60 electrodes at four different developmental phases: 7 DIV, 13 DIV, 19 DIV, 25 DIV, respectively from top to bottom. Each black dot represents a detected spike. Panel A shows the activity during development of the control network: at 7 DIV only a few random spikes are detected in the whole active area; the number increases during the second week, and at 19 DIV trains of spikes organized in network bursts are clearly visible. At 25 DIV, almost all the electrodes exhibit a high level of activity, which becomes more synchronized with network-wide brief burst (50–100 ms) separated by a period of nearly complete quiescence or sparse, asynchronous action potential. The LG-SLG MEA (Fig. 4.5 (B)) shows a higher level of activity, involving also more channels, as compared to the control cultures at every recording point. Specifically, at 7 DIV, we can observe that the majority of electrodes present a

good level of firing, while at 13 DIV network bursts are clearly visible. Network bursts appear more packed with spiking activity within the bursts more synchronized from 19 DIV on. This pattern is maintained all along the developmental window under investigation.

We then analyzed typical networks parameters for all monitored time frames (sections 4.2.7 and 4.2.8). Fig. 4.6 compares the firing and the bursting parameters of control (n=5 cultures) and LG-SLG MEA networks (n=5 cultures) during their development. As shown in Fig. 4.6, the LG-SLG MEA networks show higher values of firing/bursting rate at the very beginning of their development. MFR and MBR show a similar profile, with diverging values starting from 13 DIV (Fig. 4.6 (A–B)). In particular, for the firing rate, we found a significant difference between the control and LG-SLG MEA networks at 13 and 16 DIV, while for the bursting rate, statistical significance was found at 13, 19 and 22 and 25 DIV. Burst Duration did not show any significant difference between the two experimental conditions for every time points (Fig. 4.6 (C)). Contrary, the percentage of random spikes was higher (i.e. IBR) in the control experiments starting from 17 DIV, indicating a more asynchronous for control experiments (Fig. 4.6 (D)).

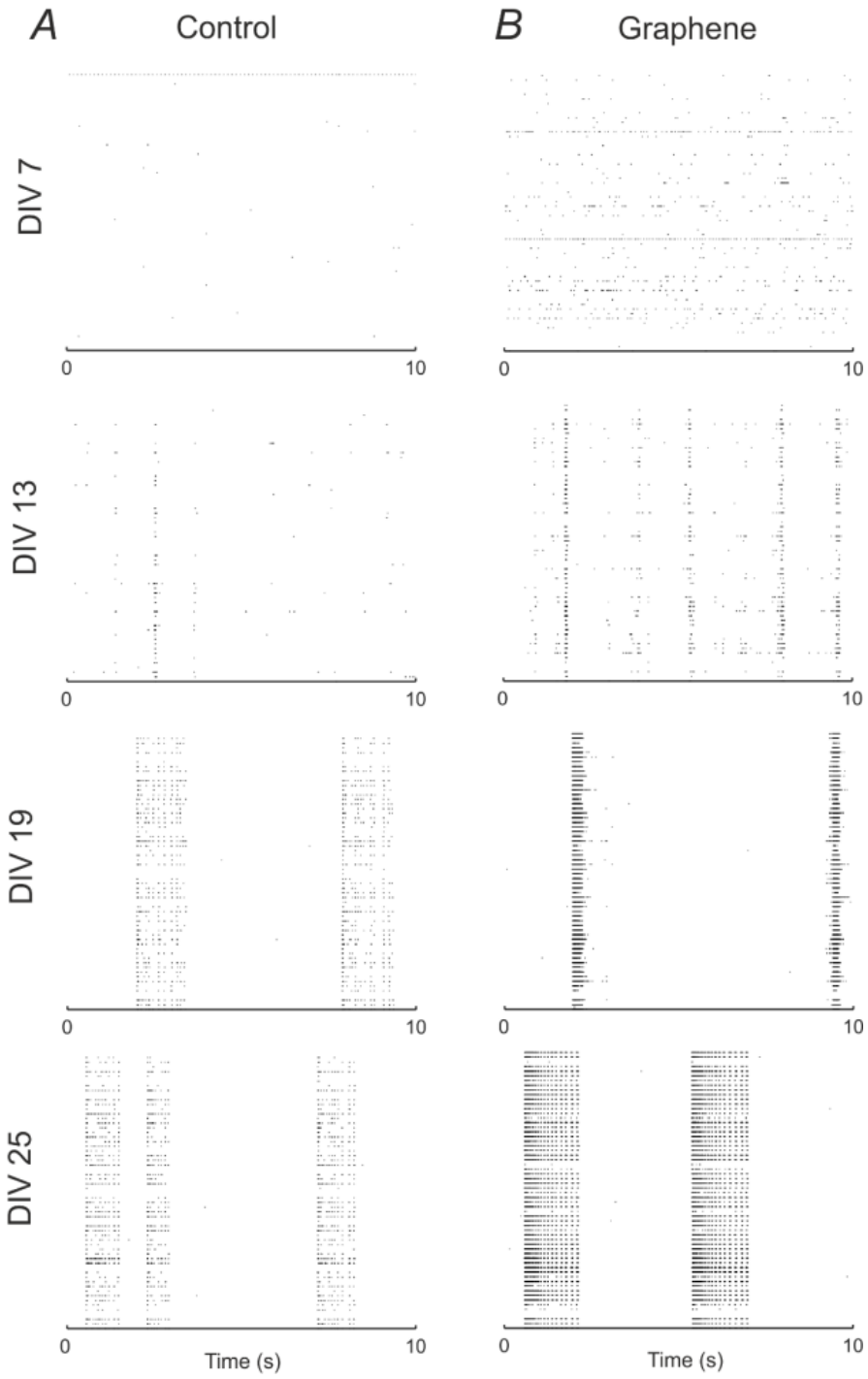

Figure 4.5 Developmental changes of hippocampal network activity of one representative graphene-transferred MEA and one control MEA. A. 10-s raster plots of spontaneous activity of a representative network cultured on conventional MEA, recorded by 60 electrodes at four different developmental phases: 7 DIV, 13 DIV, 19 DIV and 25 DIV, respectively from top to bottom. Each black dot represents a detected spike. B. 10-s raster plots of spontaneous activity recorded by 60 electrodes covered by single-layer graphene at four different developmental phases: 7 DIV, 13 DIV, 19 DIV, 25 DIV, respectively from top to bottom.

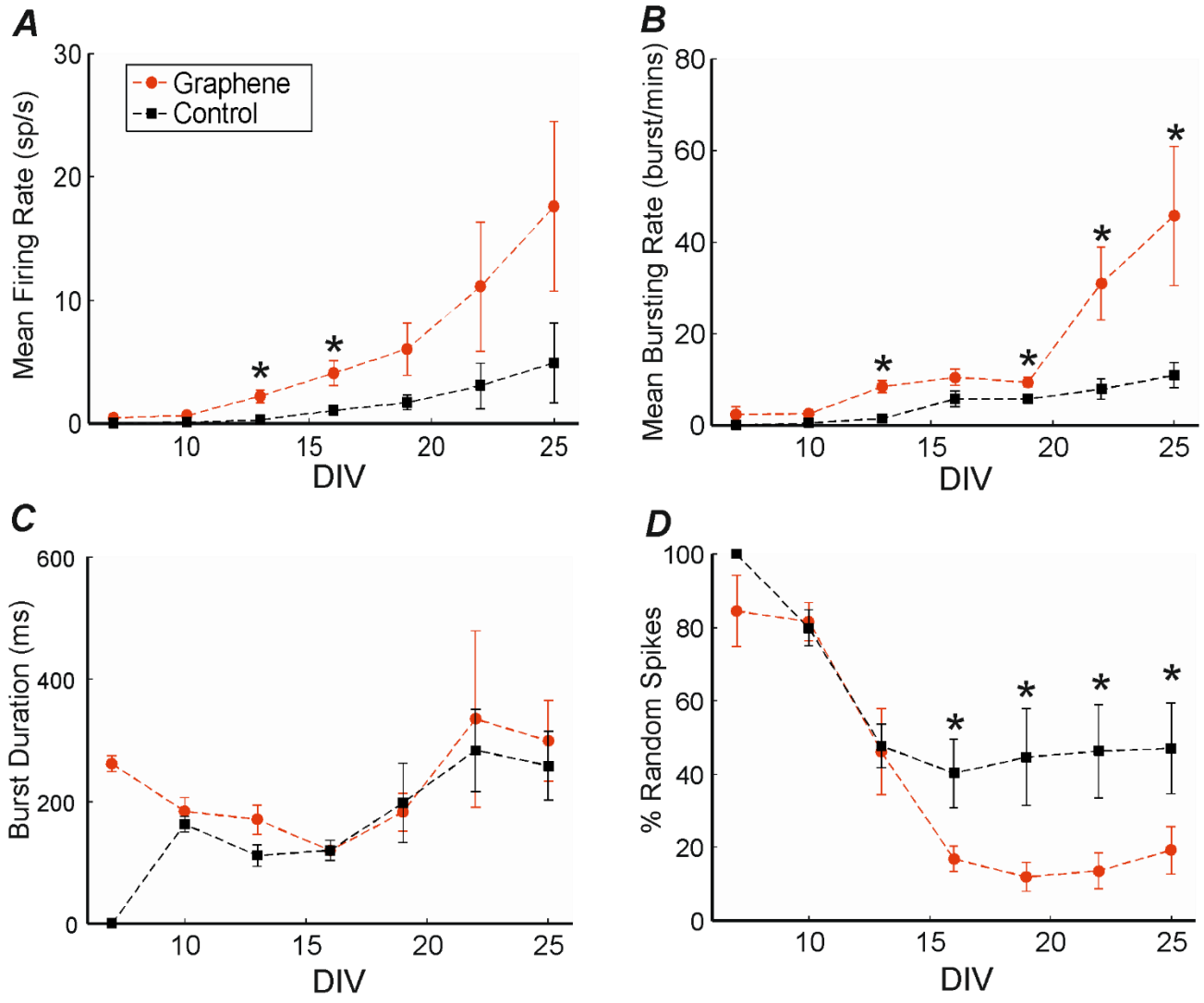

Figure 4.6 Developmental profiles of hippocampal network cultured on graphene-transferred MEA (red) and conventional MEA (black). A. Mean firing rate (spikes/s) of 5 cultures on graphene-transferred MEA and 5 cultures on conventional MEA. The parameter was significantly different between two groups at 13 and 16 DIVs. B. Mean bursting rate (burst/min): the parameter was significantly different between two groups at 13, 19, 22 and 25 DIVs. C. Burst duration (ms): no statistical difference was found between the two groups. D. Percentage of spikes outside burst (IBR): the parameter was significantly different between two groups from 16 to 25 DIVs. All data are presented as mean±SEM. Statistical analysis has been performed by using the two sample t-test (*$p < 0.05$).

In order to assess changes in the synchronicity between control and LG-SLG cultures, we then investigated whether and how the correlation level changes during the development. For this reason, we consider Cpeak and Lpeak values computed from the cross-correlograms of each pair of active electrodes. In Fig. 4.7 (A), we compare the Cpeak values at five different time points: 13, 16, 19, 22, 25 DIVs. Control experiments present lower values of Cpeak with respect to the LG-SLG MEA cultures. This indicates that the activity of LG-SLG MEA cultures is more correlated, as previously quantified by the IBR parameter (Fig. 4.6 (D)). Fig. 4.7 (B)), instead, shows boxplot of the Lpeak values. Longer latencies for the control cultures are observed, thus suggesting a higher delay in the activity propagation with respect to the LG-SLG MEA cultures.

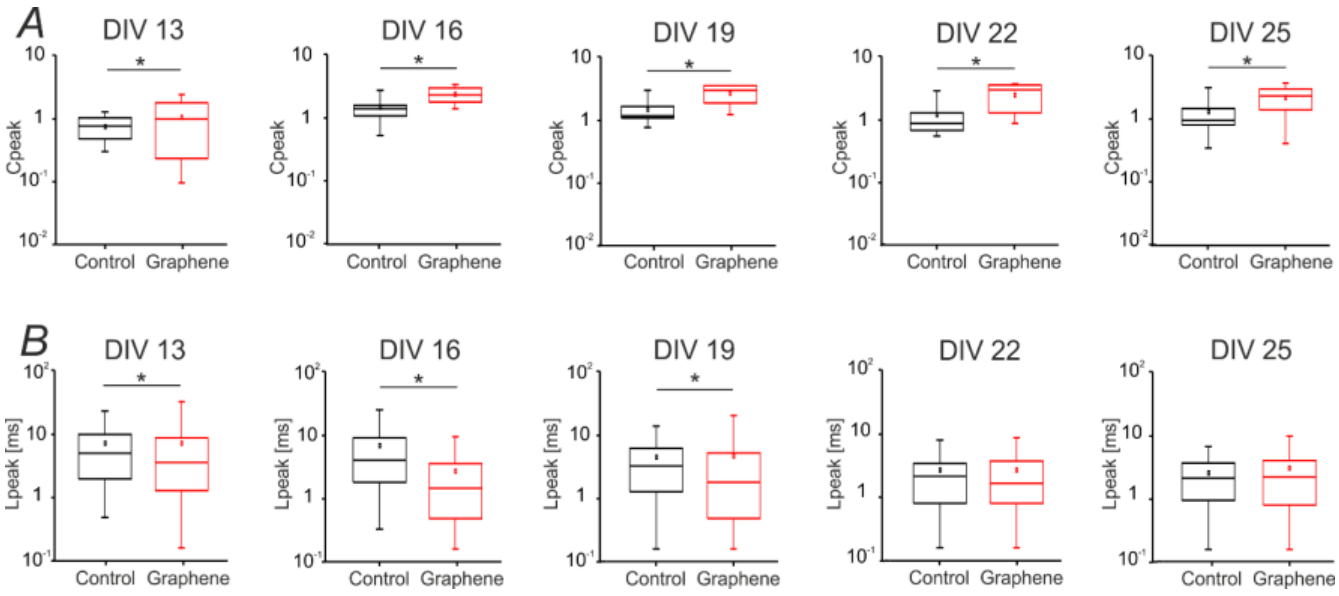

Figure 4.7 Cross Correlation Analysis. A) Box plots of the 100 strongest C peak values at each developmental time steps: 13, 16, 19, 22, 25 DIV for the control group (black box) and for the graphene (red box). We excluded the early developmental stage 7, 10 DIV since the level of activity was low. B) Box plots of the corresponding peak latency values (L peak) of the pre-selected 100 strongest C peak values. We considered only the peak latency values smaller than 50 ms. For each box plot (A–B), the small square indicates the mean, the central line illustrates the median and the box limits indicate the 25th and 75th percentiles. Whiskers represent the 5th and the 95th percentiles. Statistical Analysis was carried out using Mann-Whitney comparison test, *$p < 0.05$.

4.2.12 Discussion

In this chapter, I have presented the study of the electrophysiological development of neuronal networks on MEAs functionalized with large grain single layer graphene (LG-SLG-MEA) recording the network activity up to the completion of their maturation. This project covers both the investigation of the morphological properties of the neuronal network (on conventional and functionalized MEA) and the network development and functionality. This study can then shed light on the role that LG-SLG-MEA plays in detecting earlier neuronal network activity with respect to the conventional MEA. Graphene-based substrates have been recently employed as the interface for electrogenic cell (56,145). In particular, graphene electrodes and graphene-based MEAs consisting of graphene electrodes have been fabricated and successfully used for the recording of the neural activity of primary cultured rat cortical neurons (20,146). However, no study presenting a detailed, long-term neuronal network development on MEA functionalized with graphene has been conducted so far. The first part of the study started with the SLG transfer on MEA following the wet etching technique previously described (31,105). The following step was to ensure the successful defect free transfer of graphene using Raman spectroscopy before proceeding further with the experiments.

Immunolabeling results have demonstrated no significant changes in morphology of the neuronal network cultured on LG-SLG coverslips versus control coverslips (glass). Both cultures demonstrated morphology of healthy cells indicating that the presence of LG-SLG does not trigger any adverse reaction in the neuronal networks. The quantification of the cell density showed that the density increased with the increase in the developmental phases with no significant difference between both the LG-SLG and control cultures indicating an identical survival rate compared to standard conditions. As for the neuronal density determined by the neuronal specific MAP2 immunostaining, it was observed that the number of neurons was generally higher on LG-SLG with respect to control cultures (but the statistical significance was only found at DIV 13), indicating a higher survival rate or a higher

propensity of cells to adhere to graphene, as we already reported (31,105). Considering that the number of neurons vs. the number of total cells (Fig. 4.3(B) and (C)) was decreasing, it can be hypothesized that other types of cells, most likely glial cells, were increasing. This has a positive impact on neuronal cell development since it is well known and reported in the literature (147) that glia is necessary for the functional and healthy development of neuronal networks *in vitro*.

Concerning the neuronal growth on MEAs, the first positive observation was the higher survival rate of the neuronal cultures on SLGMEAs with respect to control. We were able to collect data during the entire development in 50% for graphene and 25% for control over the total initially plated cultures. This means that neurons on SLG-MEAs have a double chance of long-term survive with respect to the control ones. This result is very promising for the future development of graphene-based electronics since it is a demonstration of the robustness and biocompatibility of such interfaces. The investigation of the electrophysiological development of neuronal networks on SLG between the first and fourth week is the most novel part of this investigation. On the functionalized SLG-MEAs a higher number of active electrodes could be detected, as qualitatively visible in the raster plots in Fig. 4.5. The already mentioned higher number of neurons present onto SLG MEAs correlates well to this finding; additionally, a better coupling between neurons and electrode could be a factor influencing the enhanced detection from such a high number of electrodes. The electrophysiological activity of the control MEA during the development was in line with previous works (148–151). At 7 DIV, only a few random spikes and almost no burst were observed in the whole active area. At the early developmental stage, neuronal cultures usually showed low density synaptic density and less neuronal connectivity with respect to the mature stage (i.e., DIV higher than 14). After a week *in vitro*, at 13 DIV, networks exhibited an increase in the firing rate and in the bursting rate. The parameters computed through the Cross Correlation analysis (i.e. Cpeak and Lpeak) indicated a good level of synchronization, although it did not involve all the active electrodes. Starting from 19 DIV, the firing rate and the bursting rate

increased and showed a further increase until 25 DIV. The activity became more synchronized with frequent discharges organized in networks bursts. The percentage of spikes outside the burst (IBR) reached a minimum of 40% and it remained stable during later developmental stages (i.e., until 25 DIV). In a recent study (150), it was found that GABAergic and glutamatergic terminals increased gradually and simultaneously with the bursting rate, reaching a steady state between 3–4 weeks *in vitro*.

As regards LG-SLG-MEA, they showed a developmental profile which is in line with that of neuronal networks cultured over conventional MEAs, but, in general, with higher absolute values of the computed electrophysiological parameters. Specifically, the graphene treated networks exhibited higher values of firing and bursting rate at the very beginning of their development (i.e., 7 DIV). Bursting activity was clearly visible starting from 13 DIV, and from 19 DIV the LG-SLG MEA displayed short bursts with a very high bursting rate. The IBR reached a minimum of 18% and remained stable all along the developmental window under investigation. The analysis of the cross correlation showed higher values of Cpeak with respect to the control MEA starting from 13 DIV, indicating a stronger correlation of the activity. Longer latencies for the control MEA were observed, thus suggesting a higher delay in the activity propagation with respect to the LG-SLG MEA cultures. At the later developmental stages (i.e., from 21 DIV), the strength of the activity correlation remained higher for the LG-SLGMEA, possibly due to the higher number of bursting events in the graphene MEAs. Contrarily, the latency became similar between the control and the LG-SLG MEA cultures, indicating that the level of synchronization increased with time also for the control MEA, as confirmed by previous results (152). Hence, earlier and stronger synchronized neuronal network development was observed on LG-SLG-MEA as compared to the control. The earlier detection of network activity is in line with our previous observation of earlier synaptogenesis on SLG with respect to control (31): no/low synaptogenesis was detected on the control until 9 DIV, whereas on SLG a slight increase in the

post-synaptic current frequencies was observed starting from DIV 7. Moreover, the stronger firing levels detected till the latest observed developmental phase are in line with recent findings (43) showing that SLG increases neuronal firing by altering membrane-associated functions in cultured hippocampal neurons. Specifically, the detected increase in neuronal activity was demonstrated to be caused by increased cell excitability due to graphene itself, which induces the tuning of extracellular ion distribution.

In this investigation, we have also demonstrated that the number of neurons was generally higher on LG-SLG with respect to control cultures, influencing the cell density and thus the functional properties of developing networks (149,153). This, together with the earlier synaptogenesis already demonstrated (31) can suggest also a better coupling of the neurons with the LG-SLG substrate, as previously reported in the literature (107), with the final effect of accelerating the developmental processes respect to the control MEAs.

4.3 Conclusions

The long-term development of neuronal networks on LG SLG interface from the first week *in vitro* up to complete network maturation has been demonstrated. LG-SLG has proved to be a very favorable interface for neuron adhesion and growth. No major morphological differences with respect to control have been detected. Remarkably, neuronal network activity was detected earlier on LG-SLG and a more synchronous behavior of the network was recorded. The higher survival rate, the higher number of adhered cells and of firing activity indicates that the LG-SLG devices not only are compatible with the physiological functionality of neuronal network, but they have an improved detection capability, possibly due to a better neuron/substrate coupling.

4.4 Perspective

As a perspective, we would like to study the evoked activity of the neuronal network by exciting one of the MEA electrodes and studying the propagation of this stimulus in the whole network by recording the response of the rest of the electrodes.

We have performed a preliminary study on this. We have randomly excited one of the electrodes (cross mark in Fig. 4.8 (B)) and studied the response of the network to that stimulus on SLG MEA versus conventional MEA (control). We recorded the neuronal network activity by the rest of the electrodes (Fig. 4.8 (A)). Most of the electrodes of SLG-MEA have been active indicating a good propagation of the stimulus, which means that the neuronal network was communicating as compared with the control where only a few electrodes have responded (Fig. 4.8). The firing rate (FR) was stronger with longer duration on SLG MEA versus control.

We would like to perform more experiments to reproduce these preliminary results and this way to show that SLG functionalized MEA enhances the communication of neuronal networks.

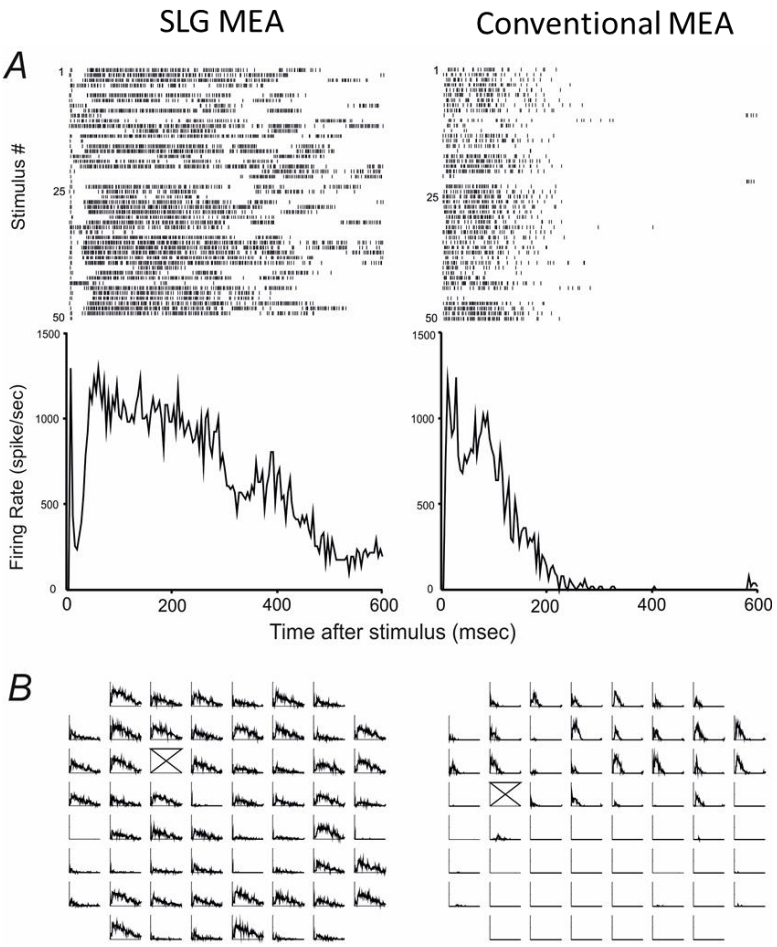

Figure 4.8 Evoked activity analysis of SLG-MEA versus conventional MEA (control). Response of the neuronal network activity to the stimulus (A).

Appendices

Appendix A

In this section, I have presented a side project that I have been also involved in. The focus of the project was to study neuronal-like response of N2a living cells to nanoporous patterns of thin supported anodic alumina.

Introduction

The role of surface morphology of foreign bodies in their integration with living tissues has been widely recognized (154). In particular, cell adhesion is critically affected by roughness, which means a spatially distributed pattern of surface amplitude features (Gentile et al. 2012, Wennerberg and Albrektsson, 2000). Adhesion is of particular importance in living cell experiments because it is connected not only to attachment to a seeding substrate after making contact, but also to active interaction with it, and is in turn affected by the surrounding medium, including the extracellular matrix. Actually, adhesion deals with chemical/physical interaction with the substrate, during which possible development of focal adhesion sites occurs (155).

Among the several possible approaches to cell adhesion engineering of the substrates available by current advanced technologies (e.g. based on electron beam lithography or focused ion beam), it is our opinion that the use of anodic porous alumina (APA) (156) is particularly promising. This technique holds the capability for patterning large areas in inexpensive manner (157), which could be used for disposable devices, may they be living-cells-mediated chemical sensors or bio-assays for diagnostics (158–161). The ‘natural lithography’ nanopatterning obtained by anodization, though at a cost of some morphological inhomogeneity, appears to be not only fast for large-area patterning but also free from undesired contamination by polymer resist scum or solvent traces, and open to possible functional

developments obtained by either loading the pores with bioactive drugs (162) or chemically modifying the pore walls, thus providing a platform for chemical sensors (163).

N2a cells are cells from a mouse neuroblastoma cell line, which are often used to investigate their neuronal-like extensions. N2a can actually differentiate to neurons and their differentiation is usually obtained in particular conditions of culturing, such as serum deprivation or addition of retinoic acid to the culture medium (109). Their tendency to differentiate to neurons can be assessed not only by the overall qualitative cell morphology as shown around the soma but can be quantitatively expressed by the number and length of neurite-like extensions (164).

In this work, we have seeded N2a cells on thin APA fabricated onto glass substrates, and investigated their response during culture at different times in culture. The cells have been stained with different dyes, allowing the visualization, under confocal microscopy, of both the cell nuclei, for cell counting purposes, and the cell extensions. Scanning electron microscopy (SEM) has also been used to provide information about the cell shape. The results are presented and discussed, in view of identification of the effect of substrate morphology on the behavior of the living cells, with particular attention on their possible differentiation to distinct neuronal cell types.

Experimental

Thin APA fabrication and characterization

The substrates have been fabricated according to a protocol already established and presented in previous publications (C. Toccafondi, Thorat, et al. 2014; C. Toccafondi et al. 2015; C. Toccafondi et al. 2016; C. Toccafondi, Stępniowski et al. 2014). Shortly, a ~100 nm thick layer of metallic aluminum was first deposited on two-inches diameter glass wafers by means of electron-beam evaporation. The aluminum-coated side-face was loaded as the bottom of a special Teflon beaker, where the outer

annular crown was contacted to the positive electrode of a high-voltage DC power supply (Agilent N5751A). The beaker was filled with 50 mL 0.3 M aqueous H_3PO_4. The cathode was a platinum basket, held dipping in the electrolyte from the top, at a distance of ~2 cm to the wafer. Mixing was provided by a magnetic stirrer, hanging inside the electrolyte, ~2 cm above the platinum basket. Anodization was carried out at constant voltage of 150 V, with a limiting current of 1 A. The process typically lasted 3 min, after which the current dropped to zero after consumption of the metallic aluminum and self-opening of the circuit, at which point the power supply was switched off. Post-fabrication treatment of the APA-coated glass was carried out *in situ*, by letting the surface exposed to the same etching solution for different times, of 0, 10, 20 and 30 min. This treatment resulted into increasing pore size, at constant pore spacing of 200 nm as set by the applied voltage. The sequence of increasing pore size has been coded for with letters from A to D, for pore diameter from 60 nm to 120 nm, respectively.

Cell culture

The N2a mouse neuroblastoma cell line (ATCC CCL-131) was maintained as a monolayer in Dulbecco's Modified Eagle medium (DMEM) (Gibco, UK), 10% Fetal Bovine Serum Inactivated (FBS), and 1% Penicillin Streptomycin (PS) at 37°C with 5% CO_2 and used in the experiments between passages 20-24. The cells were split when reaching a confluency of <80%. Then the cells were seeded on APA substrates (in duplicates) at a cell density of $1x10^3$ cells/mm^2 and left in culture for 2 days *in vitro* (DIV) of incubation. After this culturing time, they reached the desired level of confluency allowing to perform quantitative analysis for cell counting and differentiation.

Immunofluorescence staining and image analysis

Immunofluorescence staining was performed following the previously described procedure (110,169). In brief, the cultures on APA were fixed with 4% paraformaldehyde in PBS for 30 min. After

permeabilization with 0.1% Triton X-100 in PBS for 10 min four times, the cultures were incubated with PBS containing 5% goat serum and 0.1% Triton X-100 for 1 h. The permeabilized cultures were incubated overnight at 4°C with primary antibodies (1:100 anti-microtubule associated protein 2, MAP2, mouse IgG, Sigma-Aldrich) in PBS containing 5% goat serum and were rinsed with PBS for 10 min four times. The cultures were then incubated with secondary antibody (1:200 Alexa Fluor 488-labeled anti-mouse IgG, Molecular Probes) in PBS containing 5% goat serum for 2 h at room temperature and rinsed four times. The substrates were then mounted on glass slides/thin coverslips with ProLong anti fade mounting media with DAPI for nuclear staining (Thermo Fisher Scientific, Waltham, MA, USA). Fluorescence images were captured using a Nikon Inverted Microscope TiE equipped with a confocal microscope at excitation wavelengths λ=405 nm and λ=488 nm at 10X, 20X and 60X magnification.

Image analysis was performed using Nikon Imaging Software (NIS-Elements, Nikon Instruments, Japan) and ImageJ Software (NIH, Bethesda, Maryland, USA). Images were taken at least at three different cell locations for each specimen. To determine the total cell density, the samples were stained with DAPI and the respective gray-level images were transformed into black and white images by setting proper binarization threshold. Objects in the binary images that were slightly overlapped were separated by Watershed separation using ImageJ software, and finally the separated nuclei were counted. To quantify the number of differentiated cells, we counted the number of cells with neuronal-like process extensions (neurites) following the previously described method (169). Percentage of differentiated cells, i.e. neuritogenesis, was defined as (differentiated cells/total number of adhered cells) X 100. An example of high-resolution image used for the above quantitative analysis with the graphic description of the respective processing is presented in Chapter 3, Supporting Information, Fig. S1.

Statistical Analysis

Data within the text are expressed as mean ± standard error of the mean. Analysis of variance was carried out by using OriginPro (OriginLab Corporation, Northampton, MA, USA), assessing the statistical significance of the difference between all pairs of samples according to Tukey test.

Scanning electron microscopy

For SEM imaging, the N2a cells were processed following a protocol reported in detail in previous studies (31). Briefly, after fixation, the cells were extensively rinsed and post-fixed for 1 h on ice in a solution of 1% osmium tetroxide (Sigma-Aldrich) in 0.1 M cacodylate buffer. After several washes with ice-cold ultrapure water, fixed samples were rinsed for 5 min in increasing concentrations of filtered ice-cold ethanol (30, 50, 70, 90, and 96%), followed by two 15 min rinses with ice-cold 100% ethanol. The dehydration with ethanol was followed by gradual replacement with ice-cold hexamethyldisilazane (Sigma-Aldrich) that was allowed to evaporate in a fume hood overnight. The cells were finally coated with 10 nm Au layer and observed with a JSM-6490LA variable pressure SEM (JEOL, Japan) working in high-vacuum mode at 30 kV.

Results and Discussion

In Fig. A1, we report a typical sequence of large-scope confocal images acquired on APA substrates with different pore size, as well as on the control of flat smooth native-oxide-coated aluminum. These large-scope images are presented to show the typical behavior of cells on the different APA substrates. It appears that the number of cells (blue DAPI spots) is higher for A substrate, in which case it is quite similar to that obtained on the control.

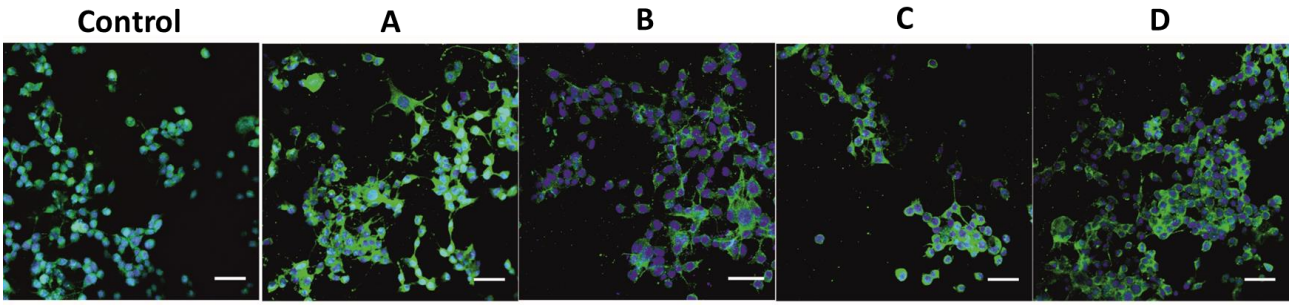

Figure A.1 One representative sequence of large-scope confocal images of N2a cells after 2 DIV cultured on control and on APA with different pore size, from 60 nm for A to 120 nm for D (scale bar is 50 µm).

From sets of images like that in Fig. A1, the surface efficiency in cell adhesion has been obtained by cell counting. The results of this analysis is summarized and presented in Fig. A2.

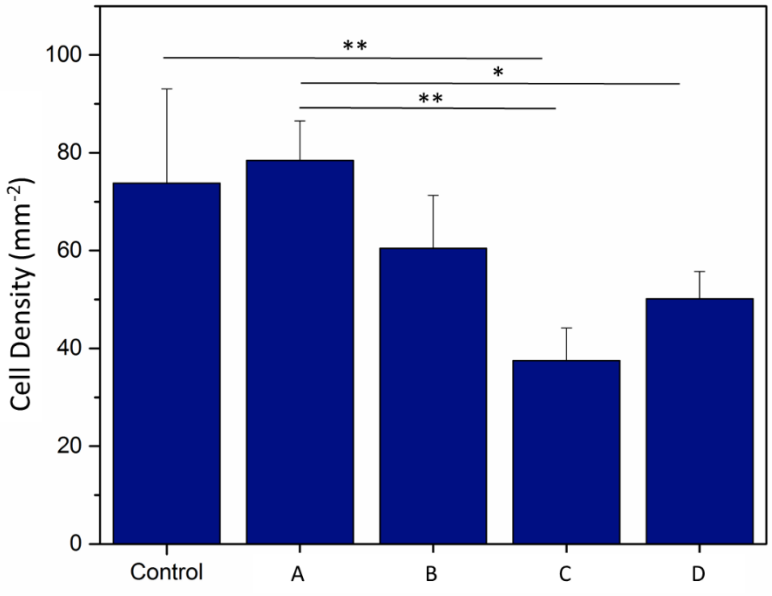

Figure A.2 Quantitative parameter of adhering cells: number of cells on substrates with different pore size, increasing from A (60 nm) to D (120 nm), including the control (no pores). Pairs joined by lines show statistically significant difference (∗: $p<0.05$, **: $p<0.01$).

In addition to cell counting, the possible effects of the substrate morphology on different cell behavior, for example associated with cell shape, may also be addressed from the confocal fluorescence imaging. After proper staining, the thin cell processes extending on the substrate surface have also been identified. From images with higher resolution than those in Fig. A1 (see Fig.S1), the neuritogenesis parameter has been calculated (refer to the Experimental section, Immunofluorescence Staining and Image Analysis). This result is presented in Fig. A3(a).

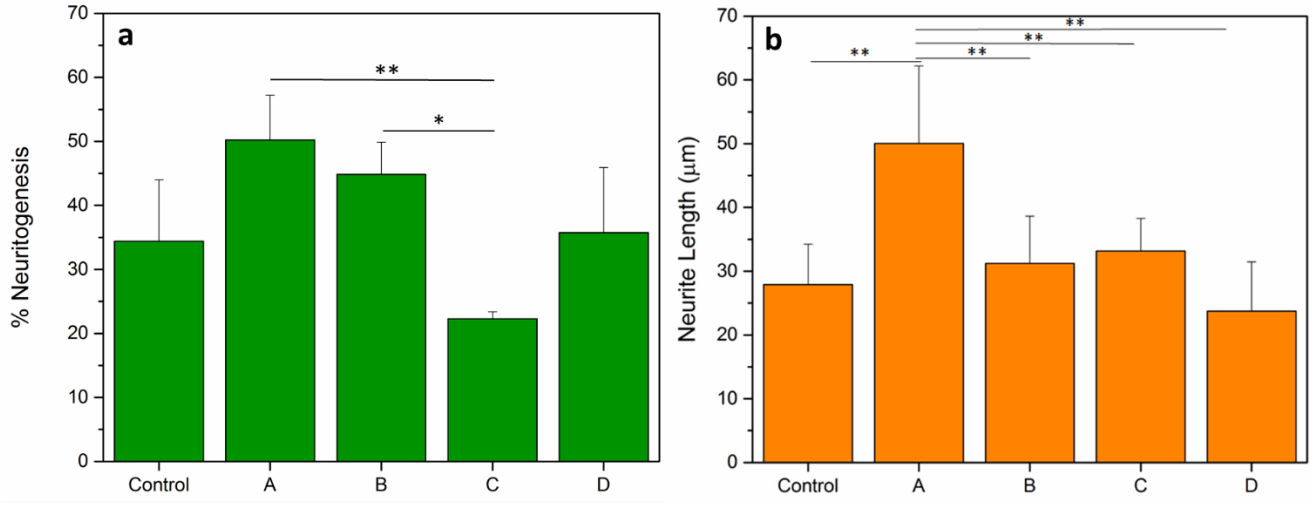

Figure A.3 Functional parameters of adhering cells: a) neuritogenesis, b) mean normalized length of the existing neuritic-like processes. Pairs joined by lines show statistically significant difference (*:$p<0.05$, **: $p<0.01$).

It appears from Fig. A3(a) that the cells seeded on APA with smallest pore size A present the larger number of neuritic extensions, whereas this number is minimum at some intermediate pore size C. In particular, the differences are statistically significant for the comparisons of A to C ($p<0.01$) and B to C ($p<0.05$).

In Fig. A3(b), the mean length of the identified neuritic extensions is plotted instead. Also for this quantity, a maximum appears for the smallest pores samples coded as A. In this case, the difference of

A with all the other samples is statistically significant for all pairs at the higher level of $p<0.01$. Again we conclude that the APA substrate with smallest pores A drives the N2a cells towards a neuron-like behavior.

The above hypothesis has also been tested by SEM imaging. In Fig. A4, representative SEM images of N2a cells are shown, at different magnifications, for cells adhering on opposite limiting pore size cases of A and D APA substrates. These images allow one to better identify the cell edges with respect to the substrate as compared with confocal images, and make shape categorization more clear and straightforward. Indeed, from the SEM images, it appears that on A substrates the overall cell shape evolves to the direction of neurons, with several narrow extensions, whereas for e.g. D substrate, the cell cytosol appears more evenly extended all around its edges, with no dominating direction. Therefore, the apparent neuritogenesis, driven by the pore size, as suggested by the analysis of Fig. A3, is confirmed.

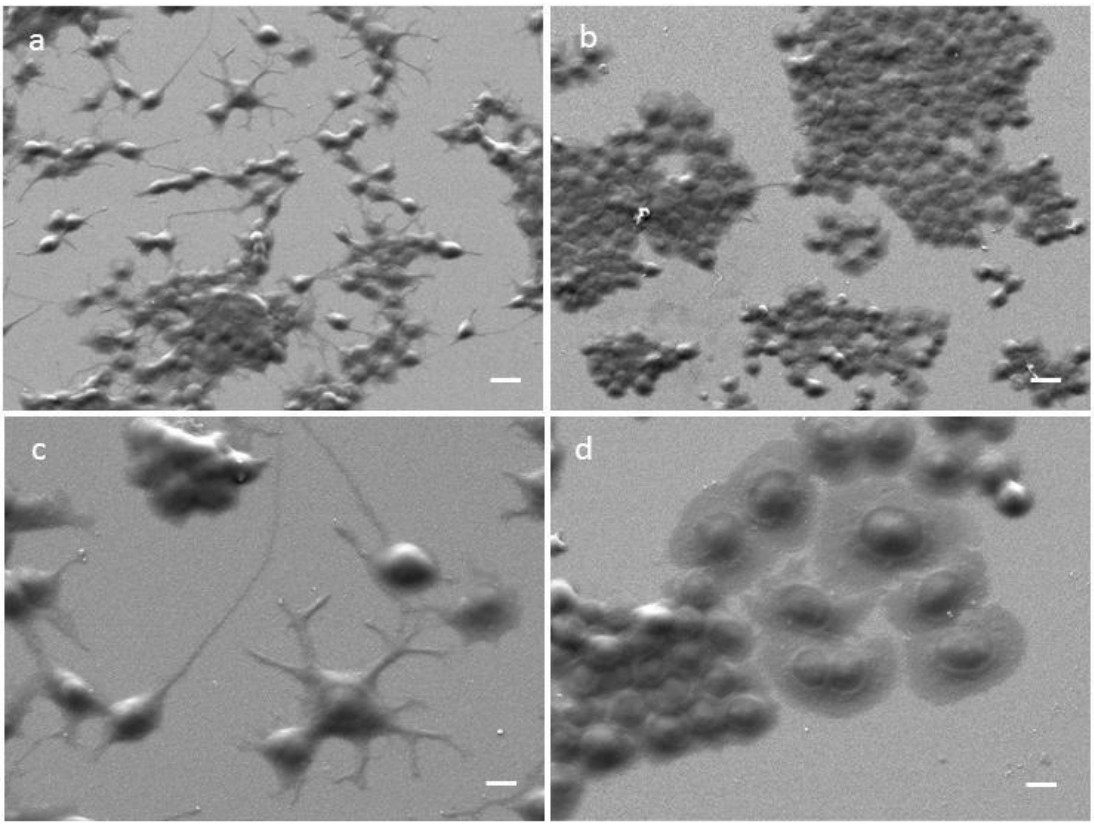

Figure A.4. Representative SEM images of N2a cells adhered on different APA substrates. Pore size seems to affect neurite outgrowth: a,c) (left column) on A APA, differentiated cells, and b,d) (right column) on D APA, undifferentiated cells, respectively. a,b) (top row) 300X magnification, 20 µm scale bar, and c,d) (bottom row) 600X magnification, 10 µm scale bar.

From the cell number plotted in Fig. A.2, it seems that the seeded cells preferentially adhere on A APA substrates, with the smallest pore size (~60 nm diameter). Additionally, both quantities plotted in Fig. A3, which represent the tendency to develop into neuronal cells, showed a maximum for APA substrates with the same pore size, namely type A. According to the smallest porosity appearing to be the best for cell adherence, this result is in agreement with results of cell adhesion on a different yet also nanoporous material, namely porous Si (Gentile et al. 2012). In that case, only two pore sizes were investigated, which were both lower than the present values investigated here (namely 5 and 20 nm pore diameter). Since we did not investigate pores as small as those ones, it is possible that still smaller

pores in APA could give even higher scores of cell adhesion than observed in this work. However, the numbers already observed here are encouraging, in that they are at least on the same level of the non-porous substrate, such that the possible improvement for even smaller pores would represent a further increase with respect to this control.

In fact, the existing literature on the pore size effect of APA substrates on cell adhesion is controversial, as there is no general consensus on this topic. This may partly be due to the different cell types investigated. For example, both Karlsson *et al.* (170) and Song *et al.* (171) found similar results as the present ones and those of Gentile *et al.*, in that they also observed enhanced living cell activity, in terms of cell number, on APA substrates with smaller pores, namely 20 nm *vs* 200 nm diameter for PMN leukocytes and 20 nm *vs* 100 and 200 nm diameter for MG63 osteoblast cell line, respectively. However, Song *et al.* observed higher cell elongation and mineralization for cells grown on the APA with largest pore size (200 nm). On the same MG63 cell type of Song *et al.* (171), in a former work by Salerno *et al.* (172), even the number of cells was higher for intermediate pore size and not for the smallest available pores, but in that case some interplay due to the independent APA parameter of the type of growth (potentiostatic vs galvanostatic) may also have played a role. Still for a different cell type, namely NIH-3T3 fibroblasts, we previously observed opposite results in terms of cell number as the largest pores performed better (165). Graham *et al.* investigated the behavior of NG108-15 neurons (173), and observed that no cell number was significantly different on various pore size substrates; however, by detaching the cells under centrifugation they measured the cell adhesion force, and observed that higher speed was required for detachment from larger pore substrates. Finally, Kant *et al.* (161) seeded neuroblastoma cells on APA substrates with 50-110 nm pore diameter grading, obtained on the same sample by galvanostatic anodizing aluminum tilted at 45° to the cathode, but observed different cell behavior in both number of adherent cells and development of neuronal-like cell shape

and connectivity only for partly collapsed pores forming brush-like structures, which occurred for the highest current density (150 mA/cm^2). Overall, one may conclude that the effect of pore size on the adhering cell number is at least cell-type dependent, i.e., different cells may possibly react to the pore size with different behavior, specific to their type.

One limitation of the present work is the restricted range of pore size investigated. Actually, it should be noticed that the pore size (d) has an upper limit in the pore spacing (or cell size) (D), since it should always be d<D, to avoid collapse of the porous structure. In fact, D can be tuned by changing the anodization voltage. However, a change in D also implies a change in pore density, which is proportional to D^{-2}. Therefore, if the goal is to investigate the separate effect of d only, this should be done at constant D.

Clearly, the types of pores that we consider in this work are not the microscale pores allowing cell filaments to enter, cell nutrients to pass through, and eventually whole cells being loaded and vascularization to occur. However, those functions are more useful in scaffold materials, disappearing progressively in time, where the cell tissue or at least network should finally replace the original foreign material and make the 3D bulk. On the contrary, here we address the interaction between permanent solid surface-adhering cell, such as in the case of permanent implants as used in orthopedics or dentistry, where no massive damage tissue has to be regenerated and adhesion and biocompatibility are rather requested for the foreign surface remaining *in situ* indefinitely over time.

Actually, as a preliminary test pointing to a new extensive experimental campaign, we have also tried to perform one similar run of cell seeding on APA substrates with different pore size for primary neurons. A sequence of typical confocal images is shown in Fig.S2, and the overall quantitative results of the respective cell counting are presented in Fig.S3, for the single experiment done. It appears that also for neurons, same as for the N2a cells, the number of cells is higher on type A substrates. This

preliminary result seems to confirm the higher affinity of neuronal-like cells for the APA surface with small (60 nm diameter) pores. Obviously, for reasons yet to be understood, the nanoporous structure of APA substrates apparently induces an enhanced expression of neuronal cell characters for the case of pores in the smaller size as to the range investigated here (60-120 nm). However, a more comprehensive set of experiments will be requested to validate this result. These results are promising in view of application of APA as a platform for the development of neuronal bioassays based on cell interconnectivity, of which in our group we have some former experience that resulted already in a related patent (174).

Summary and Conclusions

Within the limitations of the experiment presently reported, one can draw the following conclusions:

1. There seem to be no effect of the pore size on the cell adhesion for the considered cell type (N2a cell line).

2. The highest number of cells adhering to the nanoporous substrates of thin APA is at least the same or even higher than those adhering on the control substrate; this makes the substrates promising for possible future developments of APA-based surfaces for living cells biosensors/bioassays.

3. Rather than affecting the number of adhering cells, the APA pore size seems to have a possible effect on their neuritogenesis; this property may potentially be of use in driving cell extension in a given area, for example in tissue engineering applications. It is speculated that the voids of the pore mouths can act on the cell seeding surface as a modulator of the mechanical stiffness: the larger the pores, i.e. the higher the coverage of pore voids, the lower the effective equivalent stiffness of the surfaces, as compared to flat, compact alumina. Therefore, experiments can be conceived where the surface is not just void - i.e. filled with ‘zero stiffness’ air - but rather with a more fine ‘stiffness modulator’, e.g. a

solution-processable polymer such as polymethyl methacrylate, polystyrene or polyethylene, to be cast into the pores and the excess be removed by e.g. high speed spin-coating or wet-chemical removal.

Supporting Information

Similar to the case of N2a cells for Fig. 2, in a single experiment we carried out a confocal imaging after fluorescence labelling and extracted from the images quantitative information also for cultures of primary neurons. In Fig.S2, one set of representative confocal images of primary neurons cultured on APA with different pore size and fixed at 5 DIV is shown. The cells were fluorescently labelled with DAPI for cell counting and vinculin marker for quantification of cell adhesion. In this case the substrates were coated with poly-d-lysine (PDL) prior to seeding with cells. As another difference, in addition to the flat alumina as the control, here we also tested glass substrate.

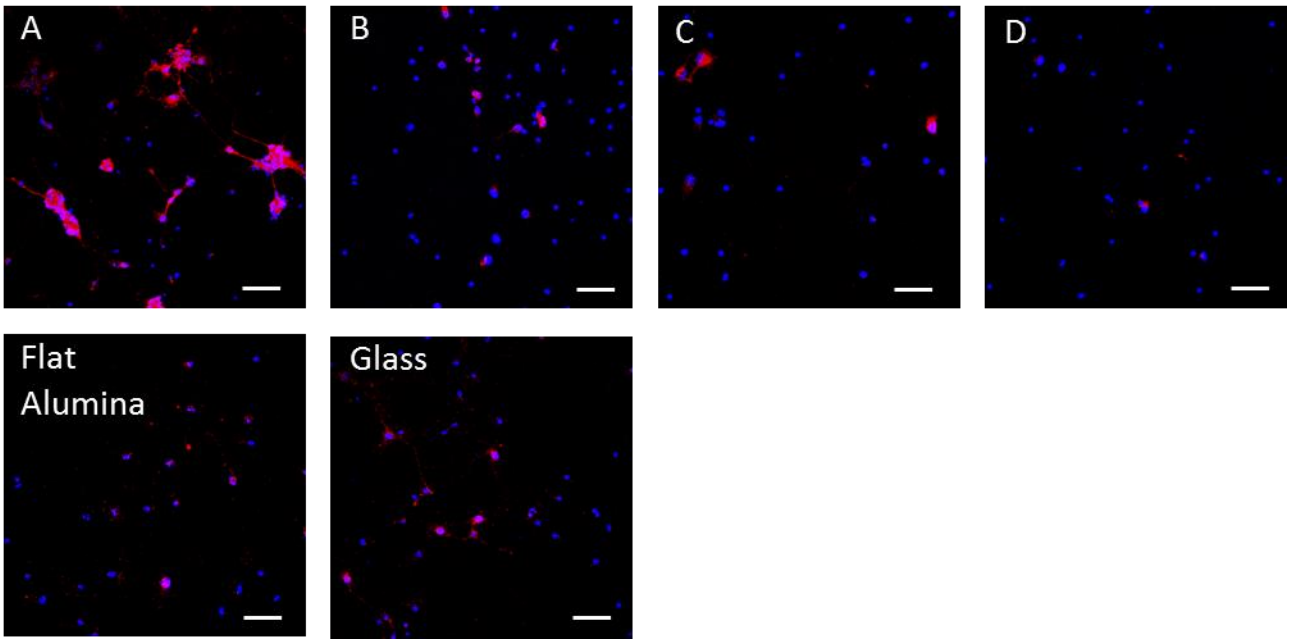

Figure A.S1: Sequence of confocal microscope images of neurons cultured on PDL-coated APA (A – D) and controls (flat alumina and glass) after fluorescence labelling (scale bar is 50 µm).

From the confocal images as in Fig. AS1, image analysis was carried out, which resulted in the quantitative data as reported in Fig. AS2.

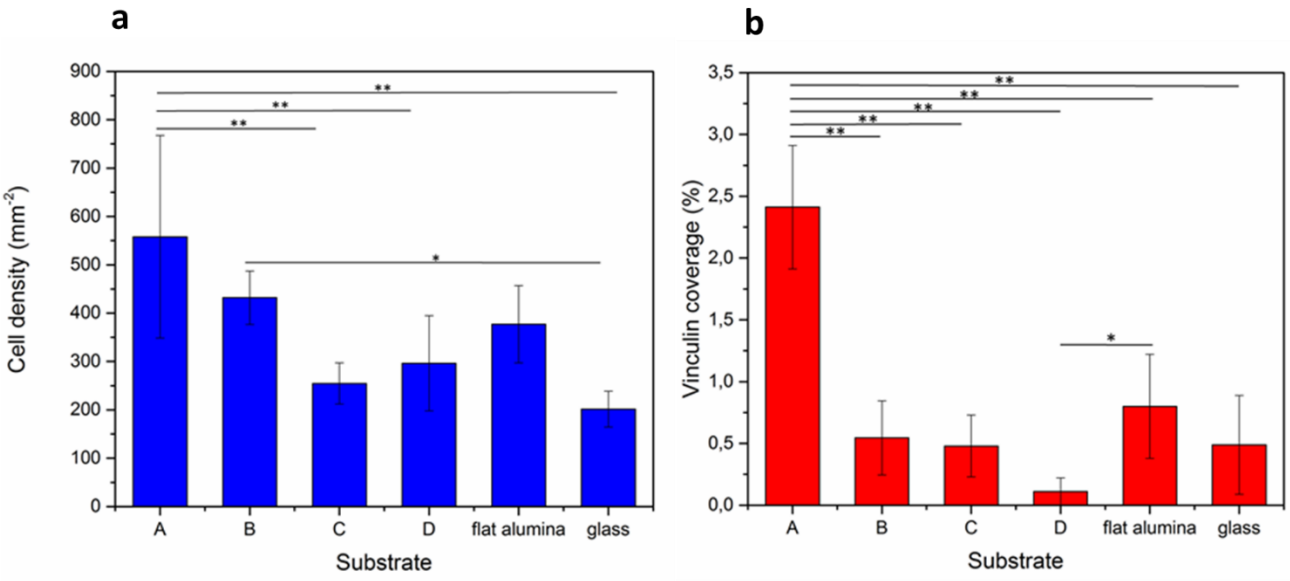

Figure A.S2 Quantitative information extracted from the confocal images: a) number of neurons, b) percentage of image area covered by vinculin. Pairs joined by lines show statistically significant difference (*: $p<0.05$, **: $p<0.01$).

The number of neurons identified on the APA substrates with different pore size (Fig. AS2(a)) allows for a crude assessment of cell adhesion, same as for the N2a cells. Again, a maximum number of cells is observed for A type substrates (i.e. smaller pore diameter, approx. 60 nm). As for the number of focal adhesions in Fig. AS2(b), one can see that the difference between A and all the other substrates are even more evident.

As an additional piece of information, from several SEM images and particularly for the case of APA A, it appears that the cell membrane is well spread and adherent to the nanopores, see Fig. AS3 below.

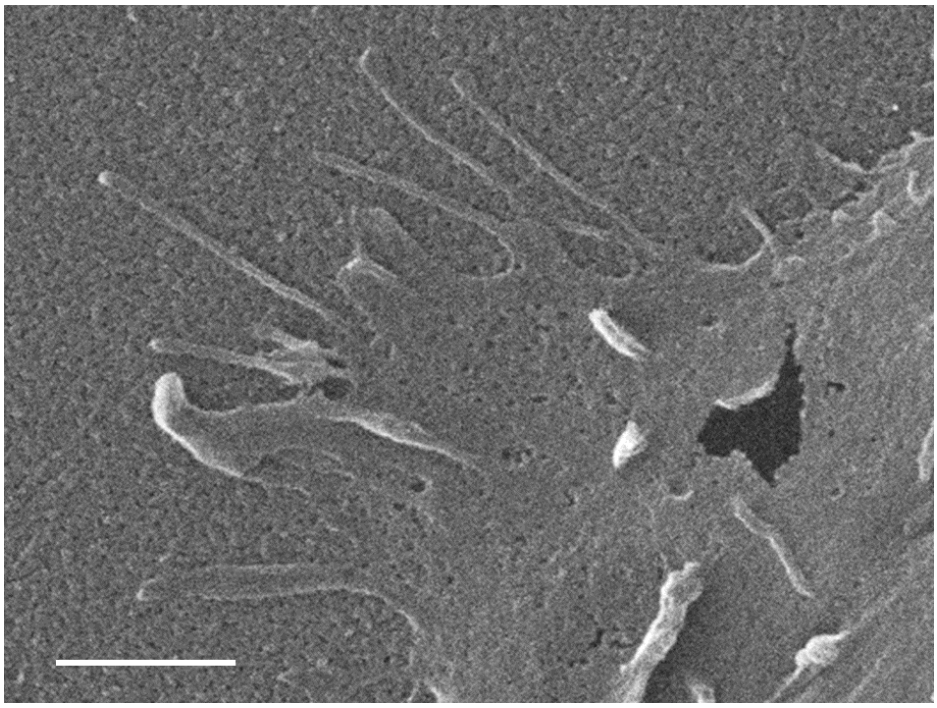

Fig. A.S3 Qualitative assessment of neuronal cell adhesion on APA A, (scale bar is 1 µm).

References

1. Bitounis D, Ali-Boucetta H, Hong BH, Min D-H, Kostarelos K. Prospects and Challenges of Graphene in Biomedical Applications. Adv Mater. 2013 Apr 24;25(16):2258–68.

2. Novoselov KS, Geim AK, Morozov SV, Jiang D, Zhang Y, Dubonos SV, et al. Electric Field Effect in Atomically Thin Carbon Films. Science. 2004 Oct 22;306(5696):666–9.

3. Geim AK, Novoselov KS. The rise of graphene. Nat Mater. 2007 Mar;6(3):183–91.

4. Wick P, Louw-Gaume AE, Kucki M, Krug HF, Kostarelos K, Fadeel B, et al. Classification framework for graphene-based materials. Angew Chem Int Ed Engl. 2014 Jul 21;53(30):7714–8.

5. Cheng C, Li S, Thomas A, Kotov NA, Haag R. Functional Graphene Nanomaterials Based Architectures: Biointeractions, Fabrications, and Emerging Biological Applications. Chem Rev. 2017 08;117(3):1826–914.

6. Bianco A. Graphene: safe or toxic? The two faces of the medal. Angew Chem Int Ed Engl. 2013 May 3;52(19):4986–97.

7. Gomez De Arco L, Zhang Y, Schlenker CW, Ryu K, Thompson ME, Zhou C. Continuous, highly flexible, and transparent graphene films by chemical vapor deposition for organic photovoltaics. ACS Nano. 2010 May 25;4(5):2865–73.

8. Muñoz R, Munuera C, Martínez JI, Azpeitia J, Gómez-Aleixandre C, García-Hernández M. Low Temperature Metal Free Growth of Graphene on Insulating Substrates by Plasma Assisted Chemical Vapor Deposition. 2d Mater. 2017 Mar;4(1).

9. Wee B-H, Wu T-F, Hong J-D. Facile and Scalable Synthesis Method for High-Quality Few-Layer Graphene through Solution-Based Exfoliation of Graphite. ACS Appl Mater Interfaces. 2017 Feb 8;9(5):4548–57.

10. Lu J, Yang J, Wang J, Lim A, Wang S, Loh KP. One-pot synthesis of fluorescent carbon nanoribbons, nanoparticles, and graphene by the exfoliation of graphite in ionic liquids. ACS Nano. 2009 Aug 25;3(8):2367–75.

11. Kurapati R, Kostarelos K, Prato M, Bianco A. Biomedical Uses for 2D Materials Beyond Graphene: Current Advances and Challenges Ahead. Adv Mater Deerfield Beach Fla. 2016 Aug;28(29):6052–74.

12. Sahoo S, Bhattacharya P, Dhibar S, Hatui G, Das T, Das CK. Graphene/Poly(aniline-co-pyrrole) Nanocomposite: Potential Candidate for Supercapacitor and Microwave Absorbing Applications. J Nanosci Nanotechnol. 2015 Sep;15(9):6931–41.

13. Casaluci S, Gemmi M, Pellegrini V, Di Carlo A, Bonaccorso F. Graphene-based large area dye-sensitized solar cell modules. Nanoscale. 2016 Mar 7;8(9):5368–78.

14. Hess LH, Jansen M, Maybeck V, Hauf MV, Seifert M, Stutzmann M, et al. Graphene transistor arrays for recording action potentials from electrogenic cells. Adv Mater Deerfield Beach Fla. 2011 Nov 16;23(43):5045–9, 4968.

15. Eda G, Fanchini G, Chhowalla M. Large-area ultrathin films of reduced graphene oxide as a transparent and flexible electronic material. Nat Nanotechnol. 2008 May;3(5):270–4.

16. Meric I, Han MY, Young AF, Ozyilmaz B, Kim P, Shepard KL. Current saturation in zero-bandgap, top-gated graphene field-effect transistors. Nat Nanotechnol. 2008 Nov;3(11):654–9.

17. Bonaccorso F, Bartolotta A, Coleman JN, Backes C. 2D-Crystal-Based Functional Inks. Adv Mater Deerfield Beach Fla. 2016 Aug;28(29):6136–66.

18. Dufficy MK, Geiger MT, Bonino CA, Khan SA. Electrospun Ultrafine Fiber Composites Containing Fumed Silica: From Solution Rheology to Materials with Tunable Wetting. Langmuir ACS J Surf Colloids. 2015 Nov 17;31(45):12455–63.

19. Hassoun J, Bonaccorso F, Agostini M, Angelucci M, Betti MG, Cingolani R, et al. An advanced lithium-ion battery based on a graphene anode and a lithium iron phosphate cathode. Nano Lett. 2014 Aug 13;14(8):4901–6.

20. Du D, Zou Z, Shin Y, Wang J, Wu H, Engelhard MH, et al. Sensitive immunosensor for cancer biomarker based on dual signal amplification strategy of graphene sheets and multienzyme functionalized carbon nanospheres. Anal Chem. 2010 Apr 1;82(7):2989–95.

21. Kang X, Wang J, Wu H, Liu J, Aksay IA, Lin Y. A graphene-based electrochemical sensor for sensitive detection of paracetamol. Talanta. 2010 May 15;81(3):754–9.

22. El-Kady MF, Kaner RB. Scalable fabrication of high-power graphene micro-supercapacitors for flexible and on-chip energy storage. Nat Commun. 2013;4:1475.

23. Ambrosi A, Pumera M. Electrochemically Exfoliated Graphene and Graphene Oxide for Energy Storage and Electrochemistry Applications. Chem Weinh Bergstr Ger. 2016 Jan 4;22(1):153–9.

24. Bonaccorso F, Colombo L, Yu G, Stoller M, Tozzini V, Ferrari AC, et al. 2D materials. Graphene, related two-dimensional crystals, and hybrid systems for energy conversion and storage. Science. 2015 Jan 2;347(6217):1246501.

25. Tour AS and JM. Graphene Electronics, Unzipped [Internet]. IEEE Spectrum: Technology, Engineering, and Science News. 2010 [cited 2018 Dec 12]. Available from: https://spectrum.ieee.org/semiconductors/materials/graphene-electronics-unzipped

26. Yang K, Feng L, Shi X, Liu Z. Nano-graphene in biomedicine: theranostic applications. Chem Soc Rev. 2013 Jan 21;42(2):530–47.

27. Feng L, Wu L, Qu X. New horizons for diagnostics and therapeutic applications of graphene and graphene oxide. Adv Mater Deerfield Beach Fla. 2013 Jan 11;25(2):168–86.

28. Ding X, Liu H, Fan Y. Graphene-Based Materials in Regenerative Medicine. Adv Healthc Mater. 2015 Jul 15;4(10):1451–68.

29. Bramini M, Alberini G, Colombo E, Chiacchiaretta M, DiFrancesco ML, Maya-Vetencourt JF, et al. Interfacing Graphene-Based Materials With Neural Cells. Front Syst Neurosci [Internet]. 2018 Apr 11 [cited 2018 Dec 5];12. Available from: http://journal.frontiersin.org/article/10.3389/fnsys.2018.00012/full

30. Mazzatenta A, Giugliano M, Campidelli S, Gambazzi L, Businaro L, Markram H, et al. Interfacing neurons with carbon nanotubes: electrical signal transfer and synaptic stimulation in cultured brain circuits. J Neurosci Off J Soc Neurosci. 2007 Jun 27;27(26):6931–6.

31. Keshavan S, Naskar S, Diaspro A, Cancedda L, Dante S. Developmental refinement of synaptic transmission on micropatterned single layer graphene. Acta Biomater. 2018;65(December):363–75.

32. Lee C, Wei X, Kysar JW, Hone J. Measurement of the elastic properties and intrinsic strength of monolayer graphene. Science. 2008 Jul 18;321(5887):385–8.

33. Novoselov KS, Geim AK, Morozov SV, Jiang D, Katsnelson MI, Grigorieva IV, et al. Two-dimensional gas of massless Dirac fermions in graphene. Nature. 2005 Nov;438(7065):197–200.

34. Park SY, Park J, Sim SH, Sung MG, Kim KS, Hong BH, et al. Enhanced differentiation of human neural stem cells into neurons on graphene. Adv Mater Deerfield Beach Fla. 2011 Sep 22;23(36):H263-267.

35. Orive G, Anitua E, Pedraz JL, Emerich DF. Biomaterials for promoting brain protection, repair and regeneration. Nat Rev Neurosci. 2009 Sep;10(9):682–92.

36. Silva GA, Czeisler C, Niece KL, Beniash E, Harrington DA, Kessler JA, et al. Selective Differentiation of Neural Progenitor Cells by High-Epitope Density Nanofibers. Science. 2004 Feb 27;303(5662):1352–5.

37. Convertino D, Luin S, Marchetti L, Coletti C. Peripheral Neuron Survival and Outgrowth on Graphene. Front Neurosci [Internet]. 2018 Jan 22 [cited 2018 Dec 6];12. Available from: http://journal.frontiersin.org/article/10.3389/fnins.2018.00001/full

38. Li N, Zhang X, Song Q, Su R, Zhang Q, Kong T, et al. The promotion of neurite sprouting and outgrowth of mouse hippocampal cells in culture by graphene substrates. Biomaterials. 2011 Dec;32(35):9374–82.

39. Lee JS, Lipatov A, Ha L, Shekhirev M, Andalib MN, Sinitskii A, et al. Graphene substrate for inducing neurite outgrowth. Biochem Biophys Res Commun. 2015 May;460(2):267–73.

40. Akhavan O. Graphene scaffolds in progressive nanotechnology/stem cell-based tissue engineering of the nervous system. J Mater Chem B. 2016;4(19):3169–90.

41. Bae S, Kim H, Lee Y, Xu X, Park J-S, Zheng Y, et al. Roll-to-roll production of 30-inch graphene films for transparent electrodes. Nat Nanotechnol. 2010 Aug;5(8):574–8.

42. Bramini M, Sacchetti S, Armirotti A, Rocchi A, Vázquez E, León Castellanos V, et al. Graphene Oxide Nanosheets Disrupt Lipid Composition, Ca $^{2+}$ Homeostasis, and Synaptic Transmission in Primary Cortical Neurons. ACS Nano. 2016 Jul 26;10(7):7154–71.

43. Pampaloni NP, Lottner M, Giugliano M, Matruglio A, D'Amico F, Prato M, et al. Single-layer graphene modulates neuronal communication and augments membrane ion currents. Nat Nanotechnol. 2018 Aug;13(8):755–64.

44. Researchers create smallest gaps ever in nanostructures using graphene - ExtremeTech [Internet]. [cited 2018 Dec 12]. Available from: https://www.extremetech.com/computing/204194-researchers-create-smallest-gaps-ever-in-nanostructures-using-graphene

45. Zhang Y, Zhang L, Zhou C. Review of chemical vapor deposition of graphene and related applications. Acc Chem Res. 2013 Oct 15;46(10):2329–39.

46. Li X, Cai W, An J, Kim S, Nah J, Yang D, et al. Large-area synthesis of high-quality and uniform graphene films on copper foils. Science. 2009 Jun 5;324(5932):1312–4.

47. Suzuki S, Nagamori T, Matsuoka Y, Yoshimura M. Threefold atmospheric-pressure annealing for suppressing graphene nucleation on copper in chemical vapor deposition. Jpn J Appl Phys. 2014 Aug 5;53(9):095101.

48. Shihommatsu K, Takahashi J, Momiuchi Y, Hoshi Y, Kato H, Homma Y. Formation Mechanism of Secondary Electron Contrast of Graphene Layers on a Metal Substrate. ACS Omega. 2017 Nov 30;2(11):7831–6.

49. Gass MH, Bangert U, Bleloch AL, Wang P, Nair RR, Geim AK. Free-standing graphene at atomic resolution. Nat Nanotechnol. 2008 Nov;3(11):676–81.

50. Ferrari AC, Meyer JC, Scardaci V, Casiraghi C, Lazzeri M, Mauri F, et al. Raman spectrum of graphene and graphene layers. Phys Rev Lett. 2006 Nov 3;97(18):187401.

51. Zhang Y, Mendez EE, Du X. Mobility-Dependent Low-Frequency Noise in Graphene Field-Effect Transistors. ACS Nano. 2011 Oct 25;5(10):8124–30.

52. Bosi S, Ballerini L, Prato M. Carbon nanotubes in tissue engineering. Top Curr Chem. 2014;348:181–204.

53. Mazia D, Schatten G, Sale W. Adhesion of cells to surfaces coated with polylysine. Applications to electron microscopy. J Cell Biol. 1975 Jul 1;66(1):198–200.

54. Bajaj P, Rivera JA, Marchwiany D, Solovyeva V, Bashir R. Graphene-Based Patterning and Differentiation of C2C12 Myoblasts. Adv Healthc Mater. 2014 Jul;3(7):995–1000.

55. Hammarback JA, Palm SL, Furcht LT, Letourneau PC. Guidance of neurite outgrowth by pathways of substratum-adsorbed laminin. J Neurosci Res. 1985;13(1–2):213–20.

56. Lorenzoni M, Brandi F, Dante S, Giugni A, Torre B. Simple and effective graphene laser processing for neuron patterning application. Sci Rep [Internet]. 2013 Jun 6 [cited 2016 Sep 20];3. Available from: http://www.nature.com/articles/srep01954

57. Kravets VG, Grigorenko AN, Nair RR, Blake P, Anissimova S, Novoselov KS, et al. Spectroscopic ellipsometry of graphene and an exciton-shifted van Hove peak in absorption. Phys Rev B. 2010 Apr 6;81(15):155413.

58. Jun SB, Hynd MR, Dowell-Mesfin N, Smith KL, Turner JN, Shain W, et al. Low-density neuronal networks cultured using patterned poly-l-lysine on microelectrode arrays. J Neurosci Methods. 2007 Mar 15;160(2):317–26.

59. Polylysine. In: Wikipedia [Internet]. 2018 [cited 2018 Dec 12]. Available from: https://en.wikipedia.org/w/index.php?title=Polylysine&oldid=864730779

60. Rao SS, Winter J. Adhesion molecule-modified biomaterials for neural tissue engineering. Front Neuroengineering [Internet]. 2009 [cited 2018 Dec 6];2. Available from: https://www.frontiersin.org/articles/10.3389/neuro.16.006.2009/full

61. Kelly S, Regan EM, Uney JB, Dick AD, McGeehan JP, Biochip GTB, et al. Patterned growth of neuronal cells on modified diamond-like carbon substrates. Biomaterials. 2008 Jun;29(17):2573–80.

62. Wang YY, Burke PJ. Polyelectrolyte multilayer electrostatic gating of graphene field-effect transistors. Nano Res. 2014 Nov 1;7(11):1650–8.

63. Zipfel WR, Williams RM, Webb WW. Nonlinear magic: multiphoton microscopy in the biosciences. Nat Biotechnol. 2003;21(11):1369–77.

64. Chen H, Wang H, Slipchenko MN, Jung Y, Shi Y, Zhu J, et al. A multimodal platform for nonlinear optical microscopy and microspectroscopy. Opt Express. 2009;17(3):1282–90.

65. Meyer T, Schmitt M, Dietzek B, Popp J. Accumulating advantages, reducing limitations: Multimodal nonlinear imaging in biomedical sciences - The synergy of multiple contrast mechanisms. J Biophotonics. 2013;6(11–12):887–904.

66. Diaspro A, Bianchini P, Vicidomini G, Faretta M, Ramoino P, Usai C. Multi-photon excitation microscopy. Biomed Eng OnLine. 2006;5(1):36.

67. Davydova D, de la Cadena A, Akimov D, Dietzek B. Transient absorption microscopy: Advances in chemical imaging of photoinduced dynamics. Laser Photonics Rev. 2016;10(1):62–81.

68. Davydova D, De La Cadena A, Demmler S, Rothhardt J, Limpert J, Pascher T, et al. Ultrafast transient absorption microscopy: Study of excited state dynamics in PtOEP crystals. Chem Phys. 2016;464:69–77.

69. Chong S, Min W, Xie XS. Ground-State Depletion Microscopy: Detection Sensitivity of Single-Molecule Optical Absorption at Room Temperature. J Phys Chem Lett. 2010 Dec 2;1(23):3316–22.

70. Cui Q, Ceballos F, Kumar N, Zhao H. Transient absorption microscopy of monolayer and bulk WSe2. ACS Nano. 2014;8(3):2970–6.

71. Guo Z, Manser JSS, Wan Y, Kamat PV V., Huang L. Spatial and temporal imaging of long-range charge transport in perovskite thin films by ultrafast microscopy. Nat Commun. 2015 Dec 23;6(1):1–8.

72. Guo Z, Wan Y, Yang M, Snaider J, Zhu K, Huang L. Long-range hot-carrier transport in hybrid perovskites visualized by ultrafast microscopy. Science. 2017;356(6333):59–62.

73. Guo Z, Zhou N, Williams OF, Hu J, You W, Moran AM. Imaging Carrier Diffusion in Perovskites with a Diffractive Optic-Based Transient Absorption Microscope. J Phys Chem C. 2018 May 17;122(19):10650–6.

74. Jung Y, Slipchenko MN, Liu CH, Ribbe AE, Zhong Z, Yang C, et al. Fast Detection of the Metallic State of Individual Single-Walled Carbon Nanotubes Using a Transient-Absorption Optical Microscope. Phys Rev Lett. 2010 Nov 15;105(21):217401.

75. Wan Y, Guo Z, Zhu T, Yan S, Johnson J, Huang L. Cooperative singlet and triplet exciton transport in tetracene crystals visualized by ultrafast microscopy. Nat Chem. 2015 Oct 14;7(10):785–92.

76. Gabriel MM, Kirschbrown JR, Christesen JD, Pinion CW, Zigler DF, Grumstrup EM, et al. Direct imaging of free carrier and trap carrier motion in silicon nanowires by spatially-separated femtosecond pump-probe microscopy. Nano Lett. 2013 Mar 13;13(3):1336–40.

77. Lo SS, Major TA, Petchsang N, Huang L, Kuno MK, Hartland G V. Charge carrier trapping and acoustic phonon modes in single CdTe nanowires. ACS Nano. 2012 Jun 26;6(6):5274–82.

78. Wong CY, Penwell SB, Cotts BL, Noriega R, Wu H, Ginsberg NS. Revealing exciton dynamics in a small-molecule organic semiconducting film with subdomain transient absorption microscopy. J Phys Chem C. 2013;117(42):22111–22.

79. Hartland G V. Ultrafast studies of single semiconductor and metal nanostructures through transient absorption microscopy. Chem Sci. 2010;1(3):303–9.

80. Malic E, Knorr A. Graphene and Carbon Nanotubes: Ultrafast Relaxation Dynamics and Optics. Graphene and Carbon Nanotubes: Ultrafast Relaxation Dynamics and Optics. Weinheim, Germany: Wiley-VCH Verlag GmbH & Co. KGaA; 2013. 1–9 p.

81. Nair RR, Blake P, Grigorenko AN, Novoselov KS, Booth TJ, Stauber T, et al. Fine structure constant defines visual transparency of graphene. Science. 2008;320(5881):1308.

82. Mak KF, Shan J, Heinz TF. Seeing many-body effects in single- and few-layer graphene: Observation of two-dimensional saddle-point excitons. Phys Rev Lett. 2011;

83. Dawlaty JM, Shivaraman S, Chandrashekhar M, Rana F, Spencer MG. Measurement of ultrafast carrier dynamics in epitaxial graphene. Appl Phys Lett. 2008;92(4).

84. Breusing M, Kuehn S, Winzer T, Malić E, Milde F, Severin N, et al. Ultrafast nonequilibrium carrier dynamics in a single graphene layer. Phys Rev B - Condens Matter Mater Phys. 2011;83(15):1–4.

85. Newson RW, Dean J, Schmidt B, van Driel HM. Ultrafast carrier kinetics in exfoliated graphene and thin graphite films. Opt Express. 2009;17(4):2326.

86. Hale PJ, Hornett SM, Moger J, Horsell DW, Hendry E. Hot phonon decay in supported and suspended exfoliated graphene. Phys Rev B - Condens Matter Mater Phys. 2011;83(12):4–7.

87. Brida D, Tomadin A, Manzoni C, Kim YJ, Lombardo A, Milana S, et al. Ultrafast collinear scattering and carrier multiplication in graphene. Nat Commun. 1AD;4(May):1–9.

88. Kumar S, Anija M, Kamaraju N, Vasu KS, Subrahmanyam KS, Sood AK, et al. Femtosecond carrier dynamics and saturable absorption in graphene suspensions. Appl Phys Lett. 2009;95(19):2007–10.

89. Shang J, Ma L, Li J, Ai W, Yu T, Gurzadyan GG. Femtosecond pump-probe spectroscopy of graphene oxide in water. J Phys Appl Phys. 2014;47(9).

90. Huang L, Hartland G V., Chu LQ, Luxmi, Feenstra RM, Lian C, et al. Ultrafast transient absorption microscopy studies of carrier dynamics in epitaxial graphene. Nano Lett. 2010;10(4):1308–13.

91. Gao B, Hartland G, Fang T, Kelly M, Jena D, Xing H, et al. Studies of intrinsic hot phonon dynamics in suspended graphene by transient absorption microscopy. Nano Lett. 2011;11(8):3184–9.

92. Grancini G, Martino N, Bianchi M, Rizzi LG, Russo V, Li Bassi A, et al. Ultrafast spectroscopic imaging of exfoliated graphene. Phys Status Solidi B Basic Res. 2012;249(12):2497–9.

93. Li J, Zhang W, Chung T, Slipchenko MN, Chen YP, Cheng J-X, et al. Highly sensitive transient absorption imaging of graphene and graphene oxide in living cells and circulating blood. Sci Rep. 2015;5(February):12394.

94. Patel H, Havener RW, Brown L, Liang Y, Yang L, Park J, et al. Tunable Optical Excitations in Twisted Bilayer Graphene Form Strongly Bound Excitons. Nano Lett. 2015;15(9):5932–7.

95. Huang K-CC, McCall J, Wang P, Liao C-SS, Eakins G, Cheng J-XX, et al. High-Speed Spectroscopic Transient Absorption Imaging of Defects in Graphene. Nano Lett. 2018;18(2):1489–97.

96. Bianchini P, Korobchevskaya K, Zanini G, Diaspro A. Pump-Probe Nanoscopy by Means of Transient Absorption Saturation. In: 2018 20th International Conference on Transparent Optical Networks (ICTON). IEEE; 2018. p. 1–4.

97. Schindelin J, Arganda-Carreras I, Frise E, Kaynig V, Longair M, Pietzsch T, et al. Fiji: An open-source platform for biological-image analysis. Nature Methods. 2012.

98. Kelvin probe force microscope. In: Wikipedia [Internet]. 2018 [cited 2018 Dec 12]. Available from: https://en.wikipedia.org/w/index.php?title=Kelvin_probe_force_microscope&oldid=828252372

99. Lin W, Tian B, Zhuang P, Yin J, Zhang C, Li Q, et al. Graphene-Based Fluorescence-Quenching-Related Fermi Level Elevation and Electron-Concentration Surge. Nano Lett. 2016 Sep 14;16(9):5737–41.

100. ATR-FTIR | The Bernasek Lab [Internet]. [cited 2018 Dec 12]. Available from: http://chemists.princeton.edu/bernasek/atr-ftir

101. Rozenberg M, Shoham G. FTIR spectra of solid poly-l-lysine in the stretching NH mode range. Biophys Chem. 2007 Jan;125(1):166–71.

102. Humblot V, Méthivier C, Pradier C-M. Adsorption of l-Lysine on Cu(110): A RAIRS Study from UHV to the Liquid Phase. Langmuir. 2006;22(7):3089–96.

103. Martin Müller †, René Buchet § and, Urs P. Fringeli* †. 2D-FTIR ATR Spectroscopy of Thermo-Induced Periodic Secondary Structural Changes of Poly-(l)-lysine: A Cross-Correlation Analysis of Phase-Resolved Temperature Modulation Spectra [Internet]. 1996 [cited 2018 Dec 11]. Available from: https://pubs.acs.org/doi/full/10.1021/jp9602843

104. Y L, Sy L. Preparation of LiNbO3 nanoparticles using poly(L-lysine) as a biomolecular additive. Mater Chem Phys. 2014;144(1–2):92–7.

105. Keshavan S, Oropesa-Nuñez R, Diaspro A, Canale C, Dante S. Adhesion and migration of CHO cells on micropatterned single layer graphene. 2D Mater. 2017;4(2):025022.

106. QI™ Mode - JPK Instruments [Internet]. [cited 2018 Dec 20]. Available from: https://www.jpk.com/products/atomic-force-microscopy/qi-mode

107. Akhavan O, Ghaderi E, Abouei E, Hatamie S, Ghasemi E. Accelerated differentiation of neural stem cells into neurons on ginseng-reduced graphene oxide sheets. Carbon. 2014 Jan;66:395–406.

108. Kishore A, Biswas K, N VR, Shunmugam R, Sarma JD. Functionalized single walled carbon nanotubes facilitate efficient differentiation of neuroblastoma cells *in vitro*. RSC Adv. 2014;4(96):53777–87.

109. Tremblay RG, Sikorska M, Sandhu JK, Lanthier P, Ribecco-Lutkiewicz M, Bani-Yaghoub M. Differentiation of mouse Neuro 2A cells into dopamine neurons. J Neurosci Methods. 2010;186(1):60–7.

110. El Merhie A, Ito D, Colombi I, Keshavan S, Mishra N, Miseikis V, et al. Single layer graphene functionalized MEA for enhanced detection of neuronal network development. Sens Actuators B Chem. 2018 Dec 20;277:224–33.

111. Ito D, Tamate H, Nagayama M, Uchida T, Kudoh SN, Gohara K. Minimum neuron density for synchronized bursts in a rat cortical culture on multi-electrode arrays. Neuroscience. 2010 Nov;171(1):50–61.

112. Lorenzoni M, Brandi F, Dante S, Giugni A, Torre B. Simple and effective graphene laser processing for neuron patterning application. Sci Rep [Internet]. 2013 Dec [cited 2018 Dec 6];3(1). Available from: http://www.nature.com/articles/srep01954

113. Jones IL, Livi P, Lewandowska MK, Fiscella M, Roscic B, Hierlemann A. The potential of microelectrode arrays and microelectronics for biomedical research and diagnostics. Anal Bioanal Chem. 2011 Mar;399(7):2313–29.

114. Fendyur A, Spira ME. Toward on-chip, in-cell recordings from cultured cardiomyocytes by arrays of gold mushroom-shaped microelectrodes. Front Neuroengineering [Internet]. 2012 [cited 2018 Dec 11];5. Available from: https://www.frontiersin.org/articles/10.3389/fneng.2012.00021/full

115. Chiappalone M, Vato A, Tedesco M (B.), Marcoli M, Davide F, Martinoia S. Networks of neurons coupled to microelectrode arrays: a neuronal sensory system for pharmacological applications. Biosens Bioelectron. 2003 May 1;18(5):627–34.

116. Hill AJ, Jones NA, Williams CM, Stephens GJ, Whalley BJ. Development of multi-electrode array screening for anticonvulsants in acute rat brain slices. J Neurosci Methods. 2010 Jan 15;185(2):246–56.

117. Noraberg J, Poulsen FR, Blaabjerg M, Kristensen BW, Bonde C, Montero M, et al. Organotypic Hippocampal Slice Cultures for Studies of Brain Damage, Neuroprotection and Neurorepair [Internet]. 2005 [cited 2018 Dec 11]. Available from: https://www.ingentaconnect.com/content/ben/cdtcnsnd/2005/00000004/00000004/art00010

118. Nagarah JM, Stowasser A, Parker RL, Asari H, Wagenaar DA. Optically transparent multi-suction electrode arrays. Front Neurosci [Internet]. 2015 [cited 2018 Dec 11];9. Available from: https://www.frontiersin.org/articles/10.3389/fnins.2015.00384/full

119. Neumann T, Ziegler C, Blau A. Multielectrode array recordings reveal physiological diversity of intrinsically photosensitive retinal ganglion cells in the chick embryo. Brain Res. 2008 May 1;1207:120–7.

120. Charlesworth P, Cotterill E, Morton A, Grant S, Eglen SJ. Quantitative differences in developmental profiles of spontaneous activity in cortical and hippocampal cultures. Neural Develop. 2015;10(1):1.

121. Johnstone AFM, Gross GW, Weiss DG, Schroeder OH-U, Gramowski A, Shafer TJ. Microelectrode arrays: a physiologically based neurotoxicity testing platform for the 21st century. Neurotoxicology. 2010 Aug;31(4):331–50.

122. Mescola A, Canale C, Prato M, Diaspro A, Berdondini L, Maccione A, et al. Specific Neuron Placement on Gold and Silicon Nitride-Patterned Substrates through a Two-Step

Functionalization Method [Internet]. 2016 [cited 2018 Dec 11]. Available from: https://pubs.acs.org/doi/abs/10.1021/acs.langmuir.6b01352

123. Dowell-Mesfin NM, Abdul-Karim M-A, Turner AMP, Schanz S, Craighead HG, Roysam B, et al. Topographically modified surfaces affect orientation and growth of hippocampal neurons. J Neural Eng. 2004;1(2):78.

124. Ceyssens F, Sree SP, Martens J, Puers R. Fabrication of Nanostructured Platinum with Multilevel Porosity for Low Impedance Biomedical Recording and Stimulation Electrodes. Procedia Eng. 2015 Jan 1;120:355–9.

125. Ostrovsky S, Hahnewald S, Kiran R, Mistrik P, Hessler R, Tscherter A, et al. Conductive hybrid carbon nanotube (CNT)–polythiophene coatings for innovative auditory neuron-multi-electrode array interfacing. RSC Adv. 2016;6(48):41714–23.

126. Yli-Rantala E, Pasanen A, Kauranen P, Ruiz V, Borghei M, Kauppinen E, et al. Graphitised Carbon Nanofibres as Catalyst Support for PEMFC. Fuel Cells. 2011 Dec 1;11(6):715–25.

127. Bo X, Zhou M, Guo L. Electrochemical sensors and biosensors based on less aggregated graphene. Biosens Bioelectron. 2017 Mar 15;89:167–86.

128. Kakatkar A, Abhilash TS, Alba RD, Parpia JM, Craighead HG. Detection of DNA and poly-l-lysine using CVD graphene-channel FET biosensors. Nanotechnology. 2015;26(12):125502.

129. Cohen-Karni T, Qing Q, Li Q, Fang Y, Lieber CM. Graphene and Nanowire Transistors for Cellular Interfaces and Electrical Recording. Nano Lett. 2010 Mar 10;10(3):1098–102.

130. Kuzum D, Takano H, Shim E, Reed JC, Juul H, Richardson AG, et al. Transparent and flexible low noise graphene electrodes for simultaneous electrophysiology and neuroimaging. Nat Commun. 2014 Oct 20;5:5259.

131. Park D-W, Schendel AA, Mikael S, Brodnick SK, Richner TJ, Ness JP, et al. Graphene-based carbon-layered electrode array technology for neural imaging and optogenetic applications. Nat Commun. 2014 Oct 20;5:5258.

132. Suk JW, Kitt A, Magnuson CW, Hao Y, Ahmed S, An J, et al. Transfer of CVD-grown monolayer graphene onto arbitrary substrates. ACS Nano. 2011 Sep 27;5(9):6916–24.

133. Zhou H, Yu WJ, Liu L, Cheng R, Chen Y, Huang X, et al. Chemical vapour deposition growth of large single crystals of monolayer and bilayer graphene. Nat Commun. 2013 Jun 27;4:2096.

134. Miseikis V, Convertino D, Mishra N, Gemmi M, Mashoff T, Heun S, et al. Rapid CVD growth of millimetre-sized single crystal graphene using a cold-wall reactor. 2D Mater. 2015;2(1):014006.

135. Blau A, Neumann T, Ziegler C, Benfenati F. Replica-moulded polydimethylsiloxane culture vessel lids attenuate osmotic drift in long-term cell cultures. J Biosci. 2009 Mar 1;34(1):59–69.

136. Colombi I, Mahajani S, Frega M, Gasparini L, Chiappalone M. Effects of antiepileptic drugs on hippocampal neurons coupled to micro-electrode arrays. Front Neuroengineering [Internet]. 2013 [cited 2018 Dec 11];6. Available from: https://www.frontiersin.org/articles/10.3389/fneng.2013.00010/full?utm_source=newsletter&utm_medium=web&utm_campaign=Neuroscience-w50-2013

137. Streit J. Regular oscillations of synaptic activity in spinal networks *in vitro*. J Neurophysiol. 1993 Sep 1;70(3):871–8.

138. Bologna LL, Pasquale V, Garofalo M, Gandolfo M, Baljon PL, Maccione A, et al. Investigating neuronal activity by SPYCODE multi-channel data analyzer. Neural Netw. 2010 Aug 1;23(6):685–97.

139. Maccione A, Gandolfo M, Massobrio P, Novellino A, Martinoia S, Chiappalone M. A novel algorithm for precise identification of spikes in extracellularly recorded neuronal signals. J Neurosci Methods. 2009 Feb 15;177(1):241–9.

140. Brewer GJ, Boehler MD, Ide AN, Wheeler BC. Chronic electrical stimulation of cultured hippocampal networks increases spontaneous spike rates. J Neurosci Methods. 2009 Oct 30;184(1):104–9.

141. Leondopulos SS, Boehler MD, Wheeler BC, Brewer GJ. Chronic stimulation of cultured neuronal networks boosts low-frequency oscillatory activity at theta and gamma with spikes phase-locked to gamma frequencies. J Neural Eng. 2012;9(2):026015.

142. Selinger JV, Kulagina NV, O'Shaughnessy TJ, Ma W, Pancrazio JJ. Methods for characterizing interspike intervals and identifying bursts in neuronal activity. J Neurosci Methods. 2007 May 15;162(1):64–71.

143. Pasquale V, Martinoia S, Chiappalone M. A self-adapting approach for the detection of bursts and network bursts in neuronal cultures. J Comput Neurosci. 2010 Aug 1;29(1):213–29.

144. Bisio M, Bosca A, Pasquale V, Berdondini L, Chiappalone M. Emergence of Bursting Activity in Connected Neuronal Sub-Populations. PLOS ONE. 2014 Sep 24;9(9):e107400.

145. Fabbro A, Scaini D, León V, Vázquez E, Cellot G, Privitera G, et al. Graphene-Based Interfaces Do Not Alter Target Nerve Cells. ACS Nano. 2016 Jan 26;10(1):615–23.

146. Kireev D, Seyock S, Lewen J, Maybeck V, Wolfrum B, Offenhäusser A. Graphene Multielectrode Arrays as a Versatile Tool for Extracellular Measurements. Adv Healthc Mater. 2017 Jun;6(12):1601433.

147. Pfrieger FW. Synaptic Efficacy Enhanced by Glial Cells *in vitro*. Science. 1997 Sep 12;277(5332):1684–7.

148. Biffi E, Regalia G, Menegon A, Ferrigno G, Pedrocchi A. The Influence of Neuronal Density and Maturation on Network Activity of Hippocampal Cell Cultures: A Methodological Study. PLOS ONE. 2013 Dec 27;8(12):e83899.

149. Chiappalone M, Massobrio P, Martinoia S. Network plasticity in cortical assemblies. Eur J Neurosci. 2008 Jul 1;28(1):221–37.

150. Gladkov A, Grinchuk O, Pigareva Y, Mukhina I, Kazantsev V, Pimashkin A. Theta rhythm-like bidirectional cycling dynamics of living neuronal networks *in vitro*. PLOS ONE. 2018 Feb 7;13(2):e0192468.

151. Wagenaar DA, Pine J, Potter SM. An extremely rich repertoire of bursting patterns during the development of cortical cultures. BMC Neurosci. 2006 Feb 7;7(1):11.

152. Chiappalone M, Bove M, Vato A, Tedesco M, Martinoia S. Dissociated cortical networks show spontaneously correlated activity patterns during *in vitro* development. Brain Res. 2006 Jun 6;1093(1):41–53.

153. Ichikawa M, Muramoto K, Kobayashi K, Kawahara M, Kuroda Y. Formation and maturation of synapses in primary cultures of rat cerebral cortical cells: an electron microscopic study. Neurosci Res. 1993 Feb 1;16(2):95–103.

154. Ross AM, Jiang Z, Bastmeyer M, Lahann J. Physical aspects of cell culture substrates: topography, roughness, and elasticity. Small Weinh Bergstr Ger. 2012 Feb 6;8(3):336–55.

155. Seo CH, Furukawa K, Montagne K, Jeong H, Ushida T. The effect of substrate microtopography on focal adhesion maturation and actin organization via the RhoA/ROCK pathway. Biomaterials. 2011;32(36):9568–75.

156. Losic D, Santos A, editors. Nanoporous Alumina Fabrication, Structure, Properties and Applications. Springer S. Springer; 2015.

157. Das G, Patra N, Gopalakrishnan A, Zaccaria RP, Toma A, Thorat S, et al. Fabrication of large-area ordered and reproducible nanostructures for SERS biosensor application. Analyst. 2012 Apr 21;137(8):1785–92.

158. Brüggemann D. Nanoporous Aluminium Oxide Membranes as Cell Interfaces. J Nanomater. 2013;2013:1–18.

159. Poinern GEJ, Shackleton R, Mamun SI, Fawcett D. Significance of novel bioinorganic anodic aluminum oxide nanoscaffolds for promoting cellular response. Nanotechnol Sci Appl. 2011 Jan;4:11–24.

160. Toccafondi C, Dante S, Reverberi AP, Salerno M. Biomedical Applications of Anodic Porous Alumina. Curr Nanosci. 2015;11(5):572–80.

161. Kant K, Low SP, Marshal A, Shapter JG, Losic D. Nanopore gradients on porous aluminum oxide generated by nonuniform anodization of aluminum. ACS Appl Mater Interfaces. 2010;2(12):3447–54.

162. Shayganpour A, Salerno M, Salis B, Dante S. Towards a single bioactive substrate combining SERS-effect and drug release control based on thin anodic porous alumina coated with gold and with lipid bilayers. MRS Adv. 2017;1–8.

163. Salerno M, Shayganpour A, Salis B, Dante S. Surface-Enhanced Raman scattering of self-assembled thiol monolayers and supported lipid membranes on thin anodic porous alumina. Beilstein J Nanotechnol. 2017;8:74–81.

164. Lin CH, Hsieh M, Fan SS. The promotion of neurite formation in Neuro2A cells by mouse Mob2 protein. FEBS Lett. 2011;585(3):523–30.

165. Toccafondi C, Thorat S, La Rocca R, Scarpellini A, Salerno M, Dante S, et al. Multifunctional substrates of thin porous alumina for cell biosensors. J Mater Sci Mater Med. 2014;25(10):2411–20.

166. Toccafondi C, La Rocca R, Scarpellini A, Salerno M, Das G, Dante S. Thin nanoporous alumina-based SERS platform for single cell sensing. Appl Surf Sci. 2015;351:738–45.

167. Toccafondi C, Zaccaria RP, Dante S, Salerno M. Fabrication of gold coated ultra thin anodic porous alumina substrates for augmented SERS. Materials. 2016;9:403–14.

168. Toccafondi C, Stępniowski WJ, Leoncini M, Salerno M. Advanced morphological analysis of patterns of thin anodic porous alumina. Mater Charact. 2014;94.

169. Ito D, Tamate H, Nagayama M, Uchida T, Kudoh SN, Gohara K. Minimum neuron density for synchronized bursts in a rat cortical culture on multi-electrode arrays. Neuroscience. 2010;171(1):50–61.

170. Karlsson M, Johansson A, Tang L, Boman M. Nanoporous aluminum oxide affects neutrophil behaviour. Microsc Res Tech. 2004 Apr 1;63(5):259–65.

171. Song Y, Ju Y, Morita Y, Song G. Effect of the nanostructure of porous alumina on growth behavior of MG63 osteoblast-like cells. J Biosci Bioeng. 2013 Oct;116(4):509–15.

172. Salerno M, Caneva-Soumetz F, Pastorino L, Patra N, Diaspro A, Ruggiero C. Adhesion and proliferation of osteoblast-like cells on anodic porous alumina substrates with different morphology. IEEE Trans Nanobioscience. 2013 Jun;12(2):106–11.

173. Graham AHD, Bowen CR, Taylor J, Robbins J. Neuronal cell biocompatibility and adhesion to modified CMOS electrodes. Biomed Microdevices. 2009 Oct;11(5):1091–101.

174. Berdondini L, Dante S, Marconi E, Salerno M, De Pietri Tonelli D. Process and device for the determination of alterations in neuronal connectivity and/or morphology. Italy: WIPO/PCT; WO 2013/132455 A1, 2013.

Appendix B

This section is dedicated to the whole study performed on studying the surface potential of patterned graphene by polyelectrolyte coating. I have attached the article that we published related to this work.

Thin Solid Films 660 (2018) 253–257

Contents lists available at ScienceDirect

Thin Solid Films

journal homepage: www.elsevier.com/locate/tsf

Step-by-step surface potential tuning of patterned graphene by polyelectrolyte coating

Marco Salerno[a], Amira El Merhie[b,c], Alberto Diaspro[b,d], Silvia Dante[b,*]

[a] Materials Characterization Facility, Istituto Italiano di Tecnologia, Via Morego 30, 16163 Genova, Italy
[b] Nanoscopy & NIC@IIT, Istituto Italiano di Tecnologia, Via Morego 30, 16163 Genova, Italy
[c] DIBRIS, University of Genoa, Via All'Opera Pia 13, 16145 Genoa, Italy
[d] Department of Physics, University of Genoa, Via Dodecaneso 33, 16146 Genoa, Italy

ARTICLE INFO

Keywords:
Graphene
Laser ablation
Scanning Kelvin probe microscopy
Surface potential
Polyelectrolytes

ABSTRACT

The fine control of the interfacial properties of functionalized graphene is a key point for its applications, especially in biosensing devices. We have here used an *in-house* developed technique to fabricate microsized patterned graphene via laser ablation and then we have functionalized the interface with poly-D-lysine, a biocompatible polyelectrolyte normally used as a promoter for cell adhesion. Scanning Kelvin probe microscopy shows that a surface potential contrast appears at the patterned regions, with ablated regions of silicon substrate exhibiting higher surface potential than the surrounding background, whereas both levels have negative values. By subsequent coating with the poly-D-lysine it is possible to change stepwise the surface potential levels, while keeping the contrast at the patterned regions constant, up to neutralizing the initial negative values. With further dipping in a polyelectrolyte solution of opposite sign, such as polystyrene sulfonate, it is then possible to decrease the surface potential shifting it again back to negative values. The starting substrate chosen for graphene transfer allows deciding the sign of the surface potential contrast between two adjacent regions of the pattern.

1. Introduction

The use of single or few layers graphene for the fabrication of biosensing devices is appealing, given the peculiar properties of this material (transparency, conductivity, robustness) [1]. The fabrication of devices requires the capability of controlled patterning of the surfaces by selective coating with graphene. Further, functionalization of graphene with organic or biological compounds forming a hybrid material [2, 3] is another task attracting the interest of the community, since it opens the way to selectively impart specific properties to the patterned graphene, allowing for controlled tuning of the surface and its selective interaction with the environment. It has been shown that organic molecules grown on graphene may adopt preferred orientation compared to the case of substrates such as e.g. silicon, also due to residuals of poly-methylmetacrylate (PMMA) after transfer of graphene to the final substrate of use [4–6]. In the recent past, we have developed and applied a reliable method for patterning large area graphene by UV single-shot laser ablation [7, 8]. By properly tuning the laser fluence, single layer graphene (SLG) can be selectively removed from micrometric areas of silicon or glass substrate, giving rise to a patterned surface alternating graphene regions with ablated (substrate) regions, in a geometry of choice [7]. This procedure is quick and straightforward when compared to other lithography-based patterning methods. In our previous studies, we have used the fabricated patterned interfaces as substrate for cell seeding. First we investigated adhesion of neurons, after proper uniform functionalization with a cell-adhesive molecule [7]; in that case, in spite of the chemical homogeneity of the substrate after the coating, geometrically ordered functional neural network could be obtained, where neurons preferentially adhered and/or migrated onto the graphene areas, avoiding the ablated ones. In a subsequent work [8], where Chinese hamster ovary cells were cultured, in parallel with single cell adhesion experiments, we also measured a very high adhesion of a silicon nitride probe onto coated graphene as compared to the ablated (i.e. glass substrate) regions.

Intrigued by these observations, and with the aim of gaining more insight on the physico-chemical properties of the patterned (and coated) substrates, we focus here our attention onto the surface potential (SP). Actually, many molecular recognition mechanisms of cells are based on electrostatics [9, 10]. The possibility to tune and to control the SP of the interface could be very important in view of the development of biosensors, since it would provide a method to gain access or to prevent the binding of selected biomolecules. To this purpose, we

* Corresponding author.
E-mail address: silvia.dante@iit.it (S. Dante).

https://doi.org/10.1016/j.tsf.2018.06.037
Received 15 February 2018; Received in revised form 25 May 2018; Accepted 17 June 2018
Available online 19 June 2018

have used scanning Kelvin probe microscopy (SKPM) to measure the SP of our patterned graphene. The surfaces have been functionalized by coating with charged polyelectrolytes, and the layer deposition has been monitored via both SKPM and Raman spectroscopy. The polyelectrolytes of choice were the positively charged poly-D-lysine (PDL), one of the most commonly used cell-adhesion molecules [11] and the negatively charged poly(sodium-4styrene sulfonate) (PSS), a well characterized molecules frequently used in layer-by-layer assemblies [12, 13].

2. Materials and methods

2.1. SLG transfer

SLG grown by chemical vapor deposition on copper (Cu) was purchased from 2D Tech (UK). SLG on SiO_2 was a commercial product purchased from Graphene Supermarket. According to the manufacturer, SLG was transferred on SiO_2 by wet etching procedure and SiO_2 was 285 nm thick. A PMMA solution (MicroChem, 950,000 MW, 9–6 wt% in anisole) was spin-coated (Sawatec SM-180-BT spinner) on SLG/Cu foils at 3000 rpm for 45 s and then the SLG on the opposite side of the Cu foil was removed by 100 W oxygen plasma (180 s), followed by drying at room temperature for 12 h. The Cu was wet-etched using 0.2 M Ammonium persulphate solution in a Petri dish and the PMMA/SLG stack was floated on the surface of the solution. The stack of PMMA/SLG was carefully rinsed in ultrapure water (Millipore, 18 MΩcm) to remove the traces of the Cu etchant, and was scooped on the target substrate (1 cm × 1 cm Si). The transferred SLG substrate was annealed in air at 180 °C for 3 h to obtain a firm adhesion to the glass coverslip and washed with acetone to remove any trace of organic contaminants. All the solvents were purchased from Sigma Aldrich. The quality of the SLG transfer was monitored by Raman spectroscopy.

2.2. Laser patterning of graphene

Exploiting the absorption peak of SLG in the deep UV at 4.6 eV, ablation patterning of the transferred SLG was carried out by a KrF excimer laser with 248 nm wavelength. The Si\SLG surface was patterned in its central area with an array of ablated squares with 40 μm side and 40 μm gap, each obtained by exposure to a single pulse at a laser fluence of 0.5 J/cm^2.

2.3. Raman characterization

Raman spectra have been collected with Horiba Jobin Yvon LabRAM HR800 at ambient conditions. A 632.8 nm excitation line in backscattering geometry through a 50× objective lens was used to excite the SLG on Si.

2.4. Polyelectrolyte coating

PDL (Sigma-Aldrich, MW 30.000–70.000) was dissolved in ultrapure water in a concentration of 0.1 g/L; PSS (Sigma-Aldrich, MW 70.000) was used at a 0.2 g/L concentration in ultrapure water. For each dipping step, the sample was immersed in the polyelectrolyte solution for 20 min and subsequently rinsed for 2 min in ultrapure water for 3 times. After wetting the substrates were dried under gentle Nitrogen flow.

2.5. SKPM

The measurements were carried out on an atomic force microscope MFP-3D (Asylum Research, CA, USA), acquiring images at maximum scan size of 90 μm, with 256^2 pixels, at a (single) line scan frequency of 0.2 Hz. A MESP probe (Bruker, MA, USA) was used, with nominal properties as follows: cantilever resonance frequency of ~75 kHz and

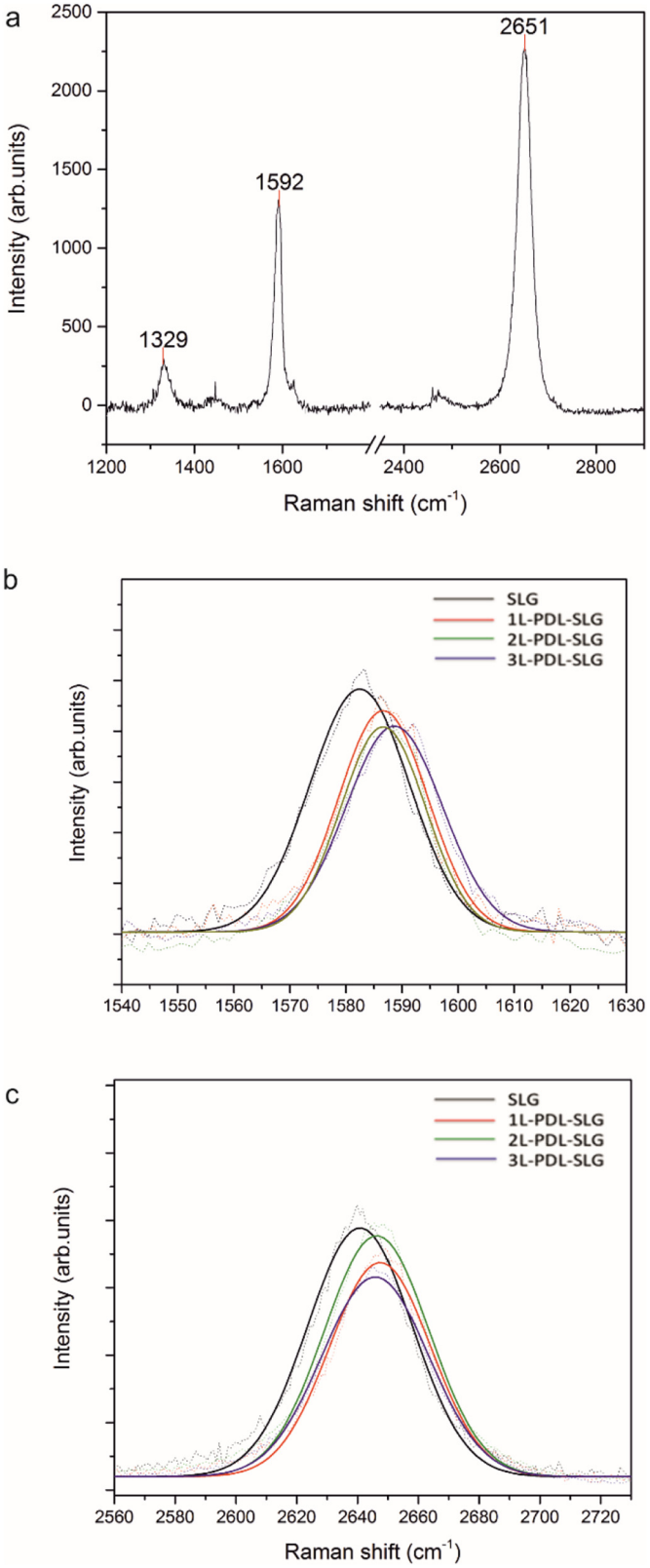

Fig. 1. typical Raman spectrum of SLG transferred onto Si substrate. G-band located at ~1590 cm^{-1} is due to the in plane vibration of sp2 carbon atoms, the 2D located at ~2650 cm^{-1} are visible. The D band at ~1300 cm^{-1} indicates the presence of some defects/impurities (a) G-band Raman peak of bare SLG (black, dotted) and of PDL coated SLG after different dipping cycles (colors, dotted). A progressive shift towards higher wave number is observable (b). 2D-band Raman peak of bare SLG (black, dotted) and of PDL coated SLG after different dipping cycles (colors, dotted). A progressive shift towards higher wave number is observable (c).

Co-Cr coating on the tip of ~30 nm, resulting in a final tip diameter of ~70 nm. The tip work function Φ_{tip}, after calibration on highly oriented pyrolytic graphite (HOPG), assumed to have $\Phi_{HOPG} = 4.65$ eV [7], appeared to be ~4.61 eV. The samples were back contacted at their bottom on a metal puck support.

The SKPM technique relies on double-pass method, where each line is scanned first in tapping-mode to track the surface topography and then is scanned again at a set elevation height (50 nm in our case) to avoid topographical artifacts. During the elevated scan, the cantilever is dithered electrically, by applying a tip voltage (with sample substrate set to ground) consisting of a DC and an AC component (the latter at the resonance frequency). A feedback circuit cancels out the force on the probe by tuning the DC voltage component, which thus equals the local SP value.

3. Results and discussion

Raman characterization of SLG onto Si substrate demonstrated a successful transfer of graphene, with low number of defects. A typical spectrum is reported in Fig. 1a The G-band at 1584 cm^{-1} is due to the in plane vibration of sp^2 carbon atoms; the 2D-band at 2700 cm^{-1} is due to a two phonon lattice vibration; and the D-band at 1350 cm^{-1} is due to broken symmetry after graphene layer edges and inner defects [14]. The ratio of the intensities of the 2D and G bands, I_{2D}/I_G, around a factor 2, and the sharp symmetric 2D band are indications of a good quality graphene in spite of the presence of few defects and impurities, possibly due to the transfer process, showing in the D-band [15]. Fig. 1b–c report in detail the G and 2D bands of the samples, including bare SLG (black curve), centered at 1588 cm^{-1} and 2651 cm^{-1}, respectively, along with the best fitting profiles (Table 1), which will be used for further characterization.

The conditions for laser ablation of SLG on Si were optimized during previous works [7, 8], and were used here to remove the graphene on the selected square areas. As visible in the topographic image of Fig.2a, the patterning was carried out successfully with micrometric resolution, and the ablated graphene squares showed a clear, flat bottom of non-modified substrate, as well as intact surrounding graphene regions. As the only side-effect of ablation, several debris particles appear in the image, especially at the square edges. The SP map obtained in the same scanned area is displayed in Fig.2b. A striking contrast in SP is observed. When averaging among several different regions, the values of the contrast at the squares and of the graphene background (mean ± standard deviation) were 143 ± 22 mV and − 440 ± 60 mV, respectively.

In another set of experiments, commercial SLG on Si\SiO_2 was used for laser patterning and for the subsequent characterization by SKPM. The results (Fig.4) showed a reverse contrast between graphene and the ablated squares of SiO_2, indicating that the contrast sign of the patterned region can be appropriately chosen by changing the substrate for graphene transfer.

The following step of our experiment was the coating of the surface with a charged polyelectrolyte to modify the local SP. Given the above voltage values in Fig.2b, despite the positive contrast against the graphene background the SP stayed negative also on the ablated squares. Therefore, we selected a positively charged molecule, i.e. PDL. The interest in studying this specific coating comes, as mentioned in the Introduction, from the use of PDL as cell adhesive layer [11].

Table 1
Change of SLG Raman G-peak position and width before and after polymer coating, according to the best fitting curves in Fig. 1.

	G-peak position (cm^{-1})	G-peak width (cm^{-1})	2D-peak position (cm^{-1})	2D-peak width (cm^{-1})
Bare Si	\SLG	1583.3 ± 0.-4	11.2 ± 0.2	2640.8 ± 1.0
34.-4 ± -2.3				
1 L-PDL	1585.5 ± 0.3	9.1 ± 0.3	2647.1 ± 1.1	33.2 ± 2.1
2 L-PDL	1588.1 ± 0.5	11.1 ± 0.5	2645.8 ± 1.1	35.1 ± 2.2
3 L-PDL	1588.1 ± 0.4	9.8 ± 0.5	2646.3 ± 1.0	34.4 ± 2.3

After immersing the sample in the PDL solution, we repeated the characterization previously performed on the graphene coated Si. As for the Raman measurements, a shift in the G and 2D bands of graphene was observed, as already reported in the literature (see supporting information to [16]). This shift, accompanied by a slightly reduced width of the peak (Table 1), is an indication of the stiffening of the graphene vibrations and is independent of the sign of the polyelectrolyte coating.

AFM topography and surface potential maps after one dipping step in PDL solution are reported in the second row of Fig.2d (namely panels 2d-f). No major differences are detected in the topography after PDL coating (number of layers n = 1) as compared to the pristine surface. Indeed, it is assumed that both regions (ablated squares and surrounding graphene) are equally coated with PDL, being both negative, and this conformal coating does not give rise to a different depth of the topographic step at the squares. However, the effective PDL coating is observed in the SP image (Fig.2e), as a shift of the SP towards less negative values (−155 ± 55 mV), as expected after a coating step with a positively charged molecule (see Fig.3, filled circles sequence, datapoint at n = 1), in agreement with [16]. Nevertheless, the SP remains still negative, and in particular is lower than that at the squares. This result, i.e. a more negative SP on SLG with respect to ablated regions, is surprising when compared to our results on living cells seeding [7, 8]. In fact, the cell membrane is negatively charged, and higher adhesion would be expected on areas with positive, or less negative, SP. Actually, the higher adhesion of cells on PDL coated graphene might be due to a preferential accumulation on those areas of extra cellular matrix molecules, highly secreted by the cells, which in turn promote preferential cell binding. Alternatively, a different molecular arrangement of the PDL polymer on the two regions carrying a different SP could be envisaged, so that PDL on graphene provides more binding sites to the cell membrane.

Incidentally, the contrast between the two regions was not varied (see Fig.3, void circles sequence, n = 1). Because the SP stayed still negative on both regions, we decided to repeat the dipping step in PDL solution and perform the measurement recursively, until a positive value of the SP was measured. As shown in Fig.3, after the second PDL dipping step (n = 2) the SP was further shifted towards higher values, for both SLG and ablated regions, indicating another uniform deposition of PDL at the surface. Concurrently, consistent Raman results were observed, as shown in Fig. 1b–c and detailed in Table 1. At that point, the SP was around zero; indeed, one additional dipping step (n = 3) did not cause any significant shift in SP, as a hint of no more PDL coating; in fact, in Fig.2j some points of sticky matter, shifted by the scanning tip, are observed, which could be associated with non-adhered excess PDL spots. As a matter of fact, Fig.3 shows a plateau in graphene SP for n = 2,3, and no further changes are observed either in the Raman peak shift.

Interestingly, the SP contrast stayed constant across the whole series of PDL dipping steps (n = 0,3), as shown by the void circles datapoints in Fig. 3. The physical origin of this local contrast is unclear at present, as it could be due to electrical charging or to a change in material work function occurring after laser irradiation. In fact the SP measured by SKPM arises from different contributions of intrinsic material properties (i.e. work function), electrostatic charge, and bias effects. The interplay of all these factors is also the reason for a rich literature claiming the tuning of graphene work function on the one hand [17–19] and pointing to the difficult repeatability and reliability of absolute SP values on the other hand, mainly due to ambient contamination [20–22]. These issues, together with uncertainty in the actual number of graphene layers [23] and arbitrary assumption on the reference material

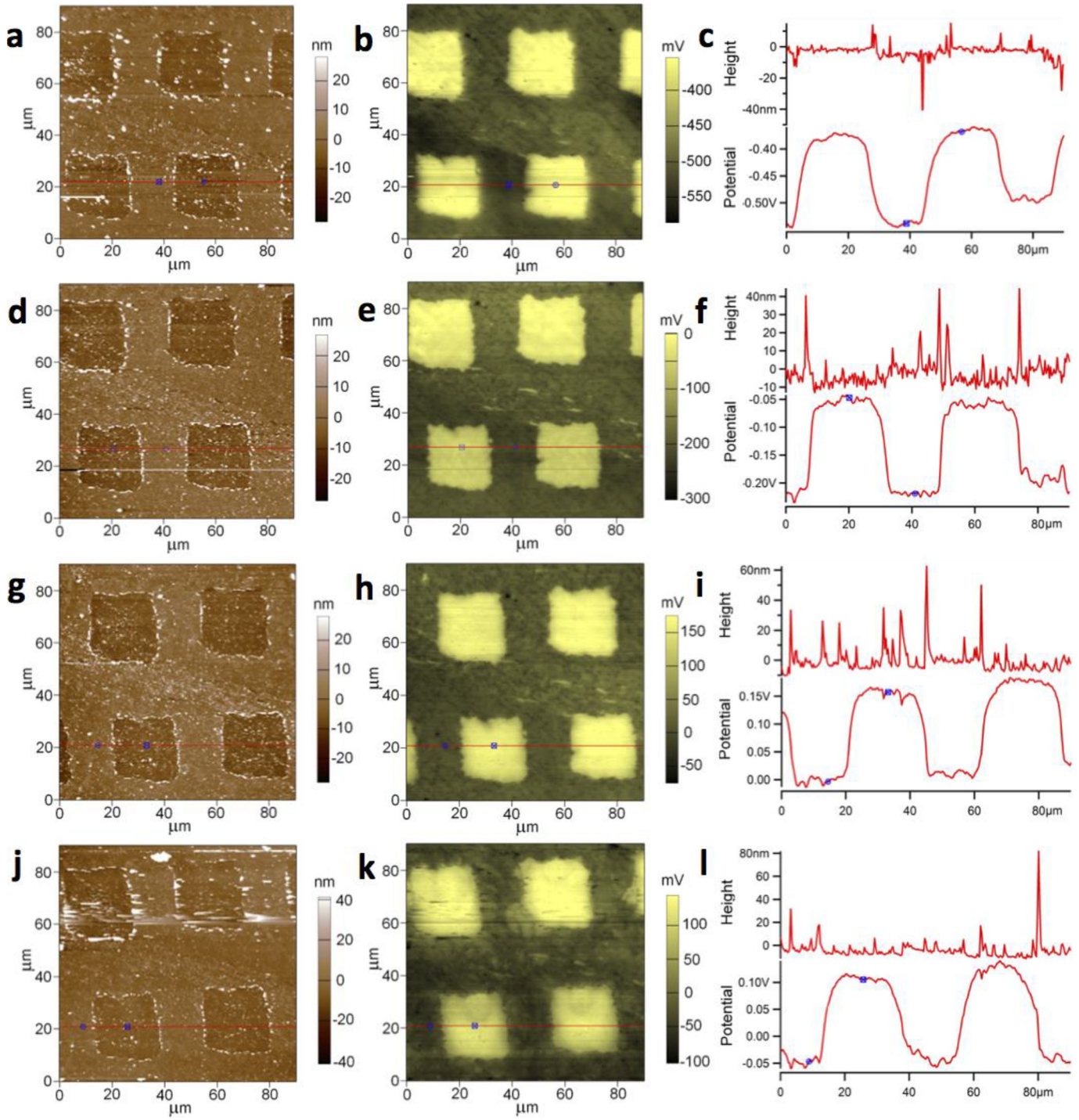

Fig. 2. AFM topography of the patterned substrate before (a) and after PDL coating (d, g, j corresponding to 1 L-PDL, 2 L-PDL, 3 L-PDL, respectively). Center: SKPM maps of the same region, showing a higher potential in correspondence of the ablated squares (b, e, h, k). Right: Scan line profiles of topography and surface potential.

work function during tip calibration, makes the absolute SP level uncertain and the material SP contrast within a given image is thus the only reliable information [24].

When the neutral SP and eventually the reversal of its initial negative value was reached (n = 3), the sample was further assessed by a control modification and test measurement. A dipping in PSS solution was carried out. As expected, a decrease in SP was detected when the starting from the n = 3 case (see respective diamond datapoint), indicating PSS adsorption. As a confirmation, the dipping in PSS was also carried out for another sample at PDL dipping stage n = 1, which on the contrary did not exhibit any significant SP shift towards negative values (diamond datapoint in Fig.3 for n = 1), thus confirming the electrostatic physisorption mechanism of the polyelectrolytes.

4. Conclusions

The presented results show that it is possible to fabricate a patterned SLG interface with a robust SP contrast in the two regions of the pattern (ablated SLG i.e. substrate vs SLG), and the background (SLG) SP level. Additionally, the SP levels can be tuned by physisorption of

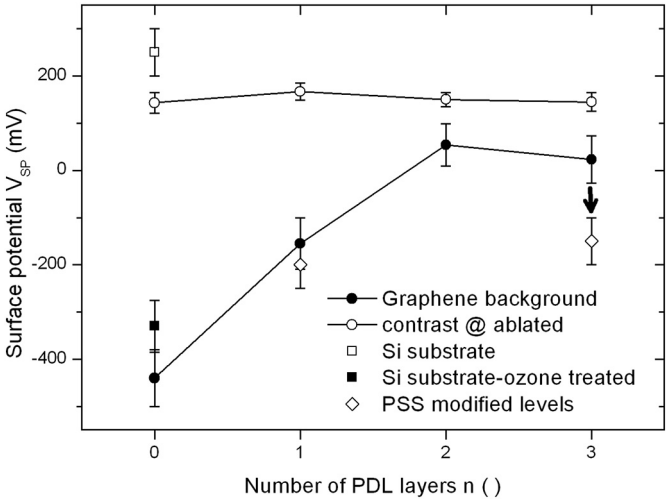

Fig. 3. Surface potential change during coating cycles with PDL (full dots): on SLG the negative surface potential changes linearly from −450 mV to +20 mV, where it reaches a plateau at the 3rd cycle. At the same time, the measured SP contrast (empty dots) between SLG and ablated areas does not vary.

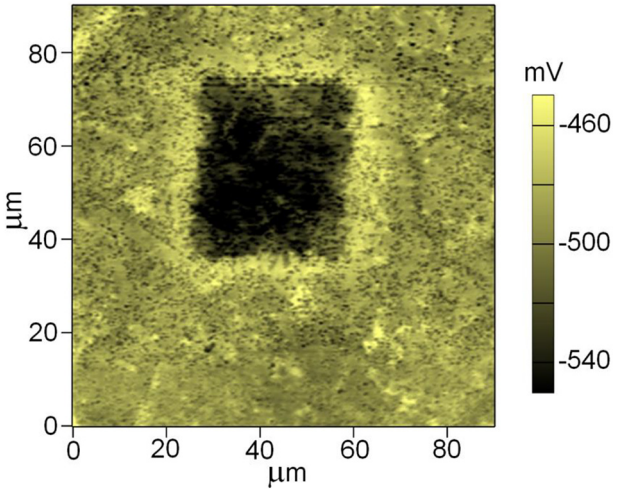

Fig. 4. SP contrast at the surface of a SLG sample transferred on SiO_2: the SP on the ablated squares is lower than on SLG background.

appropriately charged polyelectrolytes. Moreover, preliminary indications exist that by changing the substrate (from Si to SiO_2) the contrast itself at the ablated regions can be chosen either positive or negative. The tuning of this surface property can find useful application, since many interfacial phenomena are regulated by electrostatics. More detailed investigations should address the physical origin of the SP contrast at the laser ablated regions, which could be ascribed to local electrical charging after the laser energy delivery during irradiation, or a change in material work function.

Conflict of interest

The authors declare no competing interests.

References

[1] M.J. Allen, V.C. Tung, R.B. Kaner, Honeycomb carbon : a review of graphene, Chem. Rev. 110 (2010) 132–145, http://dx.doi.org/10.1021/cr900070d.
[2] C. Sanchez, K.J. Shea, S. Kitagawa, Hybrid materials themed issue, Chem. Soc. Rev. 40 (2011) 696–753, http://dx.doi.org/10.1039/c0cs00136h.
[3] A.D. Oyedele, C.M. Rouleau, D.B. Geohegan, K. Xiao, The growth and assembly of organic molecules and inorganic 2D materials on graphene for van der Waals heterostructures, Carbon N. Y. 131 (2018) 246–257, http://dx.doi.org/10.1016/j.carbon.2018.02.020.
[4] K. Xiao, W. Deng, J.K. Keum, M. Yoon, I.V. Vlassiouk, W. Kendal, A. Li, I.I. Kravchenko, G. Gu, E.A. Payzant, G. Sumpter, S.C. Smith, J.F. Browning, D.B. Geohegan, K.W. Clark, E. a Payzant, B.G. Sumpter, S.C. Smith, F. James, Surface-induced orientation control of CuPc molecules for the epitaxial growth of highly ordered organic crystals on graphene surface-induced orientation control of CuPc molecules for the epitaxial growth of highly ordered organic crystals on graphene, J. Am. Chem. Soc. 135 (2013) 3680–3687, http://dx.doi.org/10.1021/ja3125096.
[5] B.Y. Shi, W.D. Dou, Study of copper-phthalocyanine and pentacene film growth on transferred graphene: the influence of polymer residues, Thin Solid Films 636 (2017) 723–729, http://dx.doi.org/10.1016/j.tsf.2017.07.028.
[6] B.-Y. Shi, W.-D. Dou, J.-X. Tang, Influences of polymer residues on the growth properties of Pentacene thin film on graphene substrates, J. Phys. Chem. C 122 (2018) 5606–5614, http://dx.doi.org/10.1021/acs.jpcc.8b00759.
[7] M. Lorenzoni, F. Brandi, S. Dante, A. Giugni, B. Torre, Simple and effective graphene laser processing for neuron patterning application, Sci. Rep. 3 (2013) 1–9, http://dx.doi.org/10.1038/srep01954.
[8] S. Keshavan, R. Oropesa-Nu, A. Diaspro, C. Canale, S. Dante, Adhesion and migration of CHO cells on micropatterned single layer graphene, 2D Mater 4 (2017), http://dx.doi.org/10.1088/2053-1583/aa57e9.
[9] P. Kukić, J.E. Nielsen, Electrostatics in proteins and protein – ligand complexes, Future Med. Chem. 2 (2010) 647–666, http://dx.doi.org/10.4155/FMC.10.6.
[10] N. Sakai, S. Matile, On the electrostatics of cell-membrane recognition : from natural antibiotics to rigid push - pull rods, Chem. Eur. J. 6 (2000) 1731–1737, http://dx.doi.org/10.3389/neuro.16.006.2009.
[11] S.S. Rao, J.O. Winter, Adhesion molecule-modifi ed biomaterials for neural tissue engineering, Front. Neuroeng. 2 (2009) 1–14, http://dx.doi.org/10.3389/neuro.16.006.2009.
[12] S. Dante, T. Hauß, R. Steitz, C. Canale, N.A. Dencher, Biochimica et Biophysica Acta Nanoscale structural and mechanical effects of beta-amyloid (1–42) on polymer cushioned membranes: a combined study by neutron re fl ectometry and AFM Force Spectroscopy, BBA - Biomembr. 1808 (2011) 2646–2655, http://dx.doi.org/10.1016/j.bbamem.2011.07.024.
[13] J.F. Quinn, J.C.C. Yeo, F. Caruso, Layer-by-layer assembly of Nanoblended thin films : poly (allylamine hydrochloride) and a binary mixture of a synthetic and natural polyelectrolyte, Macromolecules 37 (2004) 6537–6543, http://dx.doi.org/10.1021/ma0490698.
[14] A.C. Ferrari, J.C. Meyer, V. Scardaci, C. Casiraghi, M. Lazzeri, F. Mauri, S. Piscanec, D. Jiang, K.S. Novoselov, S. Roth, A.K. Geim, Raman spectrum of graphene and graphene layers, Phys. Rev. Lett. 97 (2006), http://dx.doi.org/10.1103/PhysRevLett.97.187401 (187401-1-187401–4).
[15] A. Das, B. Chakraborty, A.K. Sood, Raman spectroscopy of graphene on different substrates and influence, Bull. Mater. Sci. 31 (2008) 579–584, http://dx.doi.org/10.1007/s12034-008-0090-5.
[16] Y.Y. Wang, P.J. Burke, Polyelectrolyte multilayer electrostatic gating of graphene field-effect transistors, Nano Res. 2 (2014) 1–9, http://dx.doi.org/10.1007/s12274-014-0525-9.
[17] Y.-J. Yu, Y. Zhao, S. Ryu, L.E. Brus, K.S. Kim, P. Kim, Tuning the graphene work function by electric field effect, Nano Lett. 9 (2009) 3430–3434, http://dx.doi.org/10.1021/nl901572a.
[18] R. Garg, N.K. Dutta, N.R. Choudhury, Work function engineering of graphene, Nano 4 (2014) 267–300, http://dx.doi.org/10.3390/nano4020267.
[19] R. Vidyasagar, B. Camargo, E. Pelegova, K. Romanyuk, A.L. Kholkin, Controlling Surface Potential of Graphene Using dc Electric Field, KnE Mater. Sci. (2016) 183–189, http://dx.doi.org/10.18502/kms.v1i1.583.
[20] F. Schedin, A.K. Geim, S.V. Morozov, E.W. Hill, P. Blake, M.I. Katsnelson, K.S. Novoselov, Detection of individual gas molecules adsorbed on graphene, Nat. Mater. 6 (2007) 652–655, http://dx.doi.org/10.1038/nmat1967.
[21] M.H. Abdellatif, S. Ghosh, I. Liakos, A. Scarpellini, S. Marras, A. Diaspro, Effect of nanoscale size and medium on metal work function in oleylamine-capped gold nanocrystals, J. Phys. Chem. Solids 89 (2016) 7–14, http://dx.doi.org/10.1016/j.jpcs.2015.09.012.
[22] M.H. Abdellatif, S. Keshavan, S. Dante, M. Salerno, Induced inhomogeneity in graphene work function due to graphene - TiO2/Ag/glass substrate interaction, Thin Solid Films 628 (2017) 43–49, http://dx.doi.org/10.1016/j.tsf.2017.03.011.
[23] P. Nemes-Incze, Z. Osvath, K. Kamaras, L.P. Biro, Anomalies in thickness measurements of graphene and few layer graphite crystals by tapping mode atomic force microscopy, Carbon N. Y. 6 (2008) 2–9, http://dx.doi.org/10.1016/j.carbon.2008.06.022.
[24] M.H. Abdellatif, M. Salerno, A. Polovitsyn, S. Marras, F. De Angelis, Applied surface science sensing the facet orientation in silver nano-plates using scanning kelvin probe microscopy in air, Appl. Surf. Sci. 403 (2017) 371–377, http://dx.doi.org/10.1016/j.apsusc.2017.01.175.